



ISSN 1028-8546

Volume XXVIII Number 3

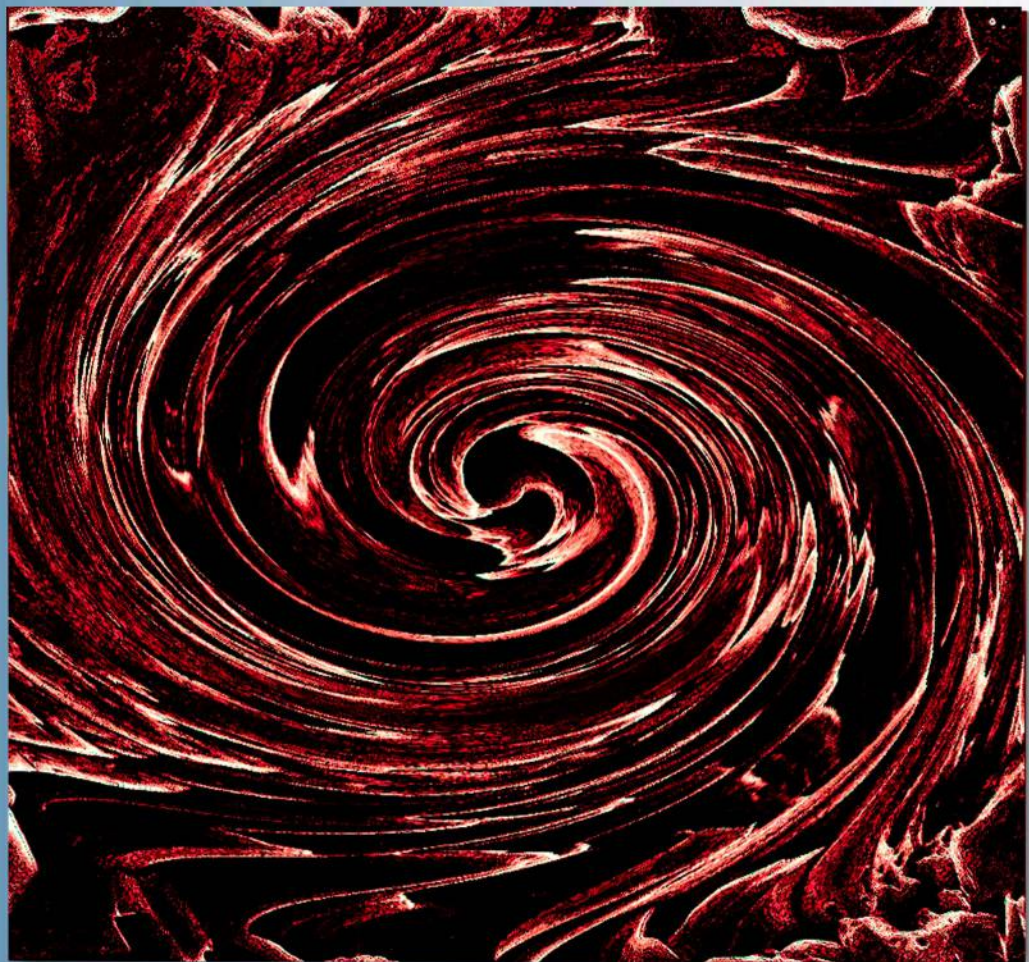
Section: En October, 2022

# Azerbaijan Journal of Physics

# Fizika

[www.physics.gov.az](http://www.physics.gov.az)

[www.physics.gov.az/ajpfizika.html](http://www.physics.gov.az/ajpfizika.html)



Institute of Physics

Azerbaijan National Academy of Sciences

Department of Physical, Mathematical and Technical Sciences

Published from 1995  
Ministry of Press and Information  
of Azerbaijan Republic,  
Registration number 514, 20.02.1995

ISSN 1028-8546  
vol. XXVIII, Number 03, 2022  
Section: En

## *Azerbaijan Journal of Physics*

# *FIZIKA*

*Institute of Physics  
Azerbaijan National Academy of Sciences  
Department of Physical, Mathematical and Technical Sciences*

### HONORARY EDITORS

Arif PASHAYEV

### EDITORS-IN-CHIEF

Arif HASHIMOV

### SENIOR EDITOR

Talat MEHDIYEV

### INTERNATIONAL REVIEW BOARD

Arif Hashimov, Azerbaijan  
Boris Denker, Russia  
Vyacheslav Tuzlukov, Belarus  
Gennadii Jablonskii, Belarus  
Vladimir Man'ko, Russia  
Mirhasan Seyidov, Turkey  
Dieter Hochheimer, USA  
Victor L'vov, Israel  
Huseyn Ibragimov, Azerbaijan

Nazim Mamedov, Azerbaijan  
Majid Ebrahim-Zadeh, Spain  
Anatoly Boreysho, Russia  
Mikhail Khalin, Russia  
Javad Abdinov, Azerbaijan  
Faik Mikailzade, Turkey  
Tayar Djafarov, Azerbaijan  
Kerim Allahverdiyev, Azerbaijan  
Talat Mehdiyev, Azerbaijan

Zakir Jahangirli, Azerbaijan  
Salima Mehdiyeva, Azerbaijan  
Nadir Abdullayev, Azerbaijan  
Oktay Tagiyev, Azerbaijan  
Ayaz Bayramov, Azerbaijan  
Tofiq Mammadov, Azerbaijan  
Shakir Nagiyev, Azerbaijan  
Rauf Guseynov, Azerbaijan

### TECHNICAL EDITORIAL BOARD

Senior secretary: Elmira Akhundova; Nazli Huseynova, Elshana Aleskerova,  
Rena Nayimbayeva, Nigar Aliyeva, Zuleykha Abdullayeva

### PUBLISHING OFFICE

131, H. Javid ave., AZ-1143, Baku  
ANAS, Institute of Physics

Tel.: (99412) 539-51-63, 539-32-23  
Fax: (99412) 537-22-92  
E-mail: [jophphysics@gmail.com](mailto:jophphysics@gmail.com)  
Internet: [www.physics.gov.az](http://www.physics.gov.az)

Published at " \_\_\_\_\_"  
\_\_\_\_\_ str., Baku

Sent for printing on: \_\_\_\_\_. 201\_  
Printing approved on: \_\_\_\_\_. 201\_  
Physical binding: \_\_\_\_\_  
Number of copies: \_\_\_\_\_ 200  
Order: \_\_\_\_\_

It is authorized for printing:

## THE PECULIARITIES OF ELECTRICAL CONDUCTIVITY IN $\text{AgSbSe}_2$ AND $(\text{AgSbSe}_2)_{0,85}(\text{PbTe})_{0,15}$

A.A. SADDINOVA, R.I. SELIM-ZADEH, A.E. BABAYEVA

*Institute of Physics of Azerbaijan National Academy of Sciences*

*H. Javid ave., 131, AZ-1143, Baku, Azerbaijan*

*e-mail: saddinova.aynur@mail.ru*

Temperature dependence of electrical conductivity in  $\text{AgSbSe}_2$  and  $(\text{AgSbSe}_2)_{0,85}(\text{PbTe})_{0,15}$  solid solution was investigated in the temperature range 80-350K. It is determined that the electrical conductivity of  $(\text{AgSbSe}_2)_{0,85}(\text{PbTe})_{0,15}$  solid solution to have a hopping mechanism in the temperature range 127-233K. In both compositions, the activation energy of the charge carriers was calculated in different temperature ranges.

**Keywords:** hopping conductivity, activation energy,  $\text{AgSbSe}_2$

**PACS:** 72.20.-i

### INTRODUCTION

Ternary chalcogenide  $\text{AgSbSe}_2$  is great interest as a good thermoelectric material due to its low thermal conductivity.  $\text{AgSbSe}_2$  crystallizes in a cubic rock salt structure with a space group of  $Fm\bar{3}m$ . In this structure the Ag and Sb atoms randomly occupy the sites of their sublattice, forming a disordered substructure [1]. The investigations of  $\text{AgSbSe}_2$  was carried out basically above room temperature for the purpose to improve thermoelectric properties by adding various elements [2, 3, 4]. In addition, the determination of the mechanism of transport of electric charge in  $\text{AgSbSe}_2$  and its solid solutions are very interesting.

As is known, both  $\text{AgSbSe}_2$  and  $\text{PbTe}$  are good thermoelectric materials that used at medium temperatures (400-800K) [5]. Both of compositions have the same crystal structure, which allows obtaining a number of solid solutions based on them [6, 7].

In this work,  $(\text{AgSbSe}_2)_{0,85}(\text{PbTe})_{0,15}$  solid solution was investigated for the purpose to study the influence of  $\text{PbTe}$  addition on the mechanism of transport of charge carriers in  $\text{AgSbSe}_2$  and to determine the activation energy of charge carriers.

### EXPERIMENTAL RESULTS AND DISCUSSION

The investigated samples were synthesized by direct fusion of high purity elements (99,99% purity) taken in stoichiometric ratios in quartz tube. The tubes

were flame sealed under vacuum ( $10^{-4}$  Torr) and slowly heated in the furnace up to 1000 K over 12 h. The furnace temperature was gradually increased at a rate of 1 K/min. Then tubes held for 10 h in this temperature and were gradually cooled to room temperature at the same rate.

The X-ray diffraction analysis for the obtained samples were performed on a Bruker D8 Advance diffractometer. The lattice constant was determined from the analysis of XRD peak positions with the EVA and TOPAS programs. The results of X-ray analysis (shown in Figure 1) revealed that both of samples were single phase with the cubic NaCl-type structure ( $Fm\bar{3}m$ ).

The lattice constants of  $\text{AgSbSe}_2$  and  $(\text{AgSbSe}_2)_{0,85}(\text{PbTe})_{0,15}$  are  $a=5,762\text{\AA}$ ,  $a=5,845\text{\AA}$ , respectively. Ionic radius of Pb (Te) is larger than of Sb. Therefore, as bigger Pb (Te) is introduced in the place of smaller Sb, the unit cell undergoes a systematic expansion, leading to increase in the lattice parameter [8].

The electrical conductivity of  $\text{AgSbSe}_2$  and  $(\text{AgSbSe}_2)_{0,85}(\text{PbTe})_{0,15}$  was measured by four-point probe method on direct current.

Figure 2 presents the temperature dependence of electrical conductivity of  $(\text{AgSbSe}_2)_{0,85}(\text{PbTe})_{0,15}$  solid solution in comparison with  $\text{AgSbSe}_2$ . The experimental results show that, at temperatures below  $T=300\text{K}$ , the electrical conductivity of the samples is relatively small and does not change much. The value of electrical conductivity of both samples with the temperature rise begins to increase.

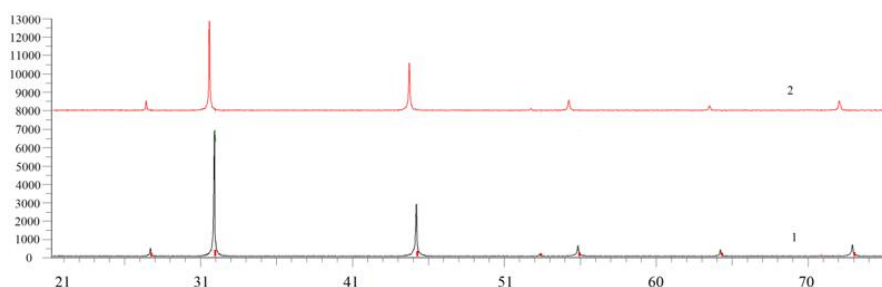


Fig. 1. X-ray diffraction patterns of  $\text{AgSbSe}_2$  (1) and  $(\text{AgSbSe}_2)_{0,85}(\text{PbTe})_{0,15}$  (2).

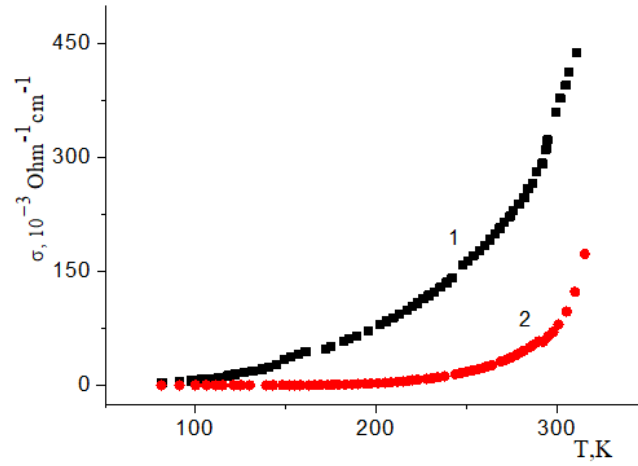


Fig. 2. Temperature dependences of electrical conductivity of AgSbSe<sub>2</sub> (1) and (AgSbSe<sub>2</sub>)<sub>0.85</sub>(PbTe)<sub>0.15</sub> (2).

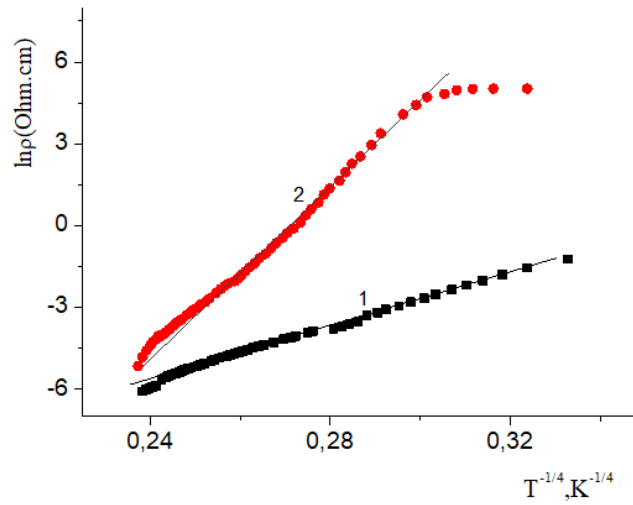


Fig. 3. Temperature dependences of specific resistance of AgSbSe<sub>2</sub> (1) and (AgSbSe<sub>2</sub>)<sub>0.85</sub>(PbTe)<sub>0.15</sub> (2) in Mott coordinates.

The temperature dependences of the resistivity of (AgSbSe<sub>2</sub>)<sub>0.85</sub>(PbTe)<sub>0.15</sub> solid solution in Mott coordinates in comparison with AgSbSe<sub>2</sub> in the 80-350K temperature range are presented in Figure 3.

As seen in figure, the experimental points at certain temperatures correspond to the linear dependence in Mott coordinates. This fact to affirm that both AgSbSe<sub>2</sub> and (AgSbSe<sub>2</sub>)<sub>0.85</sub>(PbTe)<sub>0.15</sub> solid solution the charge transfer occurs by the hopping conductivity of charge carriers over localized states lying in a narrow energy region near the Fermi level. As is known, in this case electrical conductivity is described by Mott's relation [9]:

$$\rho = \rho_0 \exp(T_0/T)^{1/4}, \quad T_0 = \beta/k_B g(\mu) a^3 \quad (1)$$

where  $k_B$  is Boltzmann's constant,  $g(\mu)$  is density of localized states near the Fermi level,  $a$  is radius of localized states near the Fermi level,  $\beta$  is number depending on dimension of the problem (for the three dimensional case  $\beta=21$ ).

As can be seen in Figure 3, the Mott dependence (1) for the AgSbSe<sub>2</sub> and (AgSbSe<sub>2</sub>)<sub>0.85</sub>(PbTe)<sub>0.15</sub> solid

solution are satisfied in the temperature ranges  $105K < T < 230K$  and  $127K < T < 233K$ , respectively. The fact that the electrical conductivity of AgSbSe<sub>2</sub> has a hopping mechanism is reported in detail in [10].

As a result of calculations based on relation (1), for the density of localized states near the Fermi level in (AgSbSe<sub>2</sub>)<sub>0.85</sub>(PbTe)<sub>0.15</sub> the value of  $g(\mu) = 3,7 \cdot 10^{14} \text{eV}^{-1} \text{cm}^{-3}$  was obtained.

Thus, it was determined that the electrical conductivity of (AgSbSe<sub>2</sub>)<sub>0.85</sub>(PbTe)<sub>0.15</sub> solid solution, as in AgSbSe<sub>2</sub>, has a hopping mechanism in the temperature range 127-233K. At higher temperatures only the band conductivity prevails.

One of the main problems in explaining the mechanism of conductivity is the calculation of the activation energy of charge carriers. For this purpose, in Figure 4 shows the dependence of the logarithm of the specific conductivity of AgSbSe<sub>2</sub> and (AgSbSe<sub>2</sub>)<sub>0.85</sub>(PbTe)<sub>0.15</sub> versus  $1/T$ . The values of the activation energy of charge carriers of AgSbSe<sub>2</sub> and (AgSbSe<sub>2</sub>)<sub>0.85</sub>(PbTe)<sub>0.15</sub> solid solution were calculated based on the values of linear region at the coordinates  $\ln \sigma \sim (1/T)$  in the temperature range 200-550K.

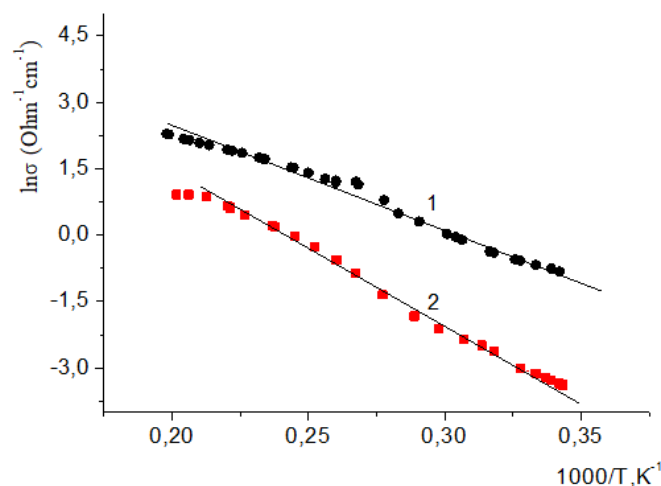


Fig. 4. Dependence of logarithm of electrical conductivity of  $\text{AgSbSe}_2$  (1) and  $(\text{AgSbSe}_2)_{0,85}(\text{PbTe})_{0,15}$  versus  $1000/T$ .

As a result of the calculation, for the activation energy of charge carriers of  $\text{AgSbSe}_2$  and  $(\text{AgSbSe}_2)_{0,85}(\text{PbTe})_{0,15}$  in different temperature ranges the values of  $\Delta E=78$  meV (200-300K),  $\Delta E=211$  meV (300-400K),  $\Delta E=130$  meV (400-500K) and  $\Delta E=173$  meV (200-300K),  $\Delta E=312$  meV (300-400K),  $\Delta E=158$  meV (400-500K) were obtained, respectively. It is seen from the obtained results, the activation energy of the charge carriers in both composition takes different values in different temperature range. The different values of activation energy of charge carriers is caused by the existence of different impurity levels in the band gap. Also, the value of activation energy of charge carriers of  $(\text{AgSbSe}_2)_{0,85}(\text{PbTe})_{0,15}$  increases compared to the value obtained for  $\text{AgSbSe}_2$ . The formation of impurity conductivity as a result of doped with PbTe increases the value of activation energy.

## CONCLUSION

The electrical conductivity of  $(\text{AgSbSe}_2)_{0,85}(\text{PbTe})_{0,15}$  solid solution has hopping mechanism in the temperature range 127-233K. The activation energy of  $\text{AgSbSe}_2$  and  $(\text{AgSbSe}_2)_{0,85}(\text{PbTe})_{0,15}$  are increasing with temperature rise. As a result of doped with PbTe the formation of impurity conductivity increases the value of the activation energy of charge carriers of  $(\text{AgSbSe}_2)_{0,85}(\text{PbTe})_{0,15}$  compared to  $\text{AgSbSe}_2$ .

## ACKNOWLEDGEMENTS

The authors are grateful to Dr. Physics S.S. Ragimov for consultation on the results of research.

- [1] S. Geller and J.H. Wernick. Ternary semiconducting compounds with sodium chloride-like structure:  $\text{AgSbSe}_2$ ,  $\text{AgSbTe}_2$ ,  $\text{AgBiS}_2$  and  $\text{AgBiTe}_2$ . Acta Crystallographica, 1959, 12 (1), p. 46-54
- [2] S. Cai, Z. Liu, J. Sun et al. Enhancement of thermoelectric properties by Na doping in Te-free p-type  $\text{AgSbSe}_2$ . Dalton Transactions, 2015, 44 (3), p. 1046-1051
- [3] Z. Liu, J. Shuai, H. Geng et al. Contrasting the role of Mg and Ba doping on the microstructure and thermoelectric properties of p-type  $\text{AgSbSe}_2$ . ACS Applied Materials and Interfaces, 2015, 7 (41), p. 23047-23055
- [4] D. Li, X.Y. Qin, T.H. Zou et al. High thermoelectric properties for Sn-doped  $\text{AgSbSe}_2$ . Journal of Alloys and Compounds, 2015, 635, p. 87-91
- [5] J.R. Sootsman, H. Kong, C. Uher et al. Large enhancements in the thermoelectric power factor of bulk PbTe at high temperature by synergistic nanostructuring. Angew. Chem. Int. Ed., 2008, 47, p.8618-8622
- [6] Y. Xiao, L.-D. Zhao. Charge and phonon transport in PbTe-based thermoelectric materials. npj Quantum Materials, 2018, 3(55), p. 1-12
- [7] H.Z. Wang, Q.Y. Zhang, B. Yu et al. Transmission electron microscopy study of Pb-depleted disks in PbTe-based alloys. Journal of Materials Research, 2011, 26(7), p. 912-916
- [8] S.N. Guin, C. Arindom, S.N. Devendra et al. High thermoelectric performance in tellurium free p-type  $\text{AgSbSe}_2$ . Energy Environ. Sci., 2013, 6(9), 2603-2608
- [9] N.F. Mott, E.A. Davis. Electronic processes in non-crystalline materials. New York: Oxford University Press, 1979, 590 p.
- [10] S.S. Ragimov, A.A. Saddinova, A.I. Aliyeva. Mechanism of electrical conductivity and thermal conductivity in  $\text{AgSbSe}_2$ . Russian Physics Journal, 2019, 62 (6), p.1077-1081.

Received: 01.06.2022

## INFRARED SPECTRA, DIFFERENTIAL SCANNING CALORIMETRY AND MECHANICAL PROPERTIES OF POLYETHYLENE DOPED WITH $\text{CaGa}_2\text{S}_4:\text{Eu}^{2+}$

T.D. IBRAGIMOV, O.B. TAGIEV, I.S. RAMAZANOVA, T.Sh. IBRAHIMOVA,  
A.F. NURALIYEV, E.G. ASADOV, B.H. IBRAGIMOV

*Institute of Physics, Azerbaijan National Academy of Sciences, Azerbaijan  
131, H. Javid ave., Baku, AZ 1143, Azerbaijan  
e-mail:tdibragimov@mail.ru*

High-density polyethylene with the additive of  $\text{CaGa}_2\text{S}_4:\text{Eu}^{2+}$  particles of different concentrations is investigated by infrared spectroscopy, differential scanning calorimetry and strength testing methods. It was shown that the presence of particles leads to an increase in the effective infrared absorption associated with an increase in scattering, a decrease in the heat of transition, and an increase in the ordering of the system. In this case, the yield threshold decreases with a simultaneous increase in the elastic modulus.

**Keywords:** phosphor, high density polyethylene, composite material.

**PACS:** 77.55.-f, 77.84. s , 77.84.Dy, 77.84.Lf, 81.07.Pr , 82.35.Np

### INTRODUCTION

Production of high-performance devices for imaging and lighting, which are capable of competing with conventional systems, requires the obtaining of phosphors with specific properties. This necessity promoted the development of new materials and the optimization of existing phosphors. One of such promising materials is  $\text{CaGa}_2\text{S}_4:\text{Eu}^{2+}$ . Its monocrystal and polycrystal emits a broad yellow luminescence band is centered at 562 and 565 nm, respectively, under both 420 nm and 337.1 nm excitation wavelengths [1-2].

The spectroscopic properties of the phosphor  $\text{CaGa}_2\text{S}_4:\text{Eu}^{2+}$  provide high performance. However, it is not only requirement for the respective devices. Active luminescent elements must be resistant to water, solar radiation and temperature. The phosphor cannot meet these requirements by itself. Its encapsulation is required. Typically, a polymer is used as the matrix. To predict the most optimal conditions for encapsulation, it is necessary to determine the interaction between the filler particles and the matrix.

The aim of present work is the study of high-density polyethylene with the additive of  $\text{CaGa}_2\text{S}_4:\text{Eu}^{2+}$  particles by infrared spectroscopy, differential scanning calorimetry and strength testing methods.

### EXPERIMENTAL

$\text{CaGa}_2\text{S}_4:\text{Eu}^{2+}$  (5 mol %) polycrystals were prepared from stoichiometric amounts of CaS and  $\text{Ga}_2\text{S}_3$  powders.  $\text{EuF}_3$  was used for the activation by europium. The synthesis of this material was done by a solid-state reaction in a graphite crucible covered with graphite powder at temperature of 1000°C and vacuum of  $10^{-4}$  Torr for 4 hours. After the synthesis, a 4-hour annealing was carried out at 700°C in an argon atmosphere with hydrogen sulfide.

Powder was obtained by grinding in the planetary micro mill (the model Pulverisette 7, firm Fritsch, Germany).

The powder obtained was separated according to sedimentation time  $\tau$  in a column with hexane according to the relation:

$$\tau = \frac{18h\eta}{(\rho_1 - \rho_2)gd^2} \quad (1)$$

where  $h$  is the height of the column;  $\eta$  is the viscosity coefficient of the liquid;  $\rho_1$  and  $\rho_2$  are the densities of this material and hexane;  $g$  is the acceleration of gravity;  $d$  is the transverse dimension of the particles. The fractions obtained were dried under a vacuum of  $10^{-2}$  torr at  $T = 50^\circ\text{C}$  for a week. This method produced a powder with an average particle size of 500 nm.

We used high density polyethylene (HDPE) as a matrix. Melting and softening points of polymer are 130-135°C and 80-90°C, correspondingly. Then obtained mixture was shaken in a vortex mixer for 1 hour at room temperature, followed by sonication with dispergator Ultrasonic Cleaner NATO CD-4800 (China) for 4 hours. Disc-shaped samples of composites were obtained by hot pressing at temperature of 165°C and pressure of 15 MPa. Pressing time after reaching the selected temperature is 15-20 minutes. The diameter and thickness of the obtained films were 4 cm and 80-90  $\mu\text{m}$ , respectively. Aluminum electrodes with diameter of 3 cm and thickness of 10  $\mu\text{m}$  are pressed on both sides of the films.

The infrared spectra of the samples were obtained using an FTIR 7600 Fourier spectrometer in the range of 7800-375  $\text{cm}^{-1}$  with a resolution no worse than 0.5  $\text{cm}^{-1}$ .

Thermal analysis of the samples is carried out in the inert gas (argon) by differential scanning calorimeter NETZSCH DSC 204 F1 (Germany). Liquid nitrogen is used as a protective gas and sample cooling. A sample with weight of 40 mg is placed in an aluminum pan. In the same way, a sapphire as reference sample is placed in another pan, and under exactly the same conditions, both panes are heated at

the rate of 10 K/min. The flow rate of the inert gas is chosen to be 20 ml/min and the studies are carried out in the temperature range from -10°C to 600°C.

The Tinius Olsen H5KS Benchtop Tester from Advanced Test Equipment Corporation with 50 N

probes was used for definition of mechanical parameters.

**RESULTS AND DISCUSSION**

Figure 1 and 2 show the infrared spectra of both pure polyethylene and composites.

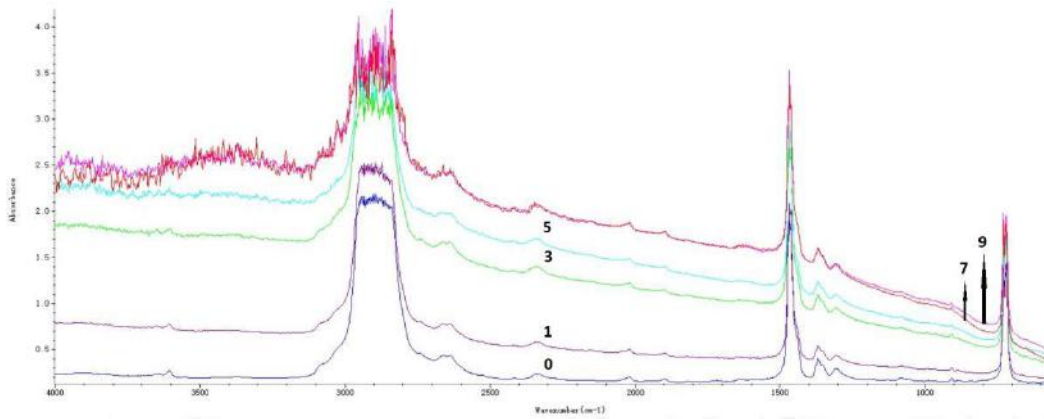


*Fig. 1. Infrared spectra of the pure polyethylene and composites.*

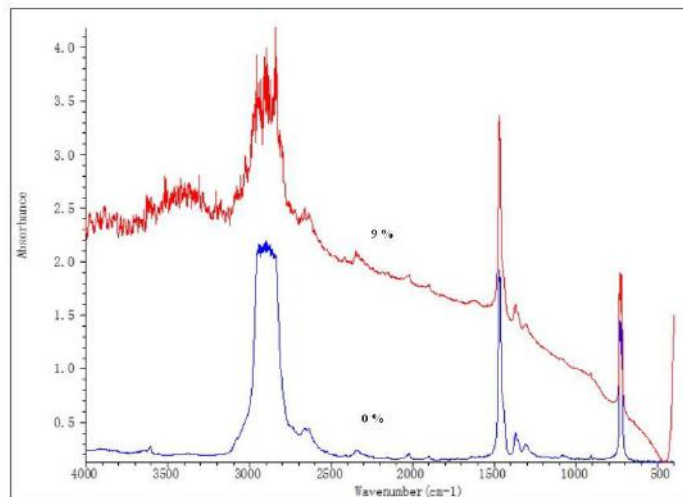


*Fig. 2. Infrared spectra of the pure polyethylene and the composite with 9 vol.% filler.*

All samples exhibit pronounced absorption peaks which correspond to different types of CH<sub>2</sub> vibrations: a) the wide band 3100-2700 cm<sup>-1</sup> which is manifestation of asymmetric stretching vibrations with symmetry B<sub>1u</sub> (2924 cm<sup>-1</sup>) and B<sub>2u</sub> (2899 cm<sup>-1</sup>); symmetric stretching vibrations B<sub>1u</sub> (2850 cm<sup>-1</sup>) and B<sub>2u</sub> (2857 cm<sup>-1</sup>); b) rather narrow split band 1500-1400 cm<sup>-1</sup> which corresponds to B<sub>1u</sub> (1473 cm<sup>-1</sup>) and B<sub>2u</sub> (1463 cm<sup>-1</sup>) deformation vibrations; c) 650-750 cm<sup>-1</sup> band corresponding to B<sub>1u</sub> (731cm<sup>-1</sup>) and B<sub>2u</sub> (720 cm<sup>-1</sup>) pendulum vibrations. In addition, a number of narrow peaks of low intensity are observed.

As can be seen, there are no noticeable changes in the positions of the absorption bands upon addition of the filler. It indicates that the particles have almost

no effect on various types of vibrations in polymer chains. However, in this case, the band 3100–2700 cm<sup>-1</sup> broadens and the total absorption increases. The latter fact is related to the scattering of infrared radiation in a heterogeneous medium [3].

Figures 3-8 show heat flow versus temperature (DSC) for both the pure polyethylene and composites at heating and cooling regimes. These dependences exhibit peaks at certain temperatures T<sub>c</sub>, the areas under which correspond to the enthalpy characterizing the heat of transition from the solid state to the liquid one. At the same time, in the heating regime, this transition is endothermic, that is, heat is required, and when cooled, it is exothermic, in which heat is released.

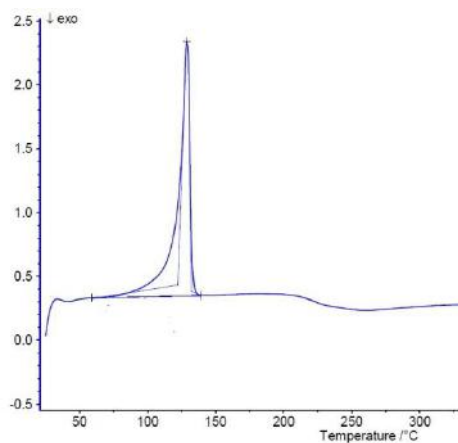


Fig.3. Temperature dependence of heat flow for the pure polyethylene.

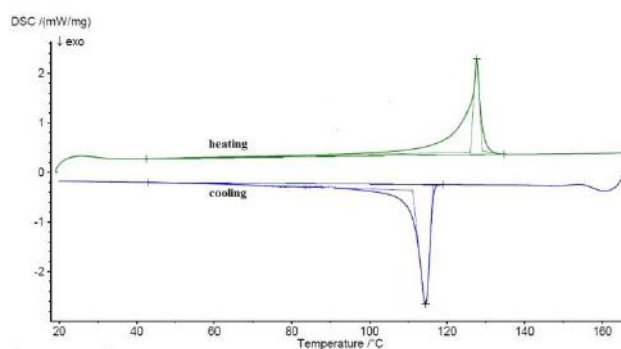


Fig. 4. Temperature dependence of heat flow for the pure polyethylene doped with 1vol.% of CaGa<sub>2</sub>S<sub>4</sub>:Eu<sup>+2</sup>

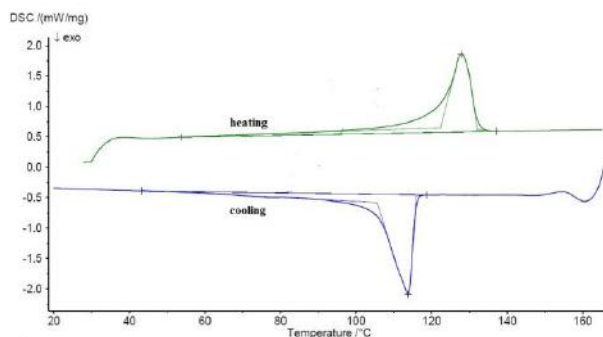


Fig.5. Temperature dependence of heat flow for the pure polyethylene doped with 3vol.% of CaGa<sub>2</sub>S<sub>4</sub>:Eu<sup>+2</sup>

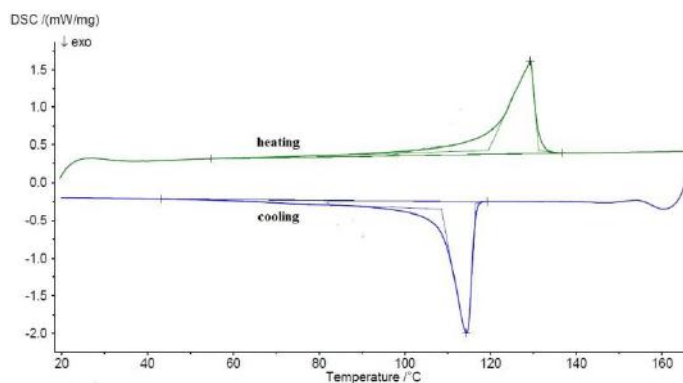


Fig.6. Temperature dependence of heat flow for the pure polyethylene doped with 5vol.% of CaGa<sub>2</sub>S<sub>4</sub>:Eu<sup>+2</sup>

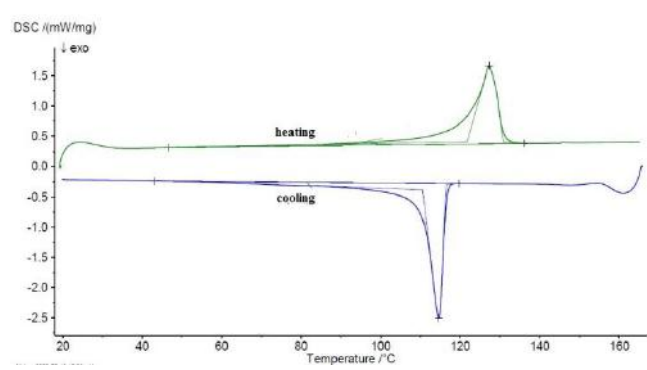


Fig.7. Temperature dependence of heat flow for the pure polyethylene doped with 7 vol.% of CaGa<sub>2</sub>S<sub>4</sub>:Eu<sup>2+</sup>

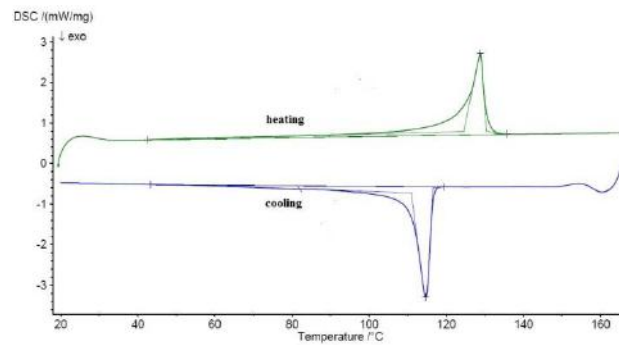


Fig.8. Temperature dependence of heat flow for the pure polyethylene doped with 9 vol.% of CaGa<sub>2</sub>S<sub>4</sub>:Eu<sup>2+</sup>

Table 1 shows the transition temperatures  $T_c$ , the change in enthalpy  $\Delta H$ , and the change in entropy  $\Delta S$  defined by the formula  $\Delta S = \Delta H/T_c$ .

Table 1.

The transition temperatures  $T_c$ , the change in enthalpy  $\Delta H$  and entropy  $\Delta S$  at this transition for the pure polyethylene and composites with different concentration of filler.

%	heating			cooling		
	T°C	$\Delta H$ , J/q	$\Delta S$ , J/q	T°C	$\Delta H$ , J/q	$\Delta S$ , J/q
0	128.9	125.2	0.97			
1	127.7	72.59	0.57	114.5	81.62	0.71
3	127.8	82.17	0.64	113.8	89.97	0.79
5	129.3	70.25	0.54	114.5	79.09	0.69
7	127.3	71.46	0.56	114.6	82.3	0.72
9	128.8	91.81	0.71	114.7	98.15	0.86

As can be seen, with the addition of particles even at concentration of 1%, the enthalpy, that is, the heat of transition sharply decreases. It indicates on weakening of intermolecular bonds in polymer chains due to the inclusion of particles. In this case, entropy (the measure of disorder) also decreases. It indicates on an increase in the ordering of the structure. The

addition of particles has little effect on the melting and solidification temperatures themselves. In this case, the curing temperature is shifted to low temperatures with respect to the melting temperature.

The results of some measurements of mechanical parameters are shown in Table 2.

Table 2.

Mechanical parameters of the pure polyethylene and composite with 9 vol.% of CaGa<sub>2</sub>S<sub>4</sub> Eu<sup>2+</sup>.

Specimen	Thickness (mm)	Width (mm)	Ultimate force (N)	Ultimate stress (MPa)	Modulus (MPa)
pure HDPE	0.075	12.4	16.7	18.1	512
HDPE+9 vol.% CaGa <sub>2</sub> S <sub>4</sub> Eu <sup>2+</sup> .	0.075	12.4	11.8	12.7	585

In this table, ultimate stress is the stress at the yield point and modulus is the elastic modulus. As seen, the ultimate force and stress decrease. It indicates on a decrease in intermolecular interaction in the presence of particles and is consistent with thermal analysis data. But on the other hand, the elastic properties increase due to the incorporation of particles into the polymer chains.

## **CONCLUSIONS**

It is known that the additive of  $\text{CaGa}_2\text{S}_4$   $\text{Eu}^{2+}$  particles into high-density polyethylene leads to light scattering in the composites, weakening of intermolecular bonds in polymer chains and an increase of elastic properties.

- 
- [1] *C. Ronda, T. Justel, H. Nikol.* Rare earth phosphors: fundamentals and applications. *J. of Alloys and Compounds.* 1998, 669, 275–277.
- [2] *P. Benalloul, C. Barthou, C. Fouassier, A.N. Georgobiani, L.S. Lepnev, Yu.N. Emirov, A.N. Gruzintsev, B.G. Tagiev, O.B. Tagiev,*
- R.B. Jabbarov.* Luminescence of  $\text{Eu}^{2+}$  in Calcium Thiogallate. *Journal of The Electrochemical Society,* 2003,150, G62-G65.
- [3] *C.F. Bohren & D.R. Huffman.* 1983. Absorption and Scattering of Light by Small Particles, John Wiley & Sons. New York 530 p.

*Received: 17.06.2022*

## SIMULATION SPATIAL STRUCTURE OF AMYLOID BETA-PEPTIDE (28-35) DETERMINED BY MOLECULAR MECHANICS METHOD

G.Z. NAJAFOVA

*UFAZ under Azerbaijan State Oil and Industry University,  
183, Nizami str., Baku, Azerbaijan  
[gulyaz.najafova@ufaz.az](mailto:gulyaz.najafova@ufaz.az)*

Conformational properties of Alzheimer's  $\beta$ -amyloid (28-35) peptide have been studied by molecular mechanics method. Using a fragmentary approach, energy-efficient spatial structures of the molecule were identified. It has been shown that this peptide molecule forms a stable conformation with two different structures: one is a complete  $\alpha$ -helical structure, and the other is a beta-freezing structure at the N-terminal complemented by a small alpha helix. Calculations The hypocritical angles of all residues in the low-energy conformations of the amyloid beta (28-35) peptide molecule and their orientations relative to each other were determined. Based on the obtained results, three-dimensional spatial structures of the amyloid- $\beta$  (28-35) peptide molecule were modelled

**Keywords:** Amyloid beta peptide (28-35), conformation,  $\alpha$ -helical structure, molecular mechanics.

**PACS:** 36.20. Ey; 87.15.Aa; 87.15.He

### INTRODUCTION

Alzheimer disease (AD) is an age-related progressive neurodegenerative disorder. Alzheimer's disease is a condition accompanied by degenerative processes in nerve cells leading to increasing impairments to cognitive functions such as language, behavioural activities and memory. AD is associated with accumulation of excess amounts of amyloid- $\beta$  (A $\beta$ ) protein in the form of extracellular senile plaques, with disruption of neuronal interactions and nerve cell death [1].

It is known that  $\beta$ -amyloid peptide molecules play an important role in the pathogenesis of Alzheimer's disease [2]. It is well established that A $\beta$ P possesses neurotoxic activity. A $\beta$ P neurotoxicity has been associated to peptide self-aggregation, which leads to the formation of amyloid-like fibrils and eventually to neuronal cell death through apoptosis. The complete  $\beta$ -amyloid peptide molecule consists of 42 amino acid residues. Its biological activity properties are attributed to the peptide A $\beta$  (25-35), which consists of 11 residues. It has been established that the peptide A $\beta$  (25-35) is the shortest A $\beta$  fragment of the whole molecule that retains some amyloidogenic and cytotoxic properties [3] At the same time, the A $\beta$  (28-35), consisting of eight amino acid residues Lys1 – Gly2 – Ala3 – Ile4 – Ile5 – Gly6 – Leu7 – Met8 – NH<sub>2</sub>, is the main part of the C-terminal of the peptide A $\beta$  (25-35). The role of this region in determining the second peptide structure and neurotoxicity is important. Therefore, the study of the conformational properties of the peptide A $\beta$  (28-35) is of particular interest.

### CALCULATION METHODS

In the presented work, the spatial structure of the octapeptide molecule Lys<sup>1</sup> – Gly<sup>2</sup> – Ala<sup>3</sup> – Ile<sup>4</sup> – Ile<sup>5</sup> – Gly<sup>6</sup> – Leu<sup>7</sup> – Met<sup>8</sup> – NH<sub>2</sub> was studied and modeled by molecular mechanics.

Molecular mechanics (MM) study of A $\beta$  (28-35) conformation involves multistage extensive computations of even-increasing fragments, with a set stable forms of each preceding step used as a starting set in the next step. Only those conformations are retained whose energies are smaller than some cut-off values. The sequential method was used, combining all low-energy conformations of constitutive residues For this purpose, the conformational properties of Ile<sup>4</sup> – Ile<sup>5</sup> – Gly<sup>6</sup> – Leu<sup>7</sup> – Met<sup>8</sup> – NH<sub>2</sub> pentapeptide, consisting of five amino acid residues, and Lys<sup>1</sup> – Gly<sup>2</sup> – Ala<sup>3</sup> – Ile<sup>4</sup> tetrapeptide, consisting of four amino acid residues, were first studied by molecular mechanics. In the method of molecular mechanics, the total internal potential energy of a molecule is equal to the sum of the energy values of the interactions of each pair of atoms that are not in its valence bond. The conformational energy of peptide molecules is defined on the basis of a mechanical model as the sum of the energies of non-valent, electrostatic, torsional interactions and hydrogen bonds, provided that the valence angles and bonds are constant:  $E_{\text{conf}} = E_{\text{nb}} + E_{\text{el}} + E_{\text{tor}} + E_{\text{hb}}$ .

The first term was described by the Lennard-Jones 6-12 potential with the parameters proposed by Scott and Scheraga. The electrostatic energy was calculated in a monopole approximation corresponding to Coulomb's law with partial charges of atoms as suggested by Scott and Scheraga. An effective dielectric constant value  $\epsilon=1$  for vacuum,  $\epsilon=4$  for membrane environment and  $\epsilon=80$  for water surrounding is typically used for calculations with peptides and proteins, which create the effects of various solutions on the conformations of peptides by MM method [4].

Conformational analysis of molecules was carried out on the basis of optimal conformation conditions of the amino acid residues that make up them [5]. Energy is minimized by the gradient method for the first order derivatives. The conformational analysis took into account the Van der Waals, electrostatic, torsional interactions energy fractions and hydrogen bond energy of the peptides to be studied. Conformational analysis

of tetrapeptide from a universal program and algorithm developed by N.M. Gojayev and I.S. Maksumov was used in solving structural problems [6]. The different forms of the main chain of the peptide molecule are divided into several classes: through the folded (f) and open (e) shapes. Thus, the number of chains that can form a peptide molecule consisting of an N amino acid residue can only be  $2N-1$ . Each chain creates its own main and side chain interactions. The conformation of the fossils is indicated by the letters corresponding to the following areas of the Ramachandran map of the hypocritical angles  $\varphi, \psi$ : R ( $\varphi=-180^{\circ}\div 0^{\circ}, \psi=-180^{\circ}\div 0^{\circ}$ ), B ( $\varphi=-180^{\circ}\div 0^{\circ}, \psi=0^{\circ}\div 180^{\circ}$ ), L ( $\varphi=0^{\circ}\div 180^{\circ}, \psi=0^{\circ}\div 180^{\circ}$ ); P ( $\varphi=0^{\circ}\div 180^{\circ}, \psi=-180^{\circ}\div 0^{\circ}$ ). The calculation of hypocritical angles was carried out according to the IUPAC-IUB nomenclature. [7] Based on these

symbols, the conformational state of each residue is described by  $H_{ij}$ , using a certain system of identifiers. The indices of the letters (R, B, L, P) characterize the state of the side chain: the number 1 corresponds to the fields  $\sim 00\div 1200$ , the number 2 to the fields  $\sim 1200\div -1200$ , the number 3 to the fields  $\sim -1200\div 00$ . As a result of the calculations, the energy fractions that play a role in stabilizing the optimal conformations of peptide molecules were determined.

## RESULTS AND DISCUSSION

The conformational properties of the amyloid- $\beta$  (28-35) peptide were investigated on the basis of the selected fragmentary [8] calculation scheme shown in Figure 1:

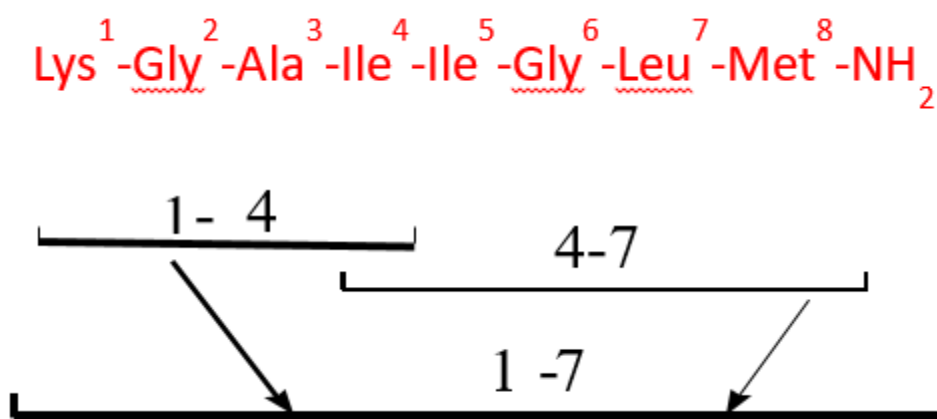


Fig. 1. Scheme for calculating the optimal compatibility of the peptide A $\beta$  (28-35).

Table 1.

The relative energy values of stable structures in separate fragments of A $\beta$  (28-35) peptide

Ile-Ile-Gly-Leu-Met-NH <sub>2</sub> pentapeptide		Lys-Gly-Ala-Ile tetrapeptide	
RRRRR	Relative energy (kcal/mol)	Backbone form	Relative energy (kcal/mol)
RRBRR	0,0	RRRR	0,0
BRBBB	3,0	BRRR	1,0
RBBRR	3,1	BBRR	1,9
BRBRR	3,1	RBRR	2,0
RBBBB	3,6	RBBB	2,4
RBBBBR	3,7	BRBB	2,8
BBBBB	3,8	RRRR	3,0
RRRRR	4,6	RRBB	3,7

Theoretical computational studies were performed on the polar medium (dielectric) of the pentapeptide Ile<sup>4</sup> – Ile<sup>5</sup> – Gly<sup>6</sup> – Leu<sup>7</sup> – Met<sup>8</sup> – NH<sub>2</sub>, consisting of five amino acid residues [9], and the tetrapeptide Lys<sup>1</sup> – Gly<sup>2</sup> – Ala<sup>3</sup> – Ile<sup>4</sup>, consisting of four amino acid residues [10]. Table 1 shows the backbone form and the relative energy for each backbone form, for pentapeptide and tetrapeptide molecules.

After determining the most stable conformations, Lys<sup>1</sup> – Gly<sup>2</sup> – Ala<sup>3</sup> – Ile<sup>4</sup> – Ile<sup>5</sup> – Gly<sup>6</sup> – Leu<sup>7</sup> – Met<sup>8</sup> – NH<sub>2</sub> octapeptide was calculated by overlapping this

pentapeptide and tetrapeptide. Analysis of the initial structures of the C-terminal A $\beta$  (28-35) octapeptide shows that the  $\alpha$ -helical conformation has minimal energy. All other stable conformations have a spiral rotation at the end of the C-terminal. That is, the longer the  $\alpha$ -helix at the end of the peptide's C-terminal, the more stable the octapeptide. This conformation is mainly distinguished by the energy of the dispersion interaction. Table 2 shows that only RRRRRRRR form of the octapeptide has minimum energy.

Table 2.

Distribution of calculated conformations of Lys-Gly-Ala-Ile-Ile-Gly-Leu-Met-NH<sub>2</sub> octapeptide in the relative energy range.

Form of main chain	Relative energy (kcal/mol)					
	0-1	1-2	2-3	3-4	4-5	>5
RRRRRRRR	2	1	7	5	3	Remain
BBRRRRRR	-	-	-	-	-	All
BRRRRRRR	-	-	-	-	-	All
BBRRRRRR	-	-	-	-	-	All
BRRRRRRR	-	-	-	-	-	All
BRRRBBBB	-	-	-	-	-	All
RBBRRRRR	-	-	-	-	-	All
RBBBRRRR	-	-	-	-	-	All
RRRRRRRR	-	-	-	-	-	All
RLRRRRRR	-	-	-	-	-	All
RRRBBRRR	-	-	-	-	-	All
RRRBBBBB	-	-	-	-	-	All
RRRBRBRR	-	-	-	-	-	All
RRRRRBRR	-	-	-	-	-	All
RRRRBRRR	-	-	-	-	-	All
RRRRBRBB	-	-	-	-	-	All
RRRBBRBB	-	-	-	-	-	All
RRRRBBBB	-	-	-	-	-	All

Low-energy octapeptide conformations differ from each other in the stability of the N-terminal therapeutic fragment. The lowest energy octapeptide conformation R<sub>22</sub>RR<sub>12</sub>R<sub>32</sub>R<sub>32</sub>RR<sub>21</sub>R<sub>32</sub> belongs to the α-spiral fffffff shape. Its durability is 1.6 kcal / mol higher

than the B<sub>22</sub>RR<sub>12</sub>R<sub>32</sub>R<sub>32</sub>RR<sub>21</sub>R<sub>32</sub> conformation in the effffff shape. Table 3. shows the low-energy conformations that characterize the C-terminal octapeptide spatial structure.

Table 3.

Energy fractions of interaction forces of optimal conformations of Lys-Gly-Ala-Ile-Ile-Gly-Leu-Met-NH<sub>2</sub> octapeptide.

Form	Conformation	Energy distribution (kcal/mol)				
		E <sub>nb</sub>	E <sub>el</sub>	E <sub>tor</sub>	E <sub>total</sub>	E <sub>rel</sub>
RRRRRRRR	R <sub>22</sub> RR <sub>12</sub> R <sub>32</sub> R <sub>32</sub> RR <sub>21</sub> R <sub>32</sub>	-38.5	15.0	5.4	-18.0	0
BRRRRRRR	B <sub>22</sub> RR <sub>12</sub> R <sub>32</sub> R <sub>32</sub> RR <sub>21</sub> R <sub>32</sub>	-31.4	13.3	3.8	-14.3	3.6
BBRRRRRR	B <sub>22</sub> BR <sub>12</sub> R <sub>32</sub> R <sub>32</sub> RR <sub>21</sub> R <sub>32</sub>	-31.5	14.7	4.2	-12.6	5.4
RLRRRRRR	R <sub>22</sub> LR <sub>12</sub> R <sub>32</sub> R <sub>32</sub> RR <sub>21</sub> R <sub>32</sub>	-31.6	15.5	4.7	-11.4	6.6
RBRRRRRR	R <sub>22</sub> BR <sub>12</sub> R <sub>32</sub> R <sub>32</sub> RR <sub>21</sub> R <sub>32</sub>	-29.7	14.8	4.0	-10.9	7.1
RRRRBRRR	R <sub>12</sub> RR <sub>12</sub> R <sub>12</sub> B <sub>22</sub> RR <sub>32</sub> R <sub>32</sub>	-30.4	14.7	5.0	-10.7	7.3
BRRRRRRR	B <sub>22</sub> RB <sub>12</sub> R <sub>32</sub> R <sub>32</sub> RR <sub>21</sub> R <sub>32</sub>	-28.7	14.9	3.8	-10.0	8.0
RRRBBBBB	R <sub>12</sub> RR <sub>12</sub> B <sub>22</sub> B <sub>22</sub> BB <sub>32</sub> B <sub>32</sub>	-28.3	14.2	4.3	-9.7	8.2
RRRBBRRR	R <sub>12</sub> RR <sub>12</sub> B <sub>22</sub> B <sub>22</sub> RR <sub>32</sub> R <sub>32</sub>	-28.3	14.4	4.3	-9.6	8.4
RBBBRRRR	R <sub>22</sub> BB <sub>12</sub> B <sub>12</sub> R <sub>32</sub> RR <sub>21</sub> R <sub>32</sub>	-29.3	14.7	5.1	-9.5	8.5
BBRRRRRR	B <sub>12</sub> BB <sub>12</sub> R <sub>22</sub> R <sub>32</sub> RR <sub>21</sub> R <sub>32</sub>	-28.8	14.7	4.6	-9.4	8.5
RBBRRRRR	R <sub>22</sub> BB <sub>12</sub> R <sub>32</sub> R <sub>32</sub> RR <sub>21</sub> R <sub>32</sub>	-28.2	14.3	4.4	-9.5	8.5
RRRRRBBB	R <sub>12</sub> RR <sub>12</sub> R <sub>12</sub> R <sub>32</sub> BB <sub>32</sub> B <sub>22</sub>	-30.0	15.2	5.5	-9.2	8.8
BRRRBBBB	B <sub>22</sub> RR <sub>12</sub> R <sub>32</sub> B <sub>22</sub> BB <sub>32</sub> B <sub>32</sub>	-25.7	13.2	3.5	-9.0	9.0
RRRRBRBB	R <sub>12</sub> RR <sub>12</sub> R <sub>12</sub> B <sub>22</sub> RB <sub>32</sub> B <sub>32</sub>	-28.6	14.9	4.9	-8.8	9.2
RRRBRBBB	R <sub>12</sub> RR <sub>12</sub> B <sub>22</sub> B <sub>22</sub> RB <sub>32</sub> B <sub>32</sub>	-28.2	14.8	4.7	-8.8	9.2
RRRRBRRR	R <sub>12</sub> RR <sub>12</sub> R <sub>12</sub> R <sub>32</sub> BR <sub>32</sub> R <sub>32</sub>	-29.3	15.1	5.5	-8.7	9.3
RRRBRBRR	R <sub>12</sub> RR <sub>12</sub> B <sub>22</sub> R <sub>32</sub> BR <sub>32</sub> R <sub>32</sub>	-28.1	14.8	5.1	-8.3	9.3

In  $\alpha$ -helical conformations, the overall effect of interactions between residues separated by two or three positions is greater than in other octapeptide conformations. However, in the latter conformation, the  $\beta$ -turn at the end of the N-terminal brings the distant residues closer together and causes an interaction between Gly<sup>2</sup> and Met<sup>8</sup> (−1.2 kcal / mol), Ala<sup>3</sup> and Met<sup>8</sup> (−2.7 kcal / mol). In the global  $\alpha$ -spiral conformation, hydrogen bonds are regularly formed between oxygen atoms of carbonyl groups and hydrogen atoms of amide groups: NH (Gly<sup>6</sup>)... OC (Gly<sup>2</sup>), NH (Leu<sup>7</sup>)... OC (Ala<sup>3</sup>), and NH (Met<sup>8</sup>)... OC (Ile<sup>4</sup>). Other conformations also have hydrogen bonds, but these are irregular. Subsequent analysis of the C-terminal

octapeptide was performed according to the stable conformations of all 8 sheets of the Lys<sup>1</sup> – Ile<sup>4</sup> tetrapeptide. Conformational properties of C-terminal octapeptide were analyzed based on the overlap of low-energy conformations of C-terminal Ile<sup>4</sup> – Ile<sup>5</sup> – Gly<sup>6</sup> – Leu<sup>7</sup> – Met<sup>8</sup> – NH<sub>2</sub> pentapeptide and Lys<sup>1</sup> – Ile<sup>4</sup> tetrapeptide. Different conformations and orientations of Ile<sup>3</sup> and Ile<sup>5</sup>, which are common side chains of Ile<sup>4</sup> – Ile<sup>5</sup> – Gly<sup>6</sup> – Leu<sup>7</sup> – Met<sup>8</sup> – NH<sub>2</sub> pentapeptide and Lys<sup>1</sup> – Ile<sup>3</sup> tetrapeptide, were taken into account when formulating the initial structural variants of the octapeptide molecule.

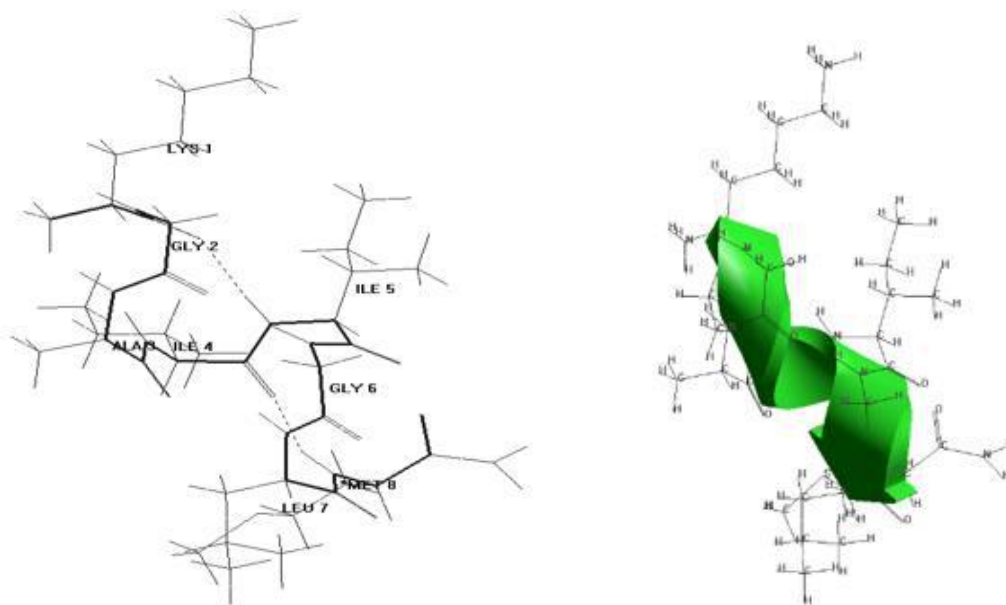


Fig. 2. The most energy-efficient conformation of the peptide A $\beta$  (28-35) (R<sub>22</sub>RR<sub>12</sub>R<sub>32</sub>R<sub>32</sub>RR<sub>21</sub>R<sub>32</sub>).

Figure 2 shows a visual projection of the most energy-efficient conformation of the peptide A $\beta$  (28-35) R<sub>22</sub>RR<sub>12</sub>R<sub>32</sub>R<sub>32</sub>RR<sub>21</sub>R<sub>32</sub>. As a result of calculations, it was determined that the spatial structure of the octapeptide A $\beta$  (28-35) tends to the alpha-helical structure.

## CONCLUSION

The A $\beta$  (28-35) peptide molecule is able to adopt different optimal conformations depending on their

environment. Thus, on the basis of conformational studies of Amyloid  $\beta$ -peptide (28-35) molecule it has been suggested that the biologically active conformation of this peptide at its receptor is alpha helix structure in solution. It should be noted that few lowest energy A $\beta$  (28-35) conformations share the same form of the peptide backbone. Some of these conformations are favourable for the polar environment, while the other favours an apolar solution.

- [1] G. Yamin, K. Ono, M. Inayathullah, D.B. Teplow. Amyloid betaprotein assembly as a therapeutic target of Alzheimer's disease. *Curr. Pharm. Des.*, 2008, vol.14(30), p.3231-3246.
- [2] K. Beyreuther and C.L. Masters. 1997. Alzheimer's disease: the ins and outs of amyloid-. *Nature*. 389:677–678.
- [3] M.P. Mattson, B. Cheng, D. Davis, K. Bryant, I. Lieberburg, and R.E. Rydel. 1992.  $\beta$ -Amyloid peptides destabilize calcium homeostasis and render human cortical neurons vulnerable to excitotoxicity. *J. Neurosci.* 12:376–389.
- [4] R.A. Scott, H.A. Scheraga. *J.Chem.Phys.*, 45, 2091, 1966.
- [5] G.A. Agaeva, N.N. Kerimli, N.M. Godjaev. *Biofizika*, vol.50, N 2, p.203-14, 2005.
- [6] N.M. Godjaev, I.S. Maksumov, L.I. Ismailova. *J.Chem.Struc. (Russian)*, 24, (1983)147-152.
- [7] IUPAC-IUB, *Biochem.J.* (1971) 121,577-585.
- [8] E.M. Popov. Quantitative approach to conformations of proteins // *Int. J. Quant. Chem.*, 1979, v.16, pp. 707-737.

- [9] *G.A. Agaeva, G.Z. Najafova, N.M. Godjaev.* Simulation spatial structure of amyloid beta-peptide (31-35) determined by molecular mechanic method, *Azerbaijan Journal of Physics*, 2019, vol. XXV, № 2, pp. 31-36.
- [10] *G.A. Agaeva, G.Z. Najafova.* Conformational analysis of A $\beta$  (25-28) and A $\beta$ (28-31). III International Scientific Conference of Young Researchers. Azerbaijan, 2019, April, p.44-46.

*Received: 28.06.2022*

## DEMONSTRATING THE IMPORTANCE OF EMISSIVITY MEASUREMENT IN DETERMINING THE DOSES OF LIGHT SOURCES ON TISSUE MIMICKING MATERIALS SUCH AS LASER, IPL AND LED

HÜSEYİN OKAN DURMUŞ<sup>1,2</sup>, MIRHASAN YU SEYİDOV<sup>1</sup>

<sup>1</sup>*Department of Physics, Gebze Technical University, 41400, Kocaeli, Turkey*

<sup>2</sup>*Medical Metrology Laboratory, TUBITAK National Metrology Institute (TUBITAK UME), 41470, Kocaeli, Turkey*

*E-mail: hokandurmus@gtu.edu.tr, smirhasan@gtu.edu.tr;*

*Tel : (262) 605 10 00; Fax: (262) 653 84 90*

Nowadays, a wide variety of low-power light sources such as IPL, LED and laser are frequently used in therapy applications. In this study, irradiance values were calculated for different emissivity values by using the temperature measurement results made in the agar phantom using low-power light sources such as LED, IPL and laser. Based on the irradiance data, energy densities (J/cm<sup>2</sup>) as per the different emissivity coefficient and time durations are calculated and the results were evaluated in terms of dose quantities given in the literature. We also present in detail both acoustic and optical characterization of the agar phantom. In conclusion, we clearly show the importance of emissivity measurement in this study. Our findings explicitly suggest that emissivity measurement must be determined precisely to determine optical power density and/or energy density values and hence doses can be applied on the base of this values.

**Keywords.** Temperature Measurement, Emissivity, Irradiance, Energy Density, Dose, Low-Power Light Sources, Laser, IPL, LED.

**DOI:** <https://doi.org/10.21203/rs.3.rs-1557976/v1>

### INTRODUCTION

In recent years, the use of light therapy in the field of health has been expanding. These low-light-intensity therapies are called as photobiomodulation therapy. Photobiomodulation therapy (PBMT) mainly includes low-level laser therapy (LLL), light-emitting diode (LED) therapy, and broadband light therapy (IPL-Intense Pulsed Light) [1]. Discovered in the late 1960s, this treatment is also called as cold laser, soft laser, low-intensity laser and biostimulatory laser therapy. PBMT is different from lasers that destroy or cut tissue used in cosmetic and surgical procedures.

PBMT, on the other hand, employs non-ionizing, non-thermal light sources in the visible and infrared spectrum (600-1200 nm) to decrease inflammation and promote healing. The light is directed at injured or inflamed tissues through the skin. Intracellular photoreceptors absorb light energy, which triggers a sequence of photochemical intracellular reactions that boost cellular activity and speed up tissue repair. PBMT is also cost-effective, non-invasive, and has been shown to have no negative side effects [2,3,4]. PBM is a treatment used by irradiation with light at low power density. As used at optimum condition of wavelengths and fluences, the beneficial effects of PBMT are photochemical, not thermal because they have been often resulted from the photostimulation of the mitochondrial electron transfer chain. PBMT not only produces therapeutic effects, but also causes no adverse effects on target organs. [4].

PBMT is used to stimulate, heal and regenerate damaged tissue and is thought to work best on diseased or damaged tissue [3]. PBMT has recently been used to treat thousands of individuals all over the world for a variety of medical and dermatological disorders. Applications of PBMT for aesthetic therapy of

disorders such as scars, fine wrinkles, inflammatory acne, photoaged skin, and others have gotten a lot of attention in the recent several decades. PBMT has also been proven to have the ability to improve various dermatological disorders such as acne, vitiligo, and hair loss, as well as cellulite therapy and tooth whitening [4]. It is reported in the literature that PBMT effectively and successfully cures many health problems such as ulcer healing treatment [5-8], wound healing [9-11], tissue repair [12,13], acne vulgaris treatment [14,15], laser hair reduction [16] and skin rejuvenation [17] operations, in improving symptoms of ocular discomfort such as dry eye problem [18] and enhancing bone repair and accelerating bone healing [1]. Furthermore, PBMT has been reported to be an adjuvant therapy option for pain management, lymphedema, wound healing, and musculoskeletal problems [2].

In this study, we present the irradiance and energy density values we calculated on the base of internal temperatures data caused by low power IPL, LED and laser light sources within the agar phantom, with respect to different emissivity coefficients, and we discuss the importance of emissivity coefficient. We also demonstrate optical and acoustical characterization study of the agar phantom. Lastly, we evaluate treatment application times of the investigated light sources, as per the given energy densities for the treatment of various diseases with light in the literature.

### METHODOLOGY

In this study, agar phantom, LED, IPL and laser devices and various types of thermocouples were used. All experiments were performed under controlled laboratory ambient conditions.

**PREPARATION OF AGAR PHANTOM**

Tissue phantom or Tissue-Mimicking Material (TMM) is a kind of material widely applied in medical ultrasonic studies and research due to its capability to mimic biological soft tissues. In our research, as a tissue phantom, agar material was used. Agar phantom was made by preparing approximately a 250 ml solution with 0.4 M ZnCl<sub>2</sub> and 2 % Agar by the weight of the initial water [19].

**THE LIGHT EQUIPMENTS AND MEASUREMENT SYSTEMS**

Philips brand, Lumea Prestige model IPL (epilation) device, Tristar One brand LED therapy device and Optotronics branded VA-I-400-635 model 635 nm wavelength red colored solid-state diode laser were used in the experiments. The laser, IPL and LED devices used on the agar phantom in the experiments can be seen in Figure 1. The operating range of the devices was as follows. The operating range of IPL

device was between 560 nm and 1200 nm. The LED therapy device has 110 LEDs on its right side, 110 LEDs on its left side and 110 LEDs on the top, with four basic lights. These LEDs were mainly red, green, blue and yellow in colour. Red LED was operating at 640 nm wavelength, Blue LED was operating at 423 nm wavelength, Green LED was operating at 532 nm wavelength and Yellow LED was operating at 583 nm wavelength. Maximum working power of the 635 nm red color laser was 400 mW. T-type ultra-fine thermocouples (Physitemp, accuracy is ±0.04 °C) were placed at 15 mm depth in from the phantom surface for the IPL and laser temperature measurement studies. The distance between the four thermocouples was set to be as 2 mm apart. In the LED research, four pieces T-Type Metronik commercial thermocouple with an accuracy of 0.2 °C were used as a thermocouple within the phantom. A PC-based Data Acquisition and Monitoring Interface system was used for multi-channel temperature measurements within the phantom [20-22].



Fig. 1. (a) Laser, b) IPL, and (c) LED devices used in the temperature measurement experiments.

**THE EMISSIVITY, IRRADIANCE AND DOSE CONCEPT**

The efficiency with which a material emits or absorbs energy is referred to as emissivity. The emissivity values are all in the range of 0.0 to 1.0. Because it is expressed as a perfect emitter, The emissivity rating of 1.0 means that 100% of the energy is emitted. A 0.0 emissivity value indicates that the object does not emit any radiation. Materials with a high emissivity value are extremely reflecting or brilliant, whereas materials with a low emissivity value are dark and dull. Emissivity is a complicated material attribute that is influenced by a variety of factors, including material type, surface structure, geometry, observation direction, wavelength, and temperature. The material is the most important factor. Materials can be separated into metal and nonmetal categories in a simplistic categorization. Skin, paper, glass, polymer, and other nonmetallic materials utilized in thermography can be classified as gray bodies and have an emissivity of greater than 0.8. Metallic materials, especially polished metals, on the other hand, often have an emissivity of less than 0.2. Even for the same material, the surface structure can have a significant impact on its emissivity. For instance, a polished metal

can have an emissivity of 0.02, but if the surface is roughened, the number rises to almost 0.8 [23].

The Stefan-Boltzmann law, as shown in Eq.1-3, says that thermal radiation intensity depends on the fourth power of the temperature.

$$I = e\sigma T^4 \quad [24] \quad (1)$$

$$I = \frac{P}{A} \quad (2)$$

$$P = e\sigma AT^4 \quad (3)$$

In the equations, “I” represents the intensity of the radiation or the power per unit area, “e” represents the object's surface radiation emissivity coefficient, which is a dimensionless number between 0 and 1, “σ” is the Stefan-Boltzmann constant (σ= 5,6703 x 10<sup>-8</sup> Watt m<sup>-2</sup> K<sup>-4</sup>), “T” represents the temperature, “P” represents the power, and “A” represents the area of the cavity opening.

The light dose is evaluated using the following formula;

$$\text{Dose} = (\text{Power Density} \times \text{Time}) \times 0.001 \quad [25] \quad (4)$$

The same standardized units and measurements (doses as J/cm<sup>2</sup>, power density as mW/cm<sup>2</sup>, and also time as seconds (s) unit) are utilized when computing the light doses.

### THE OPTICAL CHARACTERIZATION SETUP

Optical equipment included a compact spectrometer (Thorlabs, CCS200/M) with a wavelength

range of 200 nm to 1000 nm, a broadband stabilized fiber-coupled white light source (Thorlabs, SLS201L/M), and a single integrating sphere (Thorlabs IS200 type 2" integrating sphere). And the thickness of the agar phantom specimen cut out as a sample was 22 mm. Figure 1 shows the experiment set-up, and Figure 2 shows how all of the optical measurements and computations were realized using Thorlabs OSA software.

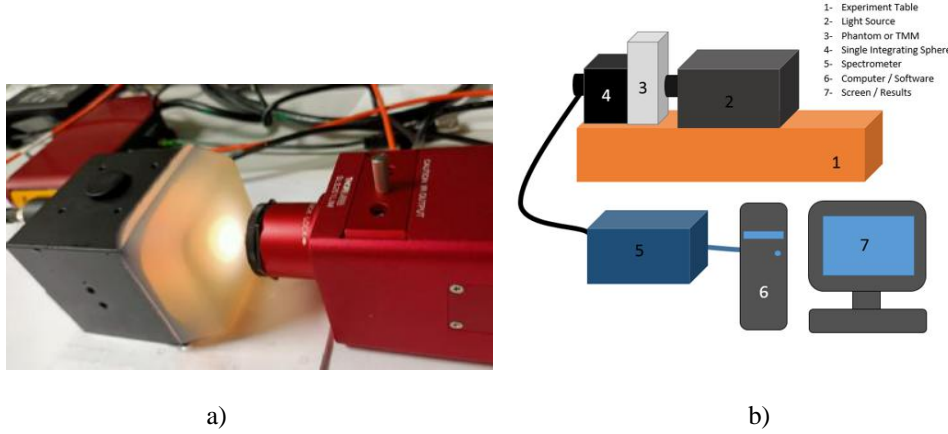


Fig. 2. a) A picture showing the phantom measurement; b) Experiment set-up. 1-experimental table, 2-light source, 3-sample (phantom or TMM), 4-single integrating sphere, 5-compact spectrometer, 6-computer and 7-computer monitor.

### ASSESSMENT OF THE OPTICAL DATA

First, the spectrum of the incoming light was obtained during the measurement. The light spectrum was received in the absence of the phantom material in the experimental setup for this. To remove the background noise in the dark environment, the same procedure was applied. The primary signal was then taken by subtracting the dark from the light. The phantom was then placed to the system, and the phantom's spectrum was recorded. The dark, which is background noise, was then eliminated to produce the real phantom signal. The "I<sub>0</sub>" data is represented by the main signal, while the "I" signal is represented by the real phantom signal. As a consequence, the following given formulas were used to extract macroscopic and microscopic optical characteristics from the acquired Main Signal (Light-Dark) and Real Phantom (Phantom-Dark) data.

### CALCULATION OF OPTICAL PROPERTIES

Optical properties such as absorbance, transmittance, reflectance, the refractive index, and optical attenuation coefficient were measured and calculated by using the following formulas.

$$R+T+A = 1 \text{ or } \%R + \%T + \%A = \%100 \quad [26] (5)$$

$$\text{Absorbance, } A; \quad A = -\log(I/I_0) = -\log(T) = 2 - \log(\%T) \quad [27] (6)$$

$$\text{Transmittance, } T; \quad T = I/I_0 \quad [27] (7)$$

$$\text{Reflectance, } R; \quad R = 1 - (A+T) \quad [26] (8)$$

$$\text{Reflectance, } R = \frac{(n-1)^2}{(n+1)^2}, \quad [26] (9)$$

where n is the Refractive Index.

$$I = I_0 e^{-\mu x}, \quad \mu = -\frac{\ln \frac{I}{I_0}}{x} \quad [28] (10)$$

Where  $\mu$  is the Linear Attenuation Coefficient.

The related microscopic formulas used in the calculations for absorption coefficient, scattering coefficient, reduced scattering coefficient, and total attenuation coefficient are as in the following.

The Kubelka-Munk Function is given by

$$F(R) = \frac{(1-R)^2}{2R} = \frac{k}{s} \quad [29] (11)$$

where R = Reflectance, k= Absorption Coefficient, s=Scattering Coefficient.

The total attenuation coefficient is described by

$$\mu = \mu_t = \mu_a + \mu_s \quad [30] (12)$$

Where  $\mu_a$  is Absorption Coefficient and  $\mu_s$  is Scattering Coefficient.

That is,  $k=\mu_a$  and  $s=\mu_s$  can be matched by using (11) and (12) formulas.

The reduced scattering coefficient ( $\mu'_s$ ) is defined by the following equation;

$$\mu'_s = (1 - g)\mu_s \quad [31] \quad (13)$$

Where  $g$  is the anisotropy factor. The  $g$  value of the phantom was used as 0.98 for the agar phantom.

**RESULTS AND DISCUSSION**

First of all, we give the optical and acoustic characterization results of the agar phantom to show that the agar phantom used in the experiments has real tissue properties. The phantom's tissue-mimicking features were validated acoustically. The sound speed was measured as  $1606,78 \pm 13$  m/s. Attenuation coefficient was measured as  $0.60 \pm 0.05$  dB·cm<sup>-1</sup>·MHz<sup>-1</sup>. And acoustic impedance was 1.70 MRayl. According to Mast's study [32], a liver tissue has the speed of sound as 1595 m/s. As seen, agar phantom has a liver-tissue characteristics. The macroscopic and microscopic optical properties of agar phantom were investigated using a spectrometer with a single integrated sphere and a broadband white light source in the wavelength range of 200 nm to 1000 nm. In fact, spectras were originally taken between 200 nm and 1000 nm. However, since the resolution of the signals was very high, the noise level was also very high. Moving average of the data was taken to reduce the noise level and get more smoother signals. For this

reason, the absorption spectrum range, shown in the Figure 3, was obtained between 400 nm and 1000 nm. All the experiments done for optical measurements were carried out under controlled laboratory ambient conditions (Temperature was  $23.5 \text{ }^\circ\text{C} \pm 0.2 \text{ }^\circ\text{C}$ , and Relative Humidity (RH) was  $50\% \pm 2\%$ ). In all graphs of repeated experiments, the individual maximum points were found and the average peak values were calculated. Then, using the absorbance values at the peak values in each measurement, all other optical parameters were calculated for this peak value using the formulations given above. By using these macroscopic optical properties, microscopic optical properties such as absorption coefficient, scattering coefficient, reduced scattering coefficient and total attenuation coefficient were calculated via Kubelka-Munk Function approach. We calculated the total attenuation coefficient from formula (10) and we know  $R =$  reflectance value, then we can solve these two equation (11) and (12) and find absorption and scattering coefficients. By the way, while calculating reduced scattering coefficient, we used 0.98 value for the agar phantom. The absorbance peak values we found for the agar phantom were in the range of  $645.55 \pm 61.05$  nm and the absorption coefficient was found to be  $0.050 \pm 0.008$  mm<sup>-1</sup>. This value is in good agreement with the absorption coefficient values given in the literature [33].

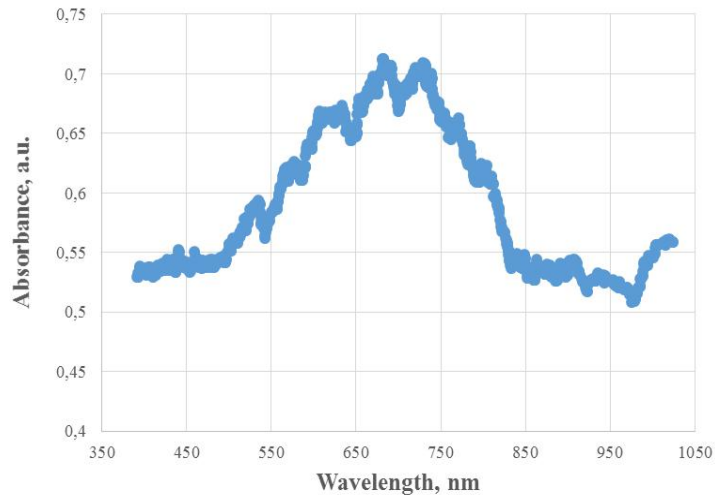


Fig. 3. Absorbance Spectrum of Agar Phantom.

The macroscopic optical properties of agar phantom such as absorbance, transmittance, reflectance, refractive index and attenuation coefficient, which was subtracted from the formulas at the peak values, were calculated as average in the Table I.

Table I.

The measured optical properties of the agar phantom as average

Phantom	Transmittance T	Absorbance A	Reflectance R	Refractive Index
Agar	$0.23 \pm 0.03$	$0.64 \pm 0.06$	$0.13 \pm 0.03$	$2.14 \pm 0.18$

The microscopic optical properties of agar phantom such as absorption coefficient, scattering coefficient, reduced scattering coefficient, and total attenuation coefficient were calculated as average in the Table II.

Table II.

The calculated microscopic optical properties of agar phantom at around maximum absorbance peak.

Phantom	Absorption Coefficient, $\mu_a, \text{cm}^{-1}$	Scattering Coefficient, $\mu_s, \text{cm}^{-1}$	Reduced Scattering Coefficient, $\mu'_s, \text{cm}^{-1}$	Total Attenuation Coefficient, $\mu_t, \text{cm}^{-1}$
Agar	$0.50 \pm 0.08$	$0.17 \pm 0.02$	$0.02 \pm 0.002$	$0.67 \pm 0.06$

After optically and acoustically characterizing the phantom and demonstrating that it has a true tissue-like structure, the temperature measurement results can now be given. The temperatures detected by the thermocouples within the agar phantom as a result of the light flushes of the IPL device were found as given in Table III below at different power levels of the device.

Table III.

Temperatures measured in thermocouples as °C inside the agar phantom with the application of different power levels of the IPL light source.

Power Level	1st Thermocouple	2nd Thermocouple	3rd Thermocouple	4th Thermocouple	Average (°C)
1st Power Level	$22,40 \pm 1,74$	$22,55 \pm 1,92$	$22,48 \pm 2,62$	$22,45 \pm 2,11$	$22,47 \pm 0,06$
2nd Power Level	$25,07 \pm 1,67$	$25,39 \pm 1,82$	$25,75 \pm 2,73$	$25,56 \pm 1,89$	$25,44 \pm 0,29$
3rd Power Level	$27,21 \pm 3,31$	$27,81 \pm 3,72$	$27,51 \pm 5,44$	$28,10 \pm 3,82$	$27,66 \pm 0,38$
4th Power level	$29,33 \pm 1,84$	$30,10 \pm 2,11$	$30,76 \pm 1,25$	$30,39 \pm 1,92$	$30,15 \pm 0,61$
5th Power Level	$32,56 \pm 0,46$	$33,79 \pm 0,76$	$34,09 \pm 1,64$	$33,21 \pm 1,17$	$33,41 \pm 0,68$

Average irradiance values calculated at different power levels of IPL device according to 0.80, 0.85, 0.90, .095 and 1.0 emissivity values can be seen between Figure 4 and Figure 8.

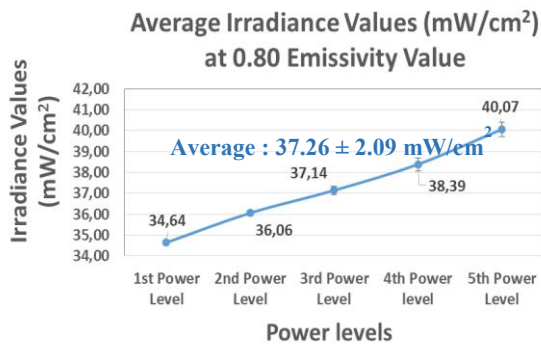


Fig. 4. The average calculated irradiances at 0.80 emissivity value.

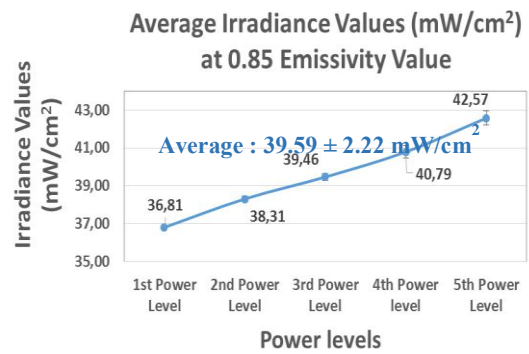


Fig. 5. The average calculated irradiances at 0.85 emissivity value.

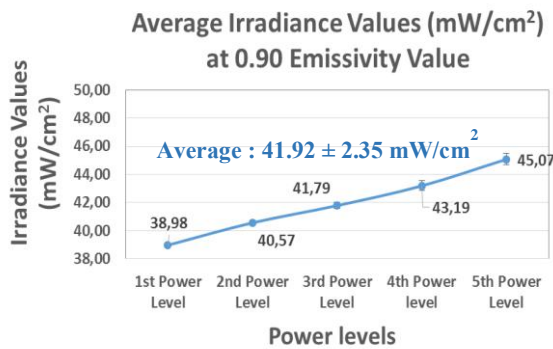


Fig. 6. The average calculated irradiances at 0.90 emissivity value

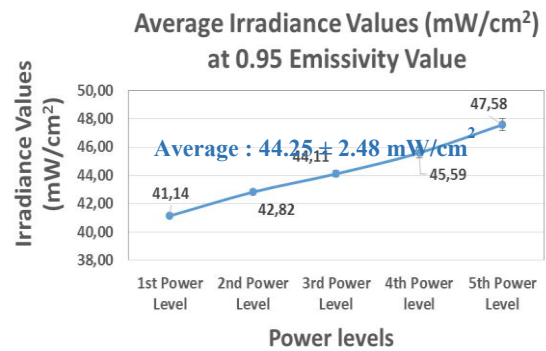


Fig. 7. The average calculated irradiances at 0.95 emissivity value.

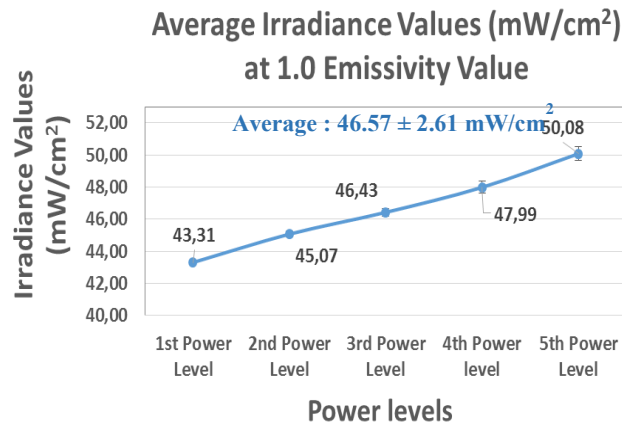


Fig. 8. The average calculated irradiances at 1.0 emissivity value.

The temperatures detected by the thermocouples within the agar phantom as a result of the different lights of the LED device were found as given in Table IV.

Table IV.

Temperatures measured in thermocouples inside the agar phantom with the application of different colors of the LED light source.

LED Color	The Measured Average Temperatures (°C)
Yellow	$18,18 \pm 0,32$
Blue	$18,74 \pm 0,15$
Orange	$18,92 \pm 0,11$
Purple	$19,08 \pm 0,11$
Red	$17,21 \pm 0,07$
Green	$17,32 \pm 0,06$

The irradiance values calculated at different emissivity values from the internal temperatures detected in the agar phantom using the LED therapy device can be seen between Figure 9 and Figure 13.

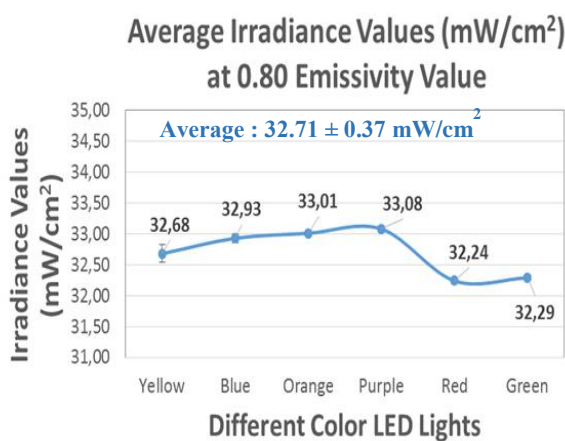


Fig. 9. The average calculated irradiances at 0.80 emissivity value.

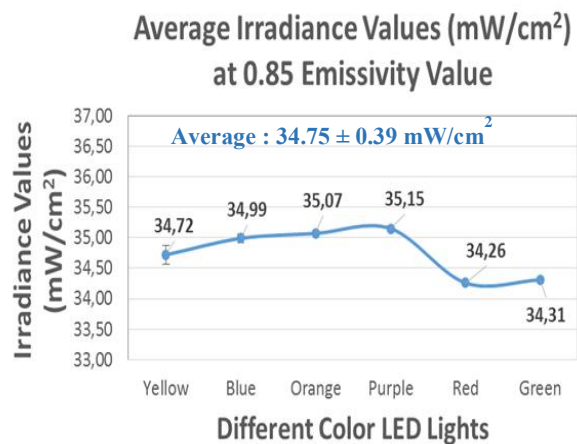


Fig. 10. The average calculated irradiances at 0.85 emissivity value.

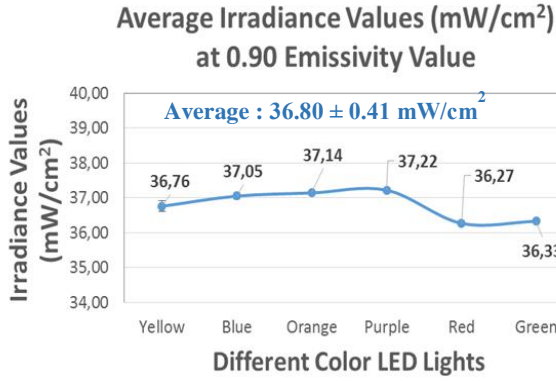


Fig. 11. The average calculated irradiances at 0.90 emissivity value.

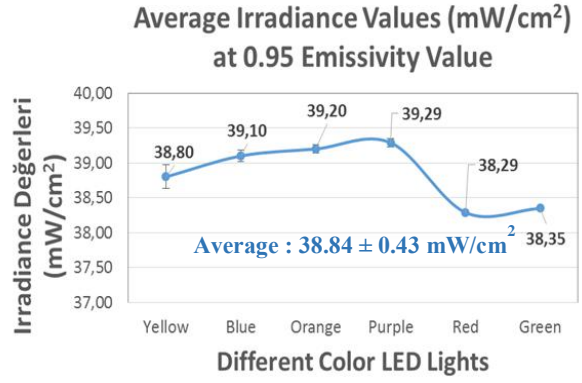


Fig. 12. The average calculated irradiances at 0.95 emissivity value.

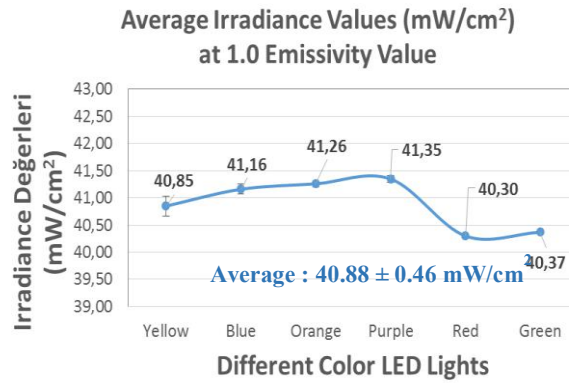


Fig. 13. The average calculated irradiances at 1.0 emissivity value.

The maximum temperatures detected by the thermocouples within the agar phantom as a result of the red color laser application at different time intervals and different distances from the laser source were found as given in Table V.

Table V.

Maximum temperatures measured in thermocouples inside the agar phantom with the application of red laser light source at different time intervals and different distances from the laser source.

The Measured Max. Temperature (°C) at	0 mm	5 mm	10 mm	15 mm	20 mm	25 mm
20 s	22.85	21.45	20.99	21.1	21.24	21.26
40 s	22.88	21.41	21.11	21.2	21.34	21.36
60 s	22.96	21.42	21.19	21.28	21.38	21.41
80 s	23.03	21.44	21.25	21.36	21.43	21.48

The irradiance values calculated at different emissivity values from the internal temperatures detected in the agar phantom using the red color laser can be seen between Table VI and Table X.

Table VI.

Irradiance values calculated for 0.80 emissivity value from the maximum internal temperatures

The Calculated Optical Intensity / Irradiance / Flux Density (mW/cm <sup>2</sup> ) at	0 mm	5 mm	10 mm	15 mm	20 mm	25 mm
20 s	34.82	34.17	33.96	34.00	34.07	34.08
40 s	34.84	34.15	34.01	34.05	34.12	34.13
60 s	34.88	34.16	34.05	34.09	34.14	34.15
80 s	34.91	34.16	34.08	34.13	34.16	34.18

Table VII.

Irradiance values calculated for 0.85 emissivity value from the maximum internal temperatures

The Calculated Optical Intensity / Irradiance / Flux Density (mW/cm <sup>2</sup> ) at	0 mm	5 mm	10 mm	15 mm	20 mm	25 mm
20 s	37.00	36.30	36.08	36.13	36.20	36.21
40 s	37.01	36.28	36.14	36.18	36.25	36.26
60 s	37.05	36.29	36.18	36.22	36.27	36.28
80 s	37.09	36.30	36.21	36.26	36.29	36.32

Table VIII.

Irradiance values calculated for 0.90 emissivity value from the maximum internal temperatures

The Calculated Optical Intensity / Irradiance / Flux Density (mW/cm <sup>2</sup> ) at	0 mm	5 mm	10 mm	15 mm	20 mm	25 mm
20 s	39.18	38.44	38.20	38.26	38.33	38.34
40 s	39.19	38.42	38.26	38.31	38.32	38.39
60 s	39.23	38.42	38.30	38.35	38.40	38.42
80 s	39.27	38.43	38.34	38.39	38.43	38.46

Table IX.

Irradiance values calculated for 0.95 emissivity value from the maximum internal temperatures

The Calculated Optical Intensity / Irradiance / Flux Density (mW/cm <sup>2</sup> ) at	0 mm	5 mm	10 mm	15 mm	20 mm	25 mm
20 s	41.35	40.58	40.32	40.38	40.46	40.47
40 s	41.37	40.55	40.39	40.44	40.52	40.53
60 s	41.41	40.56	40.43	40.48	40.54	40.55
80 s	41.45	40.57	40.47	40.53	40.56	40.59

Table X.

Irradiance values calculated for 1.0 emissivity value from the maximum internal temperatures

The Calculated Optical Intensity / Irradiance / Flux Density (mW/cm <sup>2</sup> ) at	0 mm	5 mm	10 mm	15 mm	20 mm	25 mm
20 s	43.53	42.71	42.45	42.51	42.59	42.60
40 s	43.55	42.69	42.51	42.57	42.65	42.66
60 s	43.59	42.69	42.56	42.62	42.67	42.69
80 s	43.63	42.71	42.60	42.66	42.70	42.73

When the average irradiance values calculated according to different emissivity values over the temperature data found for IPL, LED and laser experiments in the agar phantom, Figure 14 appears. As can be seen in Figure 14, the average irradiance values increase as the emissivity value increases. In other words, the irradiance value is directly dependent on the emissivity value. Therefore, it must be determined precisely.

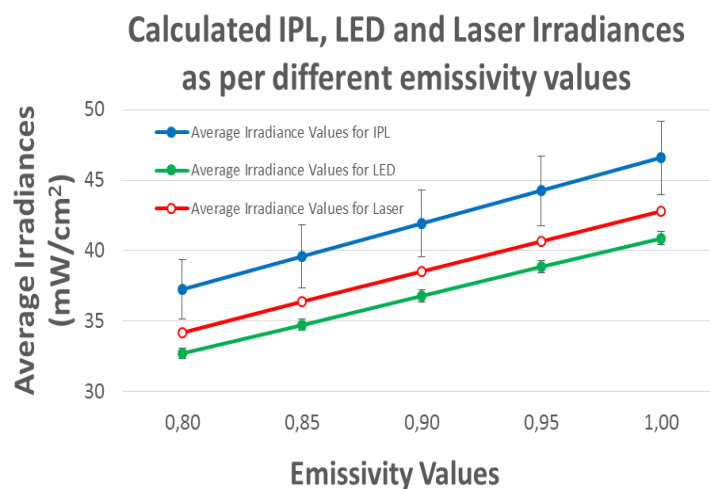


Fig. 14. The calculated IPL, LED and Laser irradiances at different emissivity value.

After determining the irradiance data, energy densities ( $J/cm^2$ ) can be calculated for different time periods and different emissivity values. For example, energy densities for each light therapy device (IPL, LED and Laser) at 0.9 emissivity value have been calculated as in Figure 15. In this way, others can be calculated and graphed. So, data of the calculated energy densities of IPL, LED and Laser therapy devices according to the emissivity data for 1 s are given in Table XI below. By the way, we also need to explain why we chose the emissivity coefficient as 0.90. Teper et al. [34], in their study on the agar phantom model, took the emissivity value as 0.8, 0.85, 0.9 and 0.95.

They obtained optimum results at 0.95 emissivity value. They explained that this emissivity value was compatible with the emissivity value of water, which was the main construction material of the phantom. Also in a doctoral study made by Sichao Hou, the emissivity value for agarose (the same material we used in our study) was stated that the agarose gel fluctuates at four different emissivity concentrations in the range of 0.88 to 0.92, so they use an average of 0.90 for the agarose gel over the temperature range of 25 to 70 °C [23]. Therefore, we took the emissivity coefficient as 0.90.

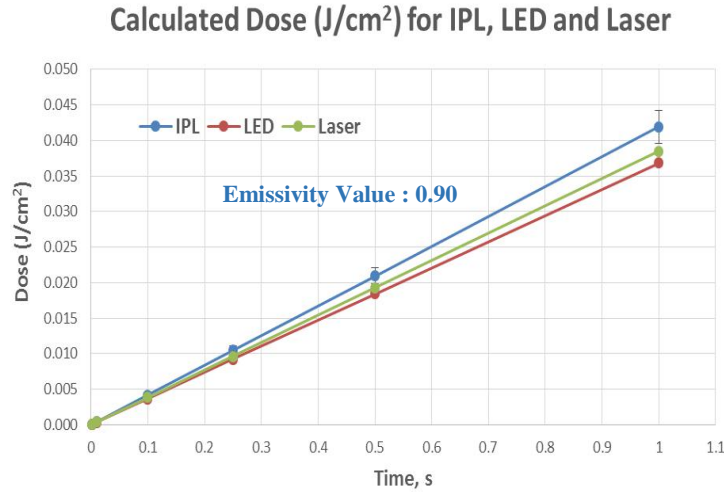


Fig. 15. The calculated energy density of IPL, LED and Laser therapy devices at 0.9 emissivity value.

Table XI.

Energy densities calculated for IPL, LED and Laser for 1 second.

Emissivity Value	Energy Density for IPL ( $J/cm^2$ )	Energy Density for LED ( $J/cm^2$ )	Energy Density for Laser ( $J/cm^2$ )
0.80	$0.04 \pm 0.002$	$0.03 \pm 0.0004$	$0.03 \pm 0.00004$
0.85	$0.04 \pm 0.002$	$0.03 \pm 0.0004$	$0.04 \pm 0.00004$
0.90	$0.04 \pm 0.002$	$0.04 \pm 0.0004$	$0.04 \pm 0.00004$
0.95	$0.04 \pm 0.002$	$0.04 \pm 0.0004$	$0.04 \pm 0.00004$
1.00	$0.05 \pm 0.003$	$0.04 \pm 0.0005$	$0.04 \pm 0.00005$
Average	$0.04 \pm 0.002$	$0.04 \pm 0.0004$	$0.04 \pm 0.00004$

In the literature, there are determined energy densities (fluence) for the treatment of various diseases with light. For example, for open wound healing, this dose value is  $2 J/cm^2$ . Total number of treatments are given as 3-10 times and time interval between treatments are 2-3 days [35]. When we divide  $2 J/cm^2$  by the values given in Table IX for each emissivity value, we get the durations required to reach 2 J. This value as averages are  $48 \pm 4.2$  s for IPL,  $55 \pm 4.8$  s for LED and  $52 \pm 4.6$  s for laser. The average of all these devices was calculated as  $51.7 \pm 3.4$  s. Again for acne vulgaris, this dose value is given as 2-5  $J/cm^2$ . Total number of treatments are given as 4-10 times and time interval between treatments are 2-3 days. The average times for max. value ( $5 J/cm^2$ ) are  $120.0 \pm 10.6$  s for IPL,  $136.7 \pm 12.1$  s for LED and  $130.7 \pm 11.6$  s for

laser. The average of all these devices for acne vulgaris treatment was calculated as  $129.1 \pm 8.5$  s. For acute pain, this dose value is stated as 5-50  $J/cm^2$ . Total number of treatments are given as every day (new injuries), max 3 days. The average times for max. value ( $50 J/cm^2$ ) are  $1200.2 \pm 106.1$  s for IPL,  $1367.3 \pm 120.8$  s for LED and  $1306.5 \pm 115.5$  s for laser. The average of all these devices for acne vulgaris treatment was calculated as  $1291.4 \pm 84.6$  s.

## CONCLUSION

In conclusion, with this study, it was clearly demonstrated the importance of emissivity coefficient for the irradiance and energy density and thus dose calculations on well-characterized tissue phantom by using light sources having low power intensities. In

addition, it has been shown that emissivity values are very critical in the evaluation of the treatment

application times required for the treatment of various diseases with light.

- [1] B. Zhang, X. Huang, S. Huo et al. Effect of photobiomodulation therapy on mini-implant stability: a systematic review and meta-analysis. *Lasers Med Sci* 36, 2021. 1557–1566.
- [2] M.A. Vetrici, S. Mokmeli, A.R. Bohm, M. Monici, S.A. Sigman. 2021. Evaluation of Adjunctive Photobiomodulation (PBMT) for COVID-19 Pneumonia via Clinical Status and Pulmonary Severity Indices in a Preliminary Trial. *Journal of inflammation research*, 14, 965–979.
- [3] P.G. Vassão, J. Parisi, T.F.C. Penha et al. Association of photobiomodulation therapy (PBMT) and exercises programs in pain and functional capacity of patients with knee osteoarthritis (KOA): a systematic review of randomized trials. *Lasers Med Sci* 36, 2021. 1341–1353.
- [4] Vinh Van Tran, Minhe Chae, Ju-Young Moon, Young-Chul Lee. Light emitting diodes technology-based photobiomodulation therapy (PBMT) for dermatology and aesthetics: Recent applications, challenges, and perspectives, *Optics & Laser Technology*, Volume 135, 2021, 106698.
- [5] H. Shojaei, Y. Sokhangoei, M.R. Soroush. 2008. Low level laser therapy in the treatment of pressure ulcers in spinal cord handicapped veterans living in Tehran. *Iranian Journal of Medical Sciences*, 33(1), 44-48.
- [6] T. Bavaresco, A.D.F. Lucena. 2021. Low-laser light therapy in venous ulcer healing: a randomized clinical trial. *Revista brasileira de enfermagem*, 75.
- [7] R.K. Mathur, K. Sahu, S. Saraf, P. Patheja, F. Khan, P.K. Gupta. 2017. Low-level laser therapy as an adjunct to conventional therapy in the treatment of diabetic foot ulcers. *Lasers in medical science*, 32 (2), 275-282.
- [8] J. Verbelen. 2007. Use of polarised light as a method of pressure ulcer prevention in an adult intensive care unit. *Journal of wound care*, 16,4, 145-150.
- [9] H.A. Elessawy, W.H. Borhan, N.A. Ghozlan, S.H. Nagib. 2021. Effect of light-emitting diode irradiation on chronic nonhealed wound after below-knee amputation. *The International Journal of Lower Extremity Wounds*, 20, 3, 251-256.
- [10] R.M. Ramos, M. Burland, J.B. Silva, L.M. Burman, M.S. Gelain, L. M. Debom, J. Valmier. 2019. Photobiomodulation improved the first stages of wound healing process after abdominoplasty: an experimental, double-blinded, non-randomized clinical trial. *Aesthetic plastic surgery*, 43 (1), 147-154.
- [11] I. Frangež, T. Nizič-Kos, H. B. Frangež. 2018. Phototherapy with LED shows promising results in healing chronic wounds in diabetes mellitus patients: a prospective randomized double-blind study. *Photomedicine and Laser Surgery*, 36(7), 377-382.
- [12] de Barros Araújo Júnior, R. Gonzaga, I.C.A. Fernandes, G.A. Lima, A.C.G. Cortelazzi, P.S.T. de Oliveira, R.A. Nicolau, R.A. 2018. Low-intensity LED therapy ( $\lambda$  640±20 nm) on saphenectomy healing in patients who underwent coronary artery bypass graft: a randomized, double-blind study. *Lasers in Medical Science*, 33(1), 103-109.
- [13] A.C.G. Lima, G.A. Fernandes, de Barros Araújo, R. Gonzaga, I.C. de Oliveira, R.A. Nicolau, R.A. 2017. Photobiomodulation (laser and LED) on sternotomy healing in hyperglycemic and normoglycemic patients who underwent coronary bypass surgery with internal mammary artery grafts: A randomized, double-blind study with follow-up. *Photomedicine and laser surgery*, 35(1), 24-31.
- [14] M.J. Al Abdullah, Y.G. Mahdi. 2022. Intense pulsed light versus benzoyl peroxide. *Journal of Population Therapeutics and Clinical Pharmacology= Journal de la Therapeutique des Populations et de la Pharmacologie Clinique*, 28(2), e54-e61.
- [15] W. Oentari, A.R. Sutrisno, N.K. Jusuf, K. Nasution. 2022. Intense pulsed light (IPL) as adjuvant therapy for acne vulgaris: A case series. *Journal of General-Procedural Dermatology and Venereology Indonesia*, 175-181.
- [16] A. Deshpande. 2022. Efficacy & safety of intense pulsed light therapy for unwanted facial hair: a retrospective analysis in skin of color. *Journal of Cosmetic and Laser Therapy*, 1-6.
- [17] M. Abrouk, J. Dong, J. S. Waibel. 2022. Medical and aesthetic improvement of photodamaged skin by the combination of intense pulsed light and photodynamic therapy with 10% aminolevulinic acid hydrochloride gel. *Lasers in Surgery and Medicine*, 54(1), 62-65.
- [18] Giannaccare, Giuseppe MD, PhD, FEBOPht\*; Pellegrini, Marco MD, FEBOPht†,‡,§; Carnovale Scalzo, Giovanna MD\*; Borselli, Massimiliano MD\*; Ceravolo, Domenico OD\*; Scorcìa, Vincenzo MD\* Low-Level Light Therapy Versus Intense Pulsed Light for the Treatment of Meibomian Gland Dysfunction, *Cornea*: February 3, 2022 - Volume - Issue - doi: 10.1097/ICO.0000000000002997
- [19] B. Karaböce, E. Çetin, H.O. Durmuş, M. Özdingiş, H. Öztürk, K. Mahmat, M.A. Güler. 2018. Investigation of Different TMMs in High Intensity Focused Ultrasound Applications. In 2018 IEEE International Symposium on Medical Measurements and Applications (MeMeA) (s. pp. 1-5). IEEE.
- [20] H.O. Durmuş, S. Kocaata, G. Naz, Çelik, Y.E. Çetin, E. Karaböce, B. Seyidov, M.Y. 2020, June. Investigation of Basic Optical Properties of Tissue Phantoms Under 635 nm Low-Level Laser

- Irradiation. In 2020 IEEE International Symposium on Medical Measurements and Applications (MeMeA) (pp. 1-6). IEEE.
- [21] *H.O. Durmuş, E.Ç. Arı, B. Karaböce, M.Y. Seyidov.* 2020. Measurements of temperature and optical power caused by an IPL therapy device on an artificial tissue. *Results in Optics*, 1, 100001.
- [22] *H.O. Durmuş, E. Çetin, E. Demirkıran, B. Karaböce, M.H.Y. Seyidov.* 2019, November. Investigation of the temperature effect of the LED therapy device on tissue-mimicking material. In *AIP Conference Proceedings* (Vol. 2178, No. 1, p. 030002). AIP Publishing LLC.
- [23] *S. Hou.* 2018. Photo-thermally enhanced temperature gradient gel electrophoresis for DNA separation (Doctoral dissertation, Northeastern University).
- [24] *M. Wellons.* 2007. The Stefan-Boltzmann Law. Physics Department, The College of Wooster, Wooster, Ohio, 44691.
- [25] <https://heliotherapyreviews.com/red-light/red-light-therapy-dosingguide/>
- [26] *M.Y. Nadeem, W. Ahmed.* 2000). Optical properties of ZnS thin films. *Turkish Journal of Physics*, 24(5), 651-659.
- [27] *D.T. Harvey.* 2003. *Analytical Chemistry for Technicians* (3rd Edition b.). John Kenkel.
- [28] *S. Chang, A.K. Bowden.* 2019. Review of methods and applications of attenuation coefficient measurements with optical coherence tomography. *Journal of biomedical optics*, 24(9), 090901.
- [29] *J.O. Torrent, V. Barrón.* 2008. Diffuse reflectance spectroscopy. *Methods of Soil Analysis Part 5. Mineralogical Methods*, 5, 367-385.
- [30] *B.C. Wilson.* 1995. Measurement of tissue optical properties: methods and theories. In *Optical-thermal response of laser-irradiated tissue*. Springer, Boston, MA.
- [31] *E.J. Jeong, H.W. Song, Lee, Y.J. Park, S.J. Yim, M. J. Lee, S.S. Kim, B. K.* 2017. Fabrication and characterization of PVCP human breast tissue-mimicking phantom for photoacoustic imaging. *BioChip Journal*, 11(1), 67-75.
- [32] *T.D. Mast.* 2000. Empirical relationships between acoustic parameters in human soft tissues. *Acoustics Research Letters Online*, 1(2), 37-42.
- [33] *L. Ntombela, B. Adeleye N. Chetty.* 2020. Low-cost fabrication of optical tissue phantoms for use in biomedical imaging. *Heliyon*, 6(3), e03602.
- [34] *M. Tepper, A. Shoval, I. Gannot.* 2015. The effect of geometry on tumor thermal profile and its use in tumor functional state estimation. *Journal of biophotonics*, 8(3), 258-264.
- [35] <https://energy-laser.com/guide-lines-for-treatment-with-laser-therapy/>

*Received: 01.07.2022*

## ON THE THEORY OF DISPERSION INTERFEROMETER WITH TWO NONLINEAR CRYSTALS

**Sh.Sh. AMIROV**

*Faculty of Physics, Baku State University, 23 Z. Khalilov str., Az-1148, Baku, Azerbaijan*

*Department of Medical and Biological Physics, Azerbaijan Medical University*

*167 S. Vurgun str., Az-1022, Baku, Azerbaijan*

*Department of Physics and Electronics, Khazar University, 41 Mahsati str., Az 1096,*

*Baku, Azerbaijan*

*E-mail: [phys\\_med@mail.ru](mailto:phys_med@mail.ru)*

Theory of double crystal dispersion interferometer is given in the constant intensity approximation taking into account the reverse reaction of excited harmonics on the phase of fundamental wave. It was shown that unlike the traditional interferometers the dispersion interferometer is not sensitive to the mechanical vibrations and intensity of second harmonics is a function of electron density in a plasma medium.

**Keywords:** dispersion interferometer, second harmonic generation, plasma electron density.

**PACS:** 95.75 Kk; 42.65-k; 42.25 Hz; 42.62-b

### 1. INTRODUCTION

It is known that conducting controlled thermo nuclear fusion is one of the most important things that can be done by plasma. In order to control the plasma and determine the electron density the thermo-nuclear devices should have higher reliability and resolution. Currently purposeful research works are being carried out in the direction of obtaining plasma media with stable parameters at higher temperatures and electron concentration as well as long retention time etc. At temperatures (about  $10^8 K$ ) required for nucleus synthesis all atoms are ionized, ordinary metals are vaporized and storage of plasma becomes impossible. For this purpose the magnetic fields are employed. It was possible to increase the storage time of plasma with the toroidal camera having magnetic coils. In order to have a mutual interaction the plasma should possess significant higher density during retention. According to S.D.Louison criterion when condition  $n\tau \geq 3 \cdot 10^{14} s | cm^3$  ( $n$  – refers to electron density,  $\tau$  – is the retention time) is met the amount of energy obtained in the nuclear reactor becomes more than the expended energy. From this point of view determination of the electron density of plasma as its important characteristics becomes actual problem. There are polarimetric methods based on Faraday's and Cotton-Mouton effects [1-5]. As it was described in those works a monochromatic light beam whose polarization plane makes angle of  $45^\circ$  with respect to the magnetic field passes through plasma medium in between poles of electromagnet. The plasma possess optical anisotropy in the magnetic field (its optical axis is parallel to the magnetic field vector- $H$ ). Then the light undergoes the elliptical polarization i.e. propagates as the ordinary and extraordinary two waves with different phase velocities in the plasma medium. Difference in the refractive indices of ordinary and extraordinary waves is then given by  $n_{q|a} - n_a = CH^2 \lambda$ . Here  $H$  – is the magnetic field

intensity,  $C$  – Cotton-Mouton coefficient,  $\lambda$  – refers to the wavelength of light.

The electron density of plasma is determined by the dispersion of refractive index. To determine the electron density in addition to polarimeters the interferometric methods are widely used too (for examp.heterodine [6,7]). In traditional interferometers optical path instability due to mechanical vibrations produces an additional phase shift which causes errors in the measurement of plasma electron density. To compensate effect of vibrations in the determination of the phases the massive vibration isolators- solid frames, the far IR radiation, as well as the double colored interferometer with two different wavelengths can be used. Realization of interferometric system on the rigid frame with large sizes in the plasma burning equipment may create some difficulties. Also the use of long waves is related to the influence of refraction as well as the existence of density gradient in plasma equipment. Shortcomings related to the small differences in optical paths and wave fronts are eliminated by use the dispersion interferometers [8-11]. The dispersion interferometers have been offered for diagnosis of micro-relief on the surface of optical elements [8, 9], for determination the electron density in a laser spark [10], as well as the arc discharge of argon laser [11]. Dispersion interferometers also can be successfully used for determination the refractive index and thickness of transparent micro-objects as well as for sanitary-hygienic purposes. Unlike the traditional interferometers the waves travel the same geometrical path in dispersion interferometers.

The operational principle of dispersion interferometer composed of two crystals and plasma placed between them is widely presented in [9, 10, 12]. A portion of fundamental wave with frequency  $\omega$  is converted to the second harmonics with frequency  $2\omega$  (its polarizatin plane is perependicular to that of fundamental wave) in the first crystal. As a result those two waves travel roughly identical geometrical paths in the plasma. In the second crystal these waves

again interact with each other. An interference of first and second harmonic waves is analyzed in the constant field approximation (CFA) in which a variation in the amplitude and phase of fundamental wave is not taken into account [8, 9,10,11]. Reverse reaction of harmonic wave on the fundamental wave is considered in [12], for the absence of linear losses and occurrence of phase matching condition.

## 2. THEORETICAL APPROACH

In this paper a theory of dispersion interferometer with two nonlinear optical crystals is analyzed in the constant intensity approximation (CIA) [13]. Unlike the constant field approximation (CFA) no restrictions are imposed to the phases of interacting waves in CIA. Note that this approximation was successfully employed in previously studies [14-21]. This circumstance has allowed to find the intensity of harmonic wave at the output of second crystal as a function generalized phase shift between interacting waves. Since variation in phases causes change in output intensity, finding variations in intensity makes

possible to determine dispersion of refractive index of plasma and hence its electron density. Generation of second harmonics in both nonlinear crystals is considered by use the set of reduced equations given for complex amplitudes of interacting waves

$$\frac{dA_1}{dz} + \delta'_1 A_1 = -i\gamma'_1 A_2 A_1^* \exp(i\Delta_2 z) \quad (1)$$

$$\frac{dA_2}{dz} + \delta'_2 A_2 = -i\gamma'_2 A_1^2 \exp(-i\Delta_2 z)$$

where  $\delta'_{1,2}$ - refer to the linear losses for the fundamental wave of frequency  $\omega_1$  and second harmonics of frequency  $\omega_2 = 2\omega_1$ .  $A_{1,2}$ - are the complex amplitudes of interacting waves,  $\gamma'_{1,2}$  - indicate nonlinear coefficients of coupling,  $\Delta_2 = k_2 - 2k_1$  - is the difference in wave numbers for the second crystal. Note that the parameter  $\Delta$  has an important role in the spatial distribution of electromagnetic waves.

Differentiation of second equation of (1) with respect to the z- coordinate yields

$$\frac{d^2 A_2}{dz^2} + (2\delta'_1 + \delta'_2 + i\Delta_1) \frac{dA_2}{dz} + [2\gamma'_1 \gamma'_2 I_1 + \delta'_2 (2\delta'_1 + i\Delta_1)] A_2 = 0 \quad (2)$$

As distinct from the first crystal the complex amplitudes of waves at the input of second crystal are determined by their values at the exit from the first crystal and properties of plasma medium :

$$A_{1,2}(z=0) = A_{1,2}(l_1) \exp[i\varphi_{1,2}(l) + i\varphi_{1,2}(L)] \quad (3)$$

where, L- is the path travelled by the waves in plasma medium,  $\varphi_{1,2}$  - are the phases due to mechanical vibration as well as due to passage of waves along the plasma,  $z=0$  corresponds to the entrance of second crystal. Solution of (2) with boundary conditions (3) for complex amplitude of second harmonics at the output of second crystal is

$$A_2(z) = A_2(l_1 + L) \cdot e^{-\frac{\delta_2 + 2\delta_1 + i\Delta_2}{2} z} \left\{ \cos \lambda_2 z - \left[ \frac{\delta_2 - 2\delta_1 - i\Delta_2}{2\lambda_2} - \left( \frac{\lambda_1}{\lambda_2} \operatorname{ctg} \lambda_1 l_1 + \frac{\delta_2 - 2\delta_1 - i\Delta_1}{2\lambda_2} \right) \cdot e^{i\psi} \right] \operatorname{xsin} \lambda_2 z \right\} \quad (4)$$

Expression for the amplitude  $A_2(l_1)$  in (4) is given [21] by

$$A_2(l_1) = -i\gamma_2 A_{10}^2 \operatorname{sinc} \lambda_1 l_1 \cdot \exp \left[ -(\delta_2 + 2\delta_1 + i\Delta_1) \frac{l_1}{2} \right] \quad (5)$$

where

$$\lambda_1^2 = 2\Gamma_1^2 - \frac{(\delta_2 - 2\delta_1 - i\Delta_1)^2}{4}, \quad \Gamma_1^2 = \gamma_1 \gamma_2 I_{10}, \quad \lambda_2^2 = 2\Gamma_2^2 - \frac{(\delta_2 - 2\delta_1 - i\Delta_2)^2}{4}, \quad \Gamma_2^2 = \gamma_1 \gamma_2 I_1(l_1),$$

$$I_1(l_1) = I_0 e^{\frac{\delta_2 + 2\delta_1}{2} l_1} \times \left[ \left( \cos \lambda_1 l_1 + \frac{\delta_2 - 2\delta_1}{2\lambda_1} \sin \lambda_1 l_1 \right)^2 + \frac{\Delta_1^2}{4\lambda_1^2} \sin^2 \lambda_1 l_1 \right]^{1/2}, \quad (6)$$

On the basis of (4) output intensity of second harmonics is determined by

$$I_{2,out.} = I_2(l_1) \exp[-(\delta'_2 + 2\delta'_1)l_2] \times \left| \sin \lambda_2 l_2 \left[ b + \frac{\gamma'_2}{\gamma_2} \left( \frac{\lambda_1}{\lambda_2} a + c \right) \cdot \exp(i\psi) + d \right] \right|^2 \quad (7)$$

where  $a = \tan^{-1} \lambda_1 l_1$ ,  $b = \tan^{-1} \lambda_2 l_2$ ,  $c = \frac{\delta_2 - 2\delta_1 - i\Delta_1}{2\lambda_2}$ ,  
 $d = \frac{2\delta'_1 - \delta'_2 + i\Delta_2}{2\lambda_2}$

According to equation (7) intensity of harmonic wave is a function common phase difference  $\psi$  which in turn depends on the phase shift in the plasma medium

$$\psi = \Delta_1 l_1 + \Delta\varphi \quad (8)$$

here  $\Delta_1$  - is the difference in wave number for the first crystal,  $l_1$  - is the length of the first crystal. Using the simple relationship  $\Delta\varphi = \frac{2\pi}{\lambda} \Delta l$  between phase of wave and optical path difference through the plasma can be seen that if a small optical path difference due to mechanical vibrations is for instant,  $l$  then phases for the waves with the given frequencies are given by  $\varphi_1 = \frac{\omega}{c} l$  and  $\varphi_2 = \frac{2\omega}{c} l$ . However the quantity of phase difference becomes zero and hence the phase shift related to the mechanical vibrations disappears. This property shows main advantage of dispersion interferometer i.e. phase difference is determined with dispersion of plasma and is independent on the travelled geometrical path. By use the expression for the dispersion of plasma [6]

$$n(\omega) = 1 - \frac{2\pi n_e e^2}{m\omega^2}$$

for the phase difference in plasma we get

$$\Delta\varphi = \frac{3}{2} \frac{e^2}{mc^2} \lambda \langle n_e L \rangle \quad (9)$$

here  $e$  - is the charge of electron,  $m$  is the mass of electron,  $c$ - refers to the speed of propagation of radiation,  $\lambda$  - indicates wavelength of laser radiation,  $n_e$  - is the electron density in plasma medium.

### 3. CONCLUSIONS

As the intensity of second harmonic is a function of electron density in plasma this quantity can be found through determination the maxima and minima of intensity. Comparison of interference patterns in the existence as well absence of investigated plasma medium a dispersion of refractive index can be determined due to shifts of pattern. Sensitivity of interferometer can be increased through performance nonlinear conversion of frequencies in resonator. This interferometric system based on the second harmonic generation can be used in modern equipment of nuclear synthesis for diagnosis of plasma as well as in the plasma burning experiments.

- 
- [1] Y. Kawano, S. Chibi and A. Inoue. Rev. Sci., Instrum., 2001, 72, 1068.
  - [2] T. Akiyama, K. Kawata, Y. Ito, S. Okajima et.al. Rev. Sci. Instrum, 2006, 77, 10F118.
  - [3] M.A. Van Zeeland, R.L. Boivin, T.N. Carlstom and T.M. Daterly. Rev.Sci.Instrum, 2008,79, 10E719.
  - [4] Ch. Fuchs and H.J. Hartfuss. Phys. Rev.Lett. 1998, 81, 1626.
  - [5] Boboc, L. Zabeo and A.Murari. Rev.Sci. Instrum 2006, 77, 10F324.
  - [6] P.A. Bagryansky, A.D. Khilchenko, A.N. Kvashin, A.A.Lizunov, R.V. Voskoboynikov, A.L. Solomakhin, H.R. Koslowski. Rev. of Sci.Instrum. 2006, 77, 053501.
  - [7] T. Akiyama, K.Kawahata, S. Okajima and K. Nakayama. Proceedings of ITC 18, 2008, P2-34, pp.401-405.
  - [8] G.V Ostrovskaya et.al. A.C. 864842, B.I. 1981, № 38.
  - [9] F.A. Hopf, A. Tomita and G.AI-Jumaily. Opt.Lett. 1980, 5, pp.386-388.
  - [10] Kh.P. Alum, Y.V. Kovalchuk, G.V. Ostrovskaya. Letters to JETP, 1981, v.7, №22, pp.1359-1364.
  - [11] A.N. Azarenko, G.B.Altusher, N.R. Belashenkov, S.A. Kozlov. Kvantovaya elektronika., 1993, v.20, № 8, pp.733-756.
  - [12] V.N. Drachev. Optics and Spectroscopy , 1993, v.75, №2, pp.473-479.
  - [13] Z.H. Tagiev, A.S. Chirkin. JETP 1977, v.73, №4, pp.1271-1282.
  - [14] R.J. Kasumova, Sh.Sh. Amirov, Sh.A. Shamilova. Quantum Electro nics., 2017, vol.47, № 7, pp.655-660.
  - [15] R.J. Kasumova, Sh.Sh. Amirov, Z.H.Tagiyev , Sh.A. Shamilova, G.A. Safarova. Journal of Russian Laser research., July 2017, vol.38, № 4, pp.211-218.
  - [16] R.J. Kasumova, Sh.Sh. Amirov. Superlattices and microstructures., 2018, 126, pp. 49-56.
  - [17] Sh.Sh.Amirov. AJP “Fizika”(EN) 2021, vol. XXVII №1, pp.8-12.
  - [18] R.J. Kasumova, Z.A.Tagiev, Sh.Sh. Amirov. “News of Baku University”, Series of physico-mathe-matical sciences №1, 2021 pp.72-82.
  - [19] Sh.Sh. Amirov. AJP “Fizika”(EN) Vol.XXVII 2022, №1, pp.13-17.
  - [20] R.J. Kasumova, Sh.Sh. Amirov. AJP “Fizika” (EN) Vol.XXVII, 2022, №2, pp.24-30.
  - [21] Z.H. Tagiev , R.J. Kasumova, R.A. Salmanova, N.V. Kerimova. Optics and Spectroscopy, 2001, v.91, № 6, pp.968-971.

Received: 01.09.2022

## PLASMA ETCHING OF GaAs SURFACE IN A PLANAR GAS DISCHARGE SYSTEM

B.G. SALAMOV <sup>a</sup> and T.G. MAMMADOV <sup>b</sup>

<sup>a</sup> *Physics Department, Faculty of Arts and Sciences, Gazi University, Beşevler 06500 Ankara, Turkey*

<sup>b</sup> *Azerbaijan National Academy of Sciences, Institute of Physics, AZ-1143 Baku, Azerbaijan*

This paper analyses the surface behaviour of etched a large-diameter GaAs plate realized by recording the spatial distribution of the gas discharge light emission (DLE) in a planar gas discharge system (PGDS) in ambient air and room temperature. The etching depth is measured by surface profilers as a function of a gap spacing and gas pressure. The analysis of the surface homogeneity is determined by fractal dimension of the gas DLE when a limiting current is passed through a discharge cell. The effect on the roughness of the GaAs surface through the plasmachemical processes at appropriate set of experimental parameters was established. The surface images of the etched GaAs are analysed using both the profile and spatial distribution DLE intensity data showing the surface inhomogeneity in the GaAs plate. It is quantitatively concluded that plasma etching at certain experimental condition can cause an improvement in surface structure of GaAs plate and spatial distribution DLE in a PGDS. The results obtained in this work suggest that a PGDS can be an efficient, alternative plasma source for general surface processing, because they can provide nonthermal discharges also near atmospheric pressures and thereby eliminate the need of costly vacuum systems.

**Keywords:** Plasma etching, GaAs plate, gas discharge system, surface processing, discharge light emission.

**PACS:** 61.50L -structure of bulk crystals, 81.40-treatment of materials and its effects on microstructure, nanostructure and properties

### 1. INTRODUCTION

The III-V compound semiconductors, such as GaAs and InP, have been long recognised for their potential applications in high speed electronic and optoelectronic circuits. The technology of reducing the negative effects of poor surface and interface is referred to as plasmachemical processes, the objective of which is to stabilise the properties of the surface so that it becomes immune to exposure of the device to operating ambient [1]. Plasmachemical processes have proved to be very useful methods for cleaning, etching, or material deposition on surfaces and have enabled the production of new and advanced materials for a variety of technical applications [2-4]. In all surface-processing techniques using plasmas, activated species (e.g., ions, electrons, photons, radicals and metastables from the working or background gas) [4,5] are generated within the plasma which then undergo chemical and physical reactions with the surface material. Examples are etching of Si and SiO<sub>2</sub> with X (where X = F or Cl) from NX<sub>3</sub>, CX<sub>4</sub>, C<sub>2</sub>X<sub>6</sub>, or C<sub>3</sub>X<sub>8</sub> in the semiconductor industry, degreasing of metal parts by O(<sup>3</sup>P) and O(<sup>1</sup>D), O<sub>2</sub>(<sup>1</sup>Δ), and O<sub>3</sub> in the metal industry [6] or coating of materials with polymers or other materials in various industry branches [3,7,8].

A planar gas discharge system (PGDS) with a semiconducting cathode has found numerous applications in the last decade, especially in the registration of IR images. High speed photography, non-silver image formation and devices for rapid visualization of electrical and structural defects in semiconductors are the other interesting applications

of these systems [9-11]. It is known [11] that if one of the electrodes is made in the form of a GaAs plate with a resistivity greater than 10<sup>6</sup> Ωcm in a PGDS cell, the gas discharge current can be distributed over the whole area of the electrodes causing a gas DLE. The uniformity of the DLE depends on the resistivity distribution of the GaAs plate, and the light emission intensity is proportional to the discharge current. Local changes in the resistivity of the GaAs plate leads to local changes in the current and the gas DLE. The current and DLE intensity depend on the local parameters of the GaAs plate, and therefore inhomogeneities in the GaAs plate are visualized in the form of irregularities in the DLE.

The presence of many electronically active defect states results in poorer device performance and reliability. Therefore, preparation of surface with acceptable levels of electronically active defects is essential for proper functioning of many devices. Unfortunately, the fundamental knowledge of the surfaces has been very limited and the research of reducing the negative effects of poor surface and interface, for Si and III-V compound semiconductors, has been primarily based on empirical techniques [1]. It is recognized that the development of GaAs semiconductor technology is directly related to the surface properties of GaAs. Hence, the control and precision in surface treatment such as the cleaning and etching processes is becoming increasingly critical in devices occur [12]. The methods for visualization the surface homogeneities of GaAs plates of large diameter are of great interest for the electronics industry and laboratory studies [11]. Therefore, any relevant evaluation of the homogeneity of

semiconductor requires description of the spatial distribution both of surface roughness and of structural defects. Moreover, in addition to provide an image of the GaAs plate, analysis of this image is important to confirm the homogeneities spatially in a PGDS with a semiconductor cathode.

In contrast to discharge devices with metal electrodes, the voltage drop in the discharge gap of a laterally extended semiconductor gas discharge cell is localized. These cells are more stable against the current filamentation because there exists negative feedback caused by the appearance of tangential components of the electric field in the case of imposing on the system an inhomogeneous fluctuation of  $j$  [13,14]. As a result, instabilities of the “fluctuation” type may not occur. Mechanisms for this include distortion of the field by the space charge, gas heating, or the dependence of the secondary electron emission factor  $\gamma$ , on the ion energy and hence on the strength of the field at the semiconductor. The presence of a resistive electrode also affects the development of instabilities of the ionization-overheating type. It was shown in [15] that in a PGDS with the Townsend discharge, the resistive electrode reduces the growth rate of the instability and under certain conditions may suppress it completely.

The uniform DLE over the whole electrode area was observed with currents of more than  $100\mu A$ . An advantage of PGDS over low pressure gas discharge (i.e., rf or microwave in a pressure range of a few  $mTorr$  to a few Torr) and dielectric barrier discharge (i.e., in a pressure range 500-1500mbar) is the nonthermal behavior at high gas pressures and uniform (i.e., without filamentary) discharge mode. In most cases, it is desirable or even necessary to use nonthermal plasmas, because high gas temperatures can destroy the sample. Therefore, at a constant gap spacing (10-100 $\mu m$ ) and a wide range of the gas pressure (20-700 Torr), even for critical electrical field strength ( $E \cong 4 \times 10^4 V/cm$ ) and current densities ( $j \cong 10^{-4} A/cm^2$ ) values the discharge in a PGDS could be still rather uniform. Filamentation can cause distortion in the GaAs surface, leading to nonuniform processing of the surface. Therefore, the local changes in the surface irregularities of the GaAs plate lead to local changes in the current and the gas DLE. Therefore, nonuniform processing of the GaAs surface are visualized in the form of irregularities in the DLE. In a previous publication [16], we reported fractal dimension analysis as an alternative method to identify inhomogeneities in the semiconductor plate with large-diameter. This paper deals with etching of semiconductor material using a (near)-atmospheric non-thermal plasma source for general surface processing and thereby eliminate the need of costly vacuum systems. Moreover, one can determine surface irregularities in the large diameter semiconductor plates by the fractal dimension method.

## 2. EXPERIMENTAL

A schematic diagram of the experimental set-up and a PGDS equipped with a proximity focused image

intensifier coupled to the charge coupled device (CCD) is shown in fig.1. A Cr-compensated GaAs ( $\rho \sim 10^7 \Omega cm$ ) plate [17] was used as a semiconductor cathode. The diameter and the thickness of the plate were 30mm and 1mm, respectively. On the illuminated side of the GaAs, a transparent conducting vacuum-evaporated Ni-layer was coated. The anode was a disc of glass (of 30mm diameter and 2mm thickness) coated with a thin layer of transparent conductor SnO<sub>2</sub>. The GaAs plates were selected from a number usually employed in a PGDS. Even after grinding and polishing the surface were not subjected to chemical etching: i.e., there was a strongly disturbed surface layer on the GaAs plate.

Gallium arsenide is a direct semiconductor with a band gap of 1.42eV at room temperature. When the radiation is absorbed, electrons are excited and perform transitions from the valence band to the conduction band. This internal photoeffect lowers the resistivity of the material. The light of an incandescent lamp with an Si-filter in front illuminates the cathode uniformly. The discharge can burn on a circular-shaped area with a diameter of 20mm. In the following, this area is often referred to as the active area. The DLE can be observed through the SnO<sub>2</sub> layer and the glass plate (fig.1). To ensure spatial homogeneous illumination, a homogeneous beam was prepared by a simple optical arrangement. The maximum illumination intensity is around  $10^{-4} Wcm^{-2}$ .

The discharge current is measured as the voltage drop at the serial resistor  $R=100\Omega$ . This voltage drop is negligible in comparison with the applied high voltage. Therefore, the voltage at the electrodes of the PGDS is virtually equal to the applied voltage. The spatial distribution of the current density in the active area cannot be measured directly but it is proportional to the light density emitted by the discharge [9,19]. Therefore, measurements of the spatial distribution of DLE give also information about the corresponding behaviour of the current. Moreover, it is necessary to have in mind that the semiconductor plate does not act like a usual load resistor, but like a spatially distributed resistive layer. Due to this fact a spatially inhomogeneous IR light distribution projected on the semiconductor cathode will cause an equivalent modulated spatial resistivity distribution in the semiconductor. In other words, this means that the local resistivity of the semiconductor will have the lowest value where the radiation density has its highest value.

The discharge gap of the cell was filled with ambient air and the measurements were carried out at room temperature. The size of the discharge gap,  $d$  (80 $\mu m$ ) and the residual gas pressure,  $p$  (100 Torr), were chosen to ensure a sufficiently bright DLE [18]. A voltage of up to 2,5kV was applied to the electrodes of the cell. DLE over the whole electrode area was observed with currents of more than  $100\mu A$ .

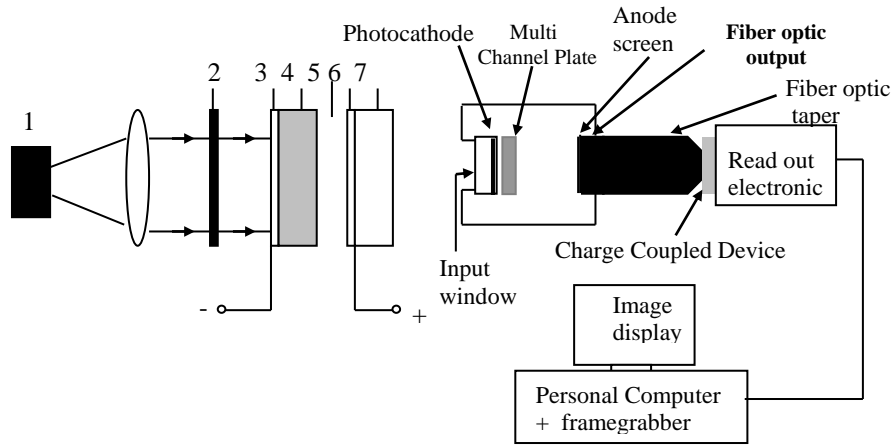


Fig. 1. Experimental setup and a PGDS equipped with a proximity focused image intensifier coupled to the CCD. Numbers indicate: 1-light source; 2-Si filter; 3-transparent Ni-layer; 4-GaAs plate; 5-gas discharge gap; 6-planar transparent  $\text{SnO}_2$  conductor; 7-flat glass disc.

In a PGDS cell the discharge gas does not distort the distribution of the current density in the GaAs plate. The assessment of the image formation was then based on analysis of the DLE (330–460nm), recorded through a transparent anode with spatial resolution via the corresponding light emission [19]. The minimum radiation energy density detected was  $8 \times 10^3 \text{ J/cm}^2$ . Under stationary conditions of image conversion, the spatial resolution of the device, R, was  $\approx 10$  lines per millimetre. With a diameter of the active part of the device of the order of 20mm. The emitted gas DLE is registered by an intensified CCD camera. The computer control and GPIB image transfer are integrated in the software to full automation of the measurement and calculation sequence. After the reference image has been recorded, the camera is focused onto the GaAs surface and a DLE image is recorded.

The two-dimensional (2D) image of a GaAs surface in a PGDS cell are presented in fig. 2a and fig. 2b. As it can be seen in fig.2, the dark regions are distributed on the light background. The dark regions correspond to a low discharge current, and hence to a high resistivity of the GaAs plate. Thus, the resistance inhomogeneities transform to DLE inhomogeneities [20]. If the conductance inhomogeneity is due to fluctuations in the number of the dislocations centers, it is possible to visualize the distribution of the dislocations centers (for more detailed information, see references [11,21]). The surface profilers and fractal analysis were carried out to characterize the surface state of GaAs plate after plasma etching, in order to establish the changes in surface roughness. After the etching process, the GaAs plate is analyzed for the etching depth using a 3-D surface profiler (Zygo, New View 5000).

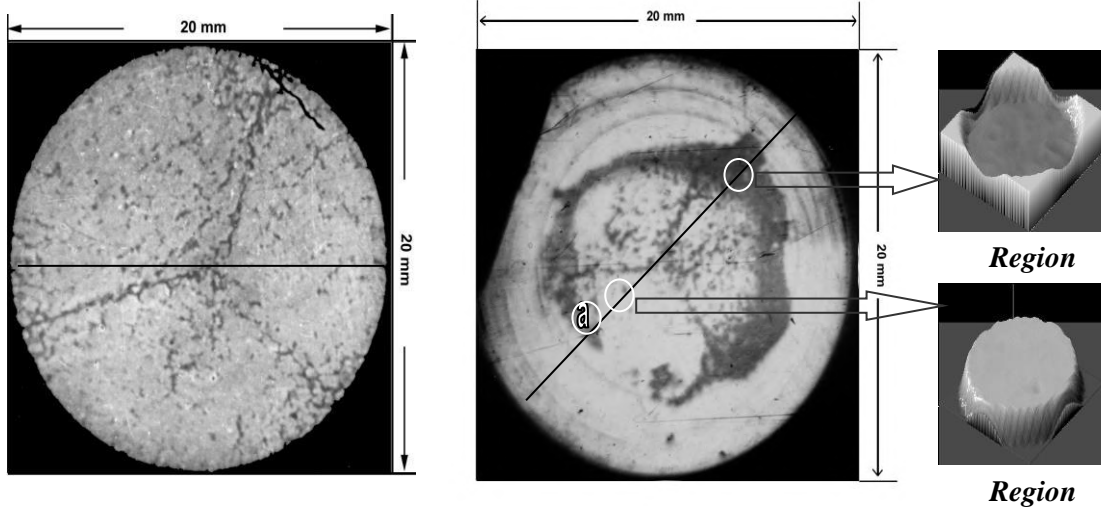


Fig. 2a

Fig. 2b

Fig. 2. The (a) untreated and (b) treated 2D images of the GaAs surface in a PGDS cell. In Fig.2b signs (a), (b) indicates some examples of the plasma etching (i.e. distortion) and (c) smooth surface regions along the profile line, respectively.

A clear graphical representation of the results was obtained by using a discrete set of amplitudes of DLE intensity to smooth out approximating surfaces that passed through all the experimental points. Three-dimensional (3D) charts of the distribution of the DLE intensity or amplitude-coordinate distributions could represent the final results. The possibilities of the visualization have been evaluated, i.e., a local change in surface inhomogeneity is determined by a local change in DLE intensity.

### 3. RESULTS AND DISCUSSION

In semiconductor technology, it is revealed that the surface roughness causes a significant degradation of gate breakdown field strength and channel mobility [18,22,23], since a high surface recombination velocity of non-equilibrium carriers in the semiconductor is ensured in present a PGDS. Studies of the characteristics of such devices showed that they are strongly affected by the quality of the semiconductor electrode. This can be observed in part when uniform illumination of a semiconductor gives rise to a nonuniform pattern of the DLE.

In a PGDS cell a spatially inhomogeneous IR light distribution projected on the surface of the GaAs plate will cause an equivalent modulated spatial resistivity distribution in the GaAs plate. Relating to

different experimental conditions of the same semiconductor, 2D images have been obtained as in fig. 2a. and fig. 2b. While fig. 2a. gives a homogenous spatial appearance owing to the similar lightness, fig. 2b. has light and dark regions compared with fig. 2a. Effects of charge particles bombardment as a reasonable result of plasma-chemical processes are mostly seen as a C - shaped dark area with the surface distortions in fig.2b. Meanwhile some local distortions take place near the center of GaAs plate. Later, these distortions will be proved as the main cause of surface irregularities of the GaAs plate, quantitatively. In fig.2b. signs (a), (b) and (c) indicate some examples of the plasma-chemical etched and smooth regions along the profile line, respectively.

Magnified three-dimensional 3D forms of (b) and (c) regions indicate surface irregularities and smooth parts of the semiconductor material with respect to the DLE intensities. These images will be discussed later. To determine the light and dark regions of 2D images of the semiconductor surface effectively, fig.2a. and fig.2b. have been transformed into 3D form (fig.3a and fig.3b). As seen in fig.3a. and fig.3b, the DLE intensity has been given by a 3D GaAs surface pattern to identify the differences in the intensity values between the 2D images in fig. 2a. and fig. 2b.

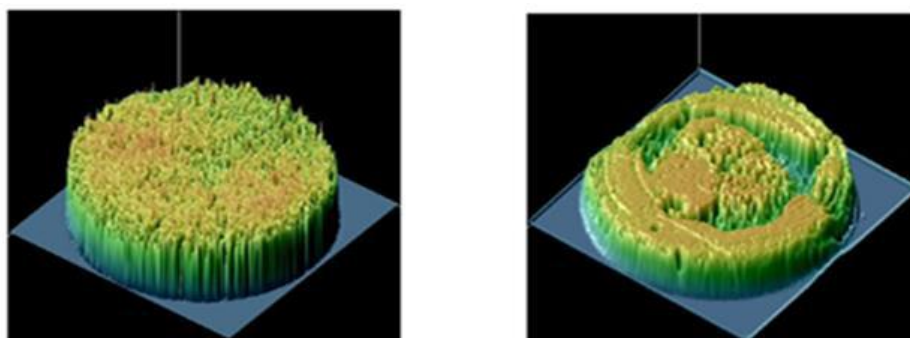


Fig. 3. The (a) untreated and (b) treated 3D surface patterns in a PGDS with a GaAs plate. The plate thickness was 1mm, the diameter was 30mm, the discharge gap width was 80 $\mu$ m, the applied voltage 800V, the air pressure was 100 Torr and the current was 100 $\mu$ A.

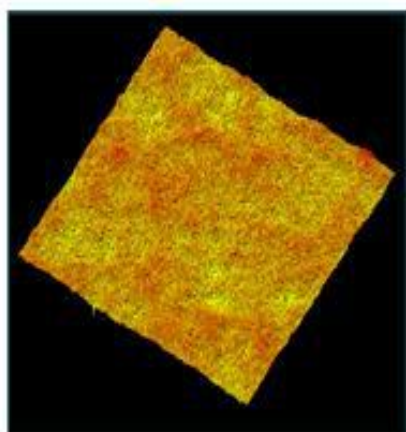


Fig.4a. 3D surface pattern of untreated region in fig.2a on the GaAs plate (2mm x 2mm) in a PGDS.

It is obvious that fig.3a differs from fig.3b in its emission intensity values and gives a homogenous spatial appearance owing to the similar DLE intensity distribution [16]. However, fig.3b. has an inhomogenous structure as a result of the very changeable emission intensity distribution as a qualitative feature. At this point, it is interesting that if fig.3a is compared with the 3D form of the region (c) in fig.2b, the DLE intensities in region (c) is seen to be smoother than that of fig.3a. We consider this event as a positive result of plasmachemical processes. The interaction between the gas mixture and semiconductor can generate smoother surfaces because of etching and desorption of the GaAs surface [24]. The effectiveness of desorption process is proportional to the densities of bombarding particles as well as the stream of desorpted particles leaving the

cathode surface. Meantime, the filamentation in a PGDS during a uniform illumination of the GaAs plate is since a higher conductivity in the cathode plate gives rise to more charging of the GaAs plate which leads to a higher gamma-coefficient on this plate [25,26]. This process in combination with ion bombardment might even explain the reproduction process of filamentation altogether. Filamentation enhances the desorbing of the GaAs surface at the corresponding (a) and (b) regions in fig.2 where the etched regions become deeper as the time progress (see fig.4b and fig.6b).

While increasing total current by illuminating the photosensitive GaAs plate or increasing the supply voltage, the density of the charged carrier in the discharge gap increases. This is accompanied by the formation of the net space charge in the discharge gap, and gradually the transition from the Townsend regime to the glow discharge regime takes place. Therefore, we want to mention that while passing from Townsend regime to the glow discharge space charge become important and the current flow through the gap is not homogeneous but constricted.

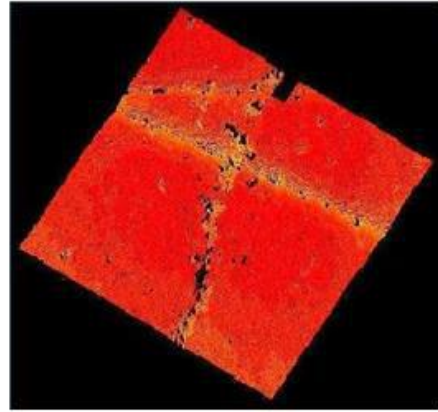


Fig. 4b. 3D smooth surface pattern of the same treated region in fig.4a on the GaAs plate (2mm x2mm) with the etched channels where the discharge current is higher than the critical and the etching depth increases to ~ 242nm. A surface profiler scan is shown in fig.4(c).

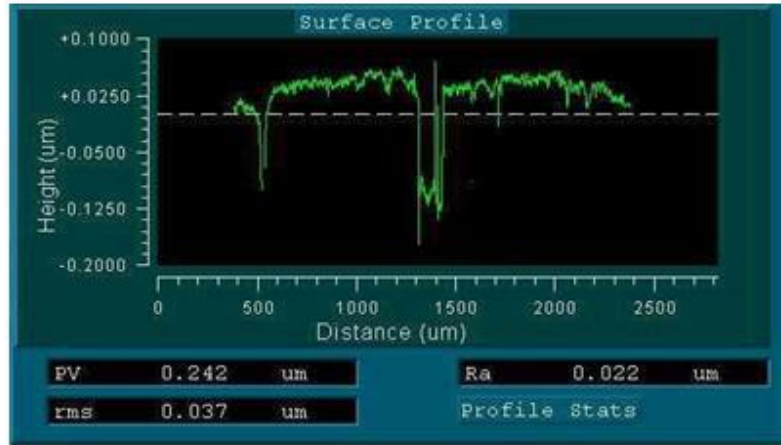


Fig.4(c). Surface profiler scan of etched region in Fig.4b on the GaAs surface caused by a PGDS at the discharge parameters above critical experimental conditions.

The discharge area spreads laterally by increasing the external applied voltage, while the current density stays nearly constant until finally, the discharge covers the whole electrode area. Therefore, due to the previous reason, surface profile reveals etched regions where the system pressure and gap produce a more uniform (without filamentary) discharge, resulting in smooth etched surface (region c in fig.2b); and regions where the discharge current is higher than the critical and the etching depth increases to ~242 nm in the etched channels on the surface (fig.4b). 3-D surface topography of untreated and treated region on the GaAs surface (2mmx2mm) is shown in fig.4a, b. After the etching process, the GaAs plate is analyzed for the etching depth using a 3-D surface profiler. A profiler scan of a typical distorted region caused by PGDS is shown in fig.4c.

Figure 5 shows the variation of the upper limits of current  $I_{\perp}$  values (above which the filamentation starts), for three different illumination intensities of

light ( $L_1 > L_2 > L_3$ ), which lead to three different resistances of GaAs cathode ( $R_1, R_2, R_3$ ). The following process resulting in a local increase in the current then occurs. Modulation of the bulk of the semiconductor cathode and a reduction in its resistance increase the current in the plasma, and also increase the intensity of the light emitted by the gas and the flux of the ionizing particles, which in turn reduce to an even greater degree the resistance of the semiconductor cathode in this range (for detailed information see [27]).

Possible explanations for the distortion include localized heating leading to vaporization, charge built-up, and release on or below the surface due to a small defect within the semiconductor material, or, most likely, due to charging which is thought to be the dominant damage mechanism in photoresist ashing [28,29]. Additionally, it is our observation that for all the pressure and gaps explored in this work the intensity of the filamentation can be adjusted, but in no instance was the discharge a homogeneous glow.

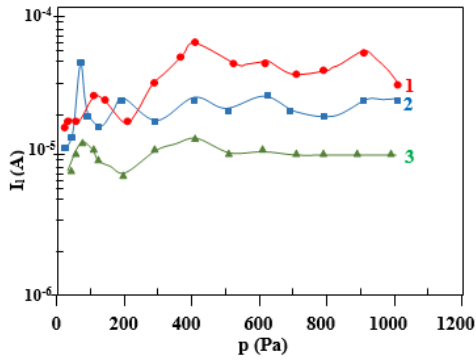


Fig.5. Dependence of the limiting current  $I_l$ , corresponding to the beginning of filamentation on pressure at the length of the discharge gap of  $d = 30\mu\text{m}$ . Curves 1, 2, 3 correspond to three different resistances  $R_1 = 10^7 \Omega$ ,  $R_2 = 6 \times 10^7 \Omega$ ,  $R_3 = 1.3 \times 10^8 \Omega$  of GaAs cathode.

Many earlier studies such as [24,30] utilized this kind of surface treatment technique to obtain convenient materials. In this manner, it will be noted later that fractal analysis method can be also considered as a qualitative analysis tool for earlier studies about this surface treatment technique. In addition to that, it should be also stated that distorted semiconductor regions such as (a) and (b) in fig.2b can be generated above critical experimental conditions (i.e., exposure time, gas pressure,  $p$ , discharge gap,  $d$ , feeding voltage, illumination intensity etc.). For present purposes, in this case, positive effects of plasma-chemical etching disappear and irregularities begin to increase on the whole surface of semiconductor.

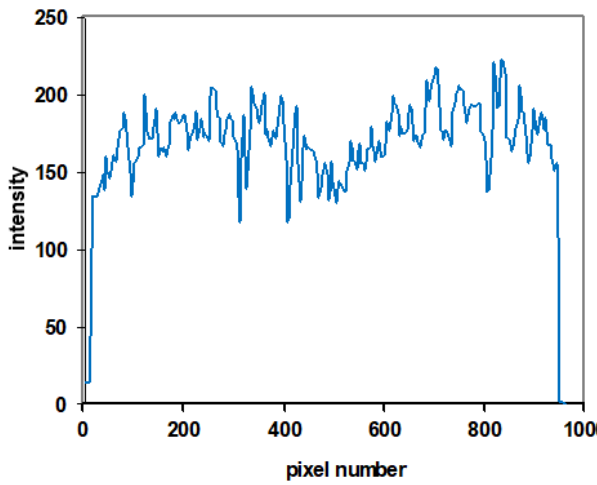


Fig. 6a

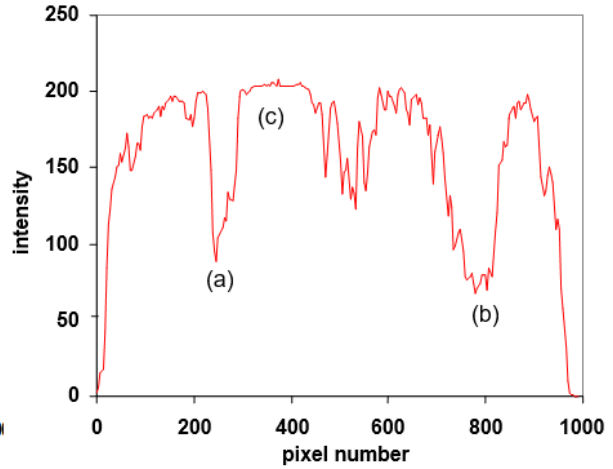


Fig. 6b

Fig. 6a, 6b. Variations of DLE intensities (i.e., gray levels) along the active semiconductor area diameter (20mm) of (a) untreated and (b) treated GaAs surface patterns. In fig.6b signs (a), (b) indicates some examples of the plasma etching regions along the profile line.

Fig. 6a and fig. 6b, which give a transformation of the DLE intensity into profile form in the active semiconductor area diameter as pixel number, clarify the differences between the 3D patterns more efficiently. The irregularities in the outer surface of the semiconductor plate are clearly visible, and these areas are indicated as two broken part grey-colored parts in the profile. The program at the chosen optimum conditions gave a better image quality. With the optimum value of the size of the discharge gap,  $d$  ( $80\mu\text{m}$ ), and the gas pressure,  $p$  (100 Torr), the image contrast of the large semiconductor plates can be improved considerably with a reasonable improvement in the spatial resolution. In order to obtain more information, the images are constructed at various operating voltages for the same parts of the semiconductor plate. It is interesting to know that the all parts of the semiconductor plate are easily identified as a spatial pattern. In the present case, the differences between the maximal and minimal DLE intensity values among the pixels on the diameter of the semiconductor surface patterns are 104 and 180

for fig. 6a and fig. 6b, thereby indicating the untreated and treated surfaces respectively. However, one should eliminate the extreme plasma etched regions (i.e., signed with (a) and (b) in fig.2b), threshold pixel numbers of which are given by 224-294 for region (a), and 704-848 for region (b), to find out the accurate differences between the maximum and minimum DLE intensity values for the determination of positive effects of plasmachemical processes. For this aim, extreme plasma etched regions are indicated by grey-coloured curves in fig.6b. According to the dark curves, which represent the positive effects of etching in the optimal conditions, differences between the maximum and minimum light emission intensity values is found as 81 in the active area of the semiconductor. This result supports the above-mentioned idea that plasma etching improves the quality of a semiconductor surface and homogeneity of DLE, if the experimental conditions are determined appropriately, in the sense that the difference between the maximum and minimum DLE intensity values is

decreased from 104 to 81 for the same semiconductor plate.

A quantitative fractal dimension estimation has been carried out over the active area of DLE intensity to identifying the homogeneity in the spatial patterns given in fig. 3a and fig. 3b. To provide similar terminology between the DLE pattern and the analyze process, it should be stated that the DLE intensity values are referred to as grey levels and the term grid is used for a pixel. In this manner, fractal dimension analysis has been realized by calculating  $L(R)$  for various  $R$  values inside a 960x960 pixel area with a

maximal 256 grey-levels for each pattern (for more detailed information see [16,31]). The fractal dimension of the coastline  $L$  is denoted by dimension  $D$  and can be found from the expression

$$D = -\frac{\log L(R)}{\log R} \quad (1)$$

The value of  $L(R)$  is calculated for each  $R$  ( $R$  is the grids size), and a log-log plot of  $L(R)$  versus  $R$  is obtained. The slope of the least-square linear fit line will give  $-D$ .

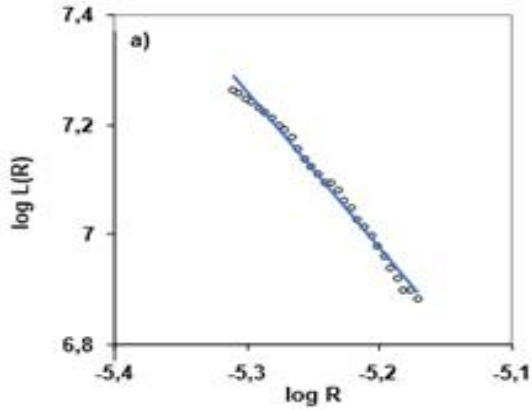


Fig. 7a

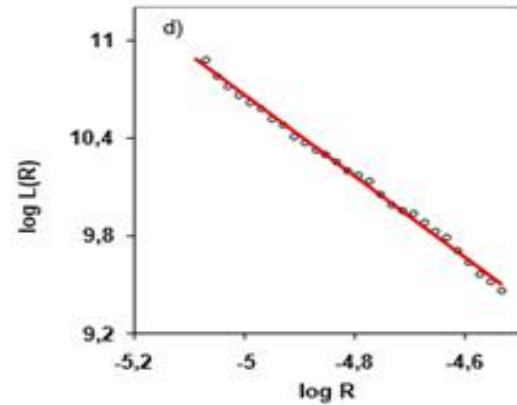


Fig. 7b

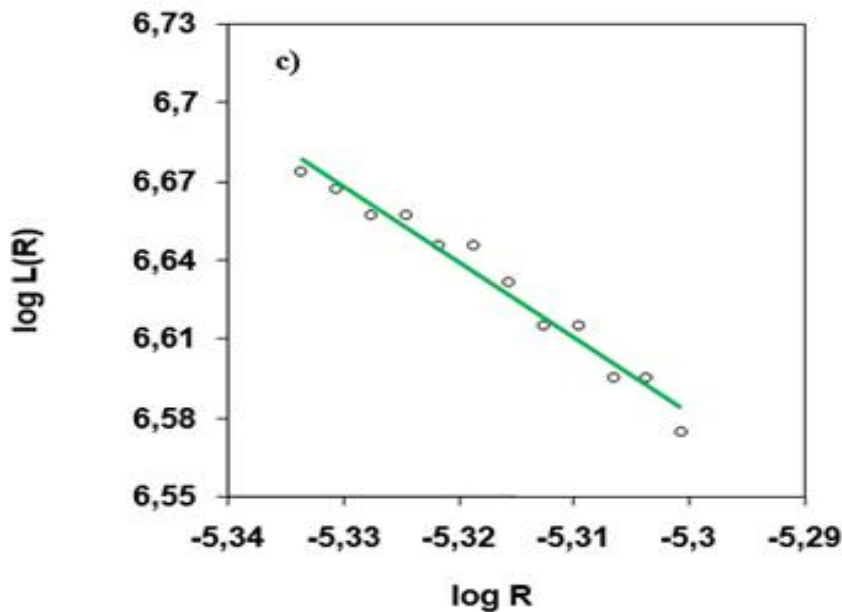


Fig. 7c.

Fig. 7. The log-log plots of the DLE intensities of (a) untreated, (b) treated and (c) smooth GaAs surface patterns with the least square fit lines.

Fig. 7a, b and c present the results of analyses as log-log plots of each pattern with the least- squares linear fit lines. Dimension values have been extracted from the slopes of linear fit lines. According to the slopes in these plots, dimension values have been

found as  $D=2.85$  and  $D=2.52$  for fig. 3a and fig.3b, respectively. These dimension values provide precise knowledge for the homogeneity of the active area of the DLE surface pattern of the semiconductor as mentioned earlier, in the sense that high dimension

values indicate the excess of filled grids relating to their grey levels. Therefore, while the homogeneity rate of the DLE pattern seen in fig.3a is 2.85 (remember that the maximal value of  $D$  is 3), fig.3b gives an inhomogeneous appearance owing to its low  $D$  value. However, if one eliminates the extreme plasma etched regions, spatially in fig.3b, fractal dimension is found as  $D=2.89$  from the log-log plot given in fig.7c. A quantitative fractal dimension estimation thereby confirm that plasma etching improves the quality of a semiconductor surface owing to higher dimension value than the dimension value of the untreated semiconductor. Moreover, the size and location of surface inhomogeneities in large-diameter semiconductor plates may be ascertained by this method. It can be considered that a local change in surface in the treated region is determined by a local change in DLE intensity. An analysis of the DLE pattern can be used to determine the effectiveness of visualization of the surface irregularities as a function of their structure [20]. The observed gas DLE patterns of the semiconductor plate make it possible to assert that the structural disturbance regions are those of accumulation of surface irregularities.

## 5. CONCLUSIONS

From the analyses on experimental findings, we could establish the etching behaviours of plasmachemical processes which result in changes to GaAs surface roughness. This indicates that at appropriate set of experimental parameters (i.e., exposure time, feeding voltage, illumination intensity, discharge gap and gas pressure) the formation of very smooth cathode surface is induced by plasma etching of GaAs plate. Moreover, this very smooth semiconductor surface also enhanced the homogeneity of DLE and consequently the spatial resolution and image contrast in a PGDS could be improved considerably. It has been found while the quality of the GaAs surface in a PGDS can be assessed by the fractal dimension estimation, the effect of plasmachemical processes for optimal and arbitrary experimental parameters are separately determined using fractal concept. The results obtained in this work suggest that a PGDS can be an efficient, alternative plasma source for general surface processing, because they can provide nonthermal discharges also near atmospheric pressures and thereby eliminate the need of costly vacuum systems.

- 
- [1] V. Malhotra, C.W. Wilmsen. In: Holloway PH, McGuire GE, editors. Passivation of GaAs and InP in Handbook of Compound Semiconductors, Noyes Publications: New Jersey, 1995, pp.328-69.
- [2] P.B. Vigneron, F. Joint, N. Isac, R. Colombelli, E. Herth. Microelectronic Engineering. 2018, 202, 42.
- [3] V.R. Agarwal, D.S. Rawal and H.P. Vyas. J. Electrochem. 2005, Soc., 152, 567.
- [4] Y.W. Chen, B.S. Doi, G.I. Ng, K. Radhakrishnan and C.L. Tan. J. Vac. Sci. Technol., 2000, B, 18, 2509.
- [5] M.A. Liebermann and A.J. Lichtenberg. Principles of Plasma Discharges and Materials Processing., 1994, Wiley, New York.
- [6] J. Rutkowski, W. Fourcault, F. Bertrand, U. Rossini, S. Gétin, S. Le Calvez, T. Jager, E. Herth, C. Gorecki, M. Le Prado, J.M. Léger, S. Morales. Sensors Actuators A Phys., 2014, 216, 386.
- [7] R. Schwarz and J.G. Salge. in Proceedings of the 11th International Symposium on Plasma Chemistry, edited by J. Harry., Loughborough, Le-icestershire, England, 1993.
- [8] M. Karlsson, F. Nikolajeff. 2002, Appl. Opt. 41, 902, 1539.
- [9] H. Willebrand, Y.A. Astrov, L. Portsel, S. Teperick, T. Gauselmann. Infrared Phys. & Technol., 1995, 36 (4), 809.
- [10] B.G. Salamov, A.Kh. Zeinally, N.N. Lebedeva and L.G. Paritskii., 1991, J. Photogr. Sci., 39, 114.
- [11] Y. Sadiq, K. Aktas, S. Acar and B.G. Salamov. Superlattices Microstruct., 2010, 47, 648.
- [12] F. Hasegawa, M. Onomura, C. Mogi and Y. Nannichi., Solid-State Electron, 1988, 31, 223
- [13] Ch. Radehaus, T. Dirksmeyer, H. Willebrand and H-G. Purwins. Phys. Lett. 1987, A 125 92
- [14] H.Willebrand, T. Hünteler, F. Niedernostheide, R. Dohmen and H-G. Purwins. Phys.Rev. 1992, A 45 8766
- [15] S. Ozturk Koç, S. Galioglu, B. Akata, E. Koç, B.G. Salamov. J. Electronic Materials., 2018, 47, (5), 2791.
- [16] H. (Yücel) Kurt, E. Kurt, B.G. Salamov. Imaging. Sci. J., 2001, 49, 205.
- [17] K. Germanova, V. Donchev, Ch. Chardalov and L. Nikolov. J.Phys.D, 1987, 20, 1507.
- [18] K. Koseoglu, B.G. Salamov. Plasma Process. Polym. 2016, 13, №3, 355.
- [19] K. Koseoglu, M. Özer, B.G. Salamov. IEEE Transactions on Plasma Science., 2015, 43, №10, 3576.
- [20] L.V. Belyakov, A.B. Mageramov and L.G. Paritskii. Sov. Phys. Semicond., 1978, 12, 6, 739.
- [21] K. Aktas, S. Acar, B.G. Salamov. Plasma Sources Sci. Technol. 2011, 20, 045010.
- [22] T. Ohmi, M. Miyashita and T. Imaoka. Proceeding of the Microcontamination Meeting, Canon Communications, San Jose, CA, 1991, pp.491.
- [23] M. Heyns, C. Hasenack, R. De Keersmaecker and R. Falster, J. Ruzyllo and R.E. Novak (eds.). Proc. of the 1<sup>st</sup> Int. Symp. on Cleaning

- Technology in Semiconductor Device Manufacturing, PV 90-9, Electrochemical Society, Pennington, NJ, 1990, p.293.
- [24] *S.W. Robey*. Phys. Rev. 2002, B, 65, 115
- [25] *Z. Falkenstein and J. Cogan*. J. Appl. Phys., 1997, 82 (12), 6273.
- [26] *G. Xu, L. Li, N. Isac, Y. Halioua, A. Giles Davies, E.H. Linfield, R. Colombelli*. Appl. Phys. Lett., 2014,104, 091112.
- [27] *Y. Sadiq, M. Ozer, B.G. Salamov*. J. Phys. D: Appl. Phys. 2008, 41, 045204.
- [28] *Ma S. and McVittie J.P.* J. Vac. Sci. Technol., 1996, B, 14, 566.
- [29] *S. Fang and McVittie J.P.* IEEE Trans. Electron Devices, 1994, 41, 1034.
- [30] *Z. Synowiec*. Vacuum, 2001, 63, 487.
- [31] *Li X W, J.F. Tian, Y. Kang and Z.G. Wang*. Scripta Metall. & Mater., 1995,33,5, 803.

*Received:12.09.2022*

## MEASUREMENT OF INTERNAL AND SURFACE TEMPERATURES AND OPTICAL PROPERTIES OF ZERDINE PHANTOM UNDER 635 NM LOW LEVEL LASER IRRADIATION

HÜSEYİN OKAN DURMUŞ<sup>1,2</sup>, MIRHASAN Yu. SEYIDOV<sup>1</sup>

<sup>1</sup>*Department of Physics, Gebze Technical University, 41400, Kocaeli, Turkey*

<sup>2</sup>*Medical Metrology Laboratory, TUBITAK National Metrology Institute (TUBITAK UME), 41470, Kocaeli, Turkey*

*E-mail: hokandurmus@gtu.edu.tr, smirhasan@gtu.edu.tr;*

*Tel: (262) 605 10 00; Fax: (262) 653 84 90*

In this study, internal and surface temperatures of the Zerdine phantom used as reference material in the ultrasonic imaging processes and its optical properties such as absorbance, transmittance, reflectance, refractive index, and optical attenuation coefficient were investigated by using a low-level laser device which has a 635 nm wavelength. Internal temperatures and the said optical properties were measured successfully. However, due to the transparent color nature of the Zerdine phantom, significant temperature increases could not be detected at the surface of the phantom. Therefore, the phantom material was colored at different concentrations with a color tone close to human skin, and thus surface temperatures were measured in this way. However, it was determined that surface temperature values did not increase too much with increasing color concentration. Therefore, it has been concluded that the use of Zerdine phantom as an ideal background reference material in optical imaging studies makes it advantageous because of its transparent color nature and low optical absorbance value.

**Keywords** Low-Level Laser, Zerdine Phantom, Internal and Surface Temperature Measurements, Optical Properties.

### INTRODUCTION

Today, lasers are used extensively in all areas of life. However, medical lasers are one of the most effective, intensive and widely used devices. The use of lasers in diagnostic and therapeutic applications varies according to the place of use. Therefore, laser researchers have developed different lasers for different medical needs in medical operations and treatments. Dermatology, ophthalmology, dentistry, otolaryngology, gastroenterology, urology, gynaecology, cardiology, neurosurgery and orthopaedics can be given the examples of areas where lasers are used. In addition, there is also every day of new developments in laser-based techniques. In particular, the role of light-based technologies in dermatology has increased dramatically in recent years. Therefore, laser or light-based therapy devices for the treatment of dermatological diseases are constantly being introduced [1-6].

The use of low-level lasers has gained popularity in the medical sciences over the last 30 years [7]. Low Level Laser Therapy (LLLT, or sometimes also called as Low Level Light Therapy or Photobiomodulation (PBM)) is a low intensity light therapy. Usually low power laser (typically in the power range of 10 mW-500 mW) or LED light is applied to the skin in this therapy. For a long time, low-level laser therapy (LLLT) or LED (light emitting diode) photobiomodulation has been shown to reduce inflammation and edema, induce analgesia (relieve pain), and promote healing musculoskeletal pathologies and injured tissues [8-9]. In clinical practice, the effect of temperature on tissue is the most common category of laser-tissue interaction, as well as photo-chemical and photo-mechanical effect [10].

Tissue-mimicking materials (TMMs) or tissue phantoms are widely used in the biomedical research

area especially at thermo-acoustical [11-14] and optical research [15-18] as a test model.

The definition of the phantom is made as “any apparatus or material that mimics the operation or physical properties of human systems or tissues”. Although it is possible to use real tissues directly in experiments, this is not a logical method. Instead, working with artificial materials that simulate the physical properties (such as acoustical, optical, mechanical and thermal, etc.) of human tissues provides many benefits. Therefore, phantoms enable systematic testing and controlled optimization of new measurement methodologies before being tested on living things such as animals or humans. The use of phantoms enables simulation for systems at different complexity levels or human tissues. The use of phantoms in initial tests instead of biological materials provides an effective alternative to medical research. Therefore, after the initial results on phantoms are positive, real tissues can be used. After this stage, animal experiments (laboratory mice in general) are usually performed, and then the tests are performed on humans [19].

In the optical field, phantoms are used in various forms such as the development of imaging techniques and image-guided interventions, system validation, optimization, stability assessment, medical device calibration, verification, and clinical training [20-22].

In this study, internal and surface temperatures caused by 635 nm low level red color laser irradiation on Zerdine phantom were measured and optical properties of the phantom were determined. With this study carried out, the temperature effects of a low level laser device on a tissue-phantom and thus the safety usage of the laser will be investigated. Therefore, this investigation will provide an innovative contribution to the scientific literature in terms of safety evaluation.

The organization of the paper will be as follows. In the second part, information about phantom material, the laser used, thermal camera and surface temperature measurements, optical power meter, thermal sensor and optical power measurements, single integrating sphere and measurement and calculation of optical properties will be given. In the third part, internal temperature measurements, surface temperature measurements, and optical power measurements results will be shared. In the final section, the studies made and the results obtained will be summarized and some suggestions will be given.

## METHODOLOGY

In this study, the colored and transparent Zerdine phantom, laser device, T-type of thermocouples, single integrating sphere, optical power meter and its thermal sensor and infrared/thermal camera were used. All experiments were performed under controlled laboratory ambient conditions.

## PREPARATION OF ZERDINE PHANTOM

The Zerdine phantom was produced according to the formula of Zerhouni and Rachedine. The colored phantom samples were prepared from the stock solution prepared with brown, yellow and pink water-based dyes in the amount of 0.375 ml (2.5%), 0.75 ml (5%), 1.5 ml (10%), 3 ml (%20) by putting together with Zerdine phantom within 15 ml containers. A picture of different colored Zerdine phantoms can be seen in Figure 1.

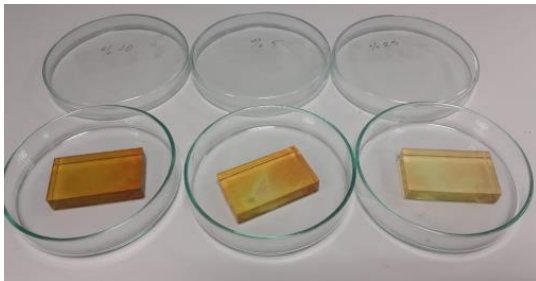


Fig. 1. A picture of the colored Zerdine phantoms.

## THE LASER USED

Optotronics brand VA-I-400-635 model 635 nm wavelength red color solid-state diode laser was used for the measurements as an optical source. Maximum working power of the laser was 400 mW.

## TERMOCOUPLE POSITION WITHIN PHANTOM AND INTERNAL TEMPERATURE MEASUREMENT

For internal temperature measurements, Physitemp T-type ultra-fine termocouples were loacted at 15 mm inside from the phantom surface. The distance between the thermocouples was designed to be as 2 mm apart. For multi-channel temperature measurements within the phantom, a PC-based Data

Acquisition and Monitoring Interface system was used. Internal temperature measurement set-up can be seen in Figure 2.



Fig. 2. Internal temperature measurement set-up.

## THERMAL CAMERA AND SURFACE TEMPERATURE MEASUREMENT

Optris PI infrared/thermal camera as shown in Figure 3 and its PC software were used for surface temperature measurements. The declared uncertainty budget for the infrared camera was  $\pm 2^\circ\text{C}$  as stated in the product catalog.

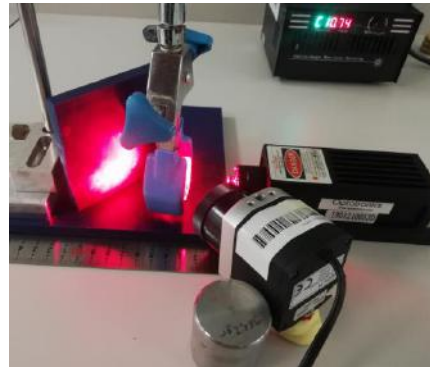


Fig. 3. A picture of pure Zerdine phantom temperature measurement set-up with infrared/thermal camera.

A picture of temperature measurement set-up with infrared/thermal camera for the deliberately colored Zerdine phantom can be seen in Figure 4.



Fig. 4. A picture of temperature measurement set-up with infrared/thermal camera for the deliberately colored Zerdine phantom.

**OPTICAL POWER METER, THERMAL SENSOR AND OPTICAL POWER MEASUREMENT**

Ophir brand StarBright model optical power meter and Ophir brand 3A type thermal sensor were used for optical power measurements. Figure 5 shows optical power meter, thermal sensor and picture of optical power measurements. Optical Power Measurement set-up can be seen in the Figure 5.

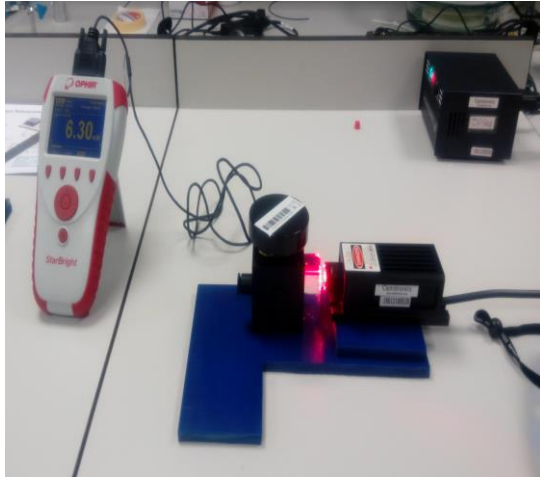


Fig. 5. Optical Power Measurement Set-up.

**SINGLE INTEGRATING SPHERE AND MEASUREMENTS OF OPTICAL PROPERTIES**

Thorlabs IS200 model 2” integrating sphere was used in the measurement of optical properties such as

absorbance, transmittance, reflectance, refractive index and optical attenuation coefficient.

**CALCULATION OF OPTICAL PROPERTIES**

Optical properties such as absorbance, transmittance, reflectance, the refractive index, and optical attenuation coefficient were calculated by using the following formulas.

$$R+T+A = 1 \text{ or } \%R+\%T+\%A = \%100 \quad [23] (1)$$

Absorbance,  
 $A; A=-\log(I/I_0)=-\log(T)=2-\log(\%T) \quad [24] (2)$

Transmittance, T;  $T = I/I_0 \quad [24] (3)$

Reflectance, R;  $R=1-(A+T) \quad [23] (4)$

$$\text{Reflectance, } R = \frac{(n-1)^2}{(n+1)^2} \quad [23] (5)$$

where n is the Refractive Index.

$$I = I_0 e^{-\mu x}, \mu = -\frac{\ln \frac{I}{I_0}}{x} \quad [25] (6)$$

Where  $\mu$  is the Linear Attenuation Coefficient.

**RESULTS AND DISCUSSION  
INTERNAL TEMPERATURE MEASUREMENTS**

Internal temperature measurements were carried out for 60 seconds duration at each step by increasing the laser distance by 5 mm from the phantom surface between 5 mm and 25 mm. The internal temperatures measured can be seen below from Figures 6 up to 10.

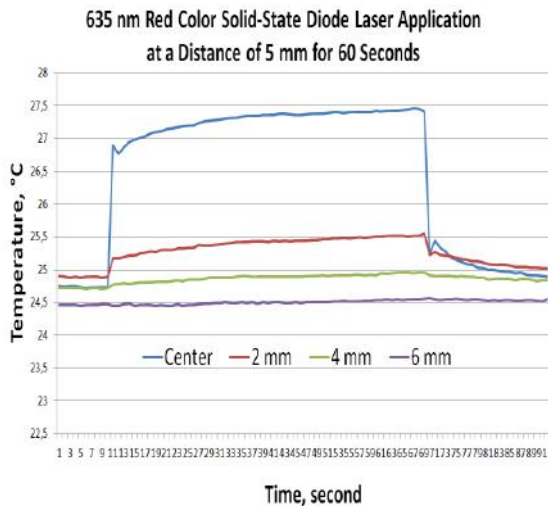


Fig. 6. The internal temperature measurements at a distance of 5 mm for laser irradiation applied for one minute.

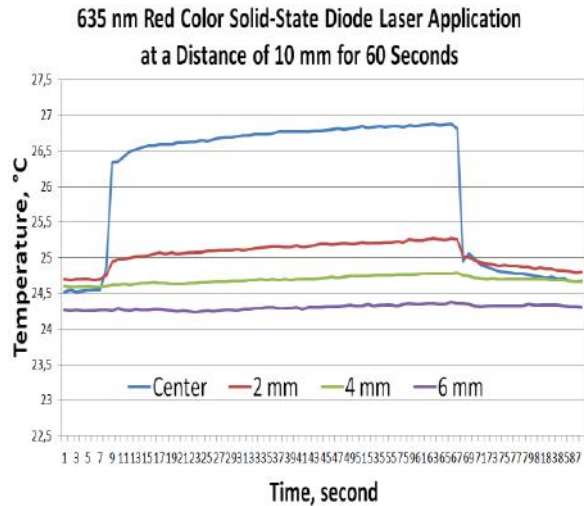


Fig. 7. The internal temperature measurements at a distance of 10 mm for laser irradiation applied for one minute.

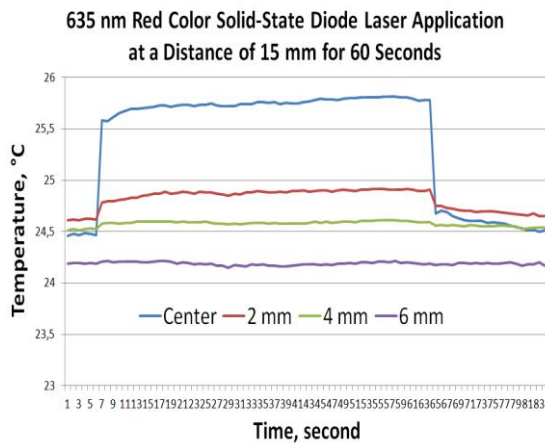


Fig. 8. The internal temperature measurements at a distance of 15 mm for laser irradiation applied for one minute.

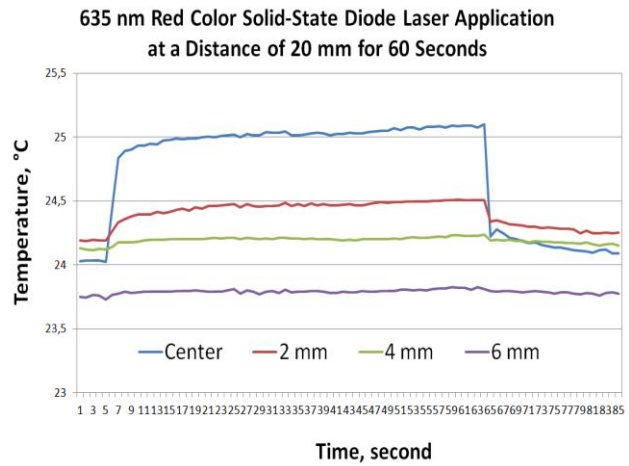


Fig. 9. The internal temperature measurements at a distance of 20 mm for laser irradiation applied for one minute.

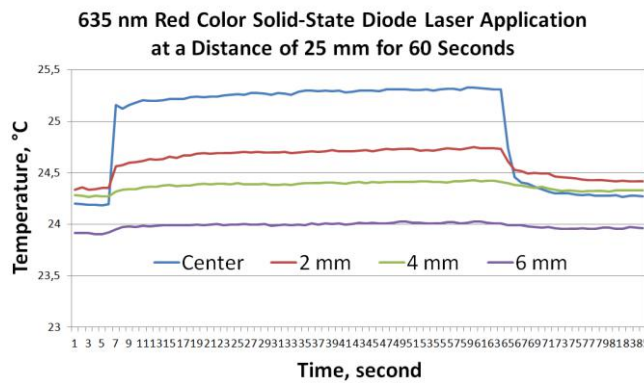


Fig. 10. The internal temperature measurements at a distance of 25 mm for laser irradiation applied for one minute.

The minimum and maximum temperatures, and temperature differences measured at different thermocouple locations within the phantom can be seen from Figure 11 to Figure 15.

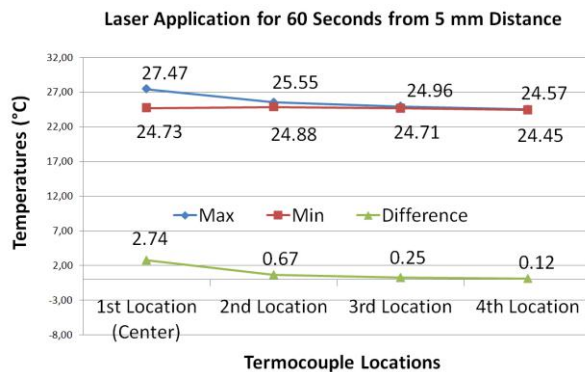


Fig. 11. Maximum and minimum temperatures, and temperature differences at different thermocouple locations caused by a distance of 5 mm.

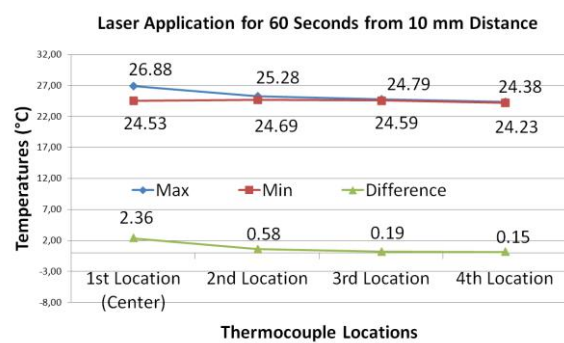


Fig. 12. Maximum and minimum temperatures, and temperature differences at different thermocouple locations caused by a distance of 10 mm

**MEASUREMENT OF INTERNAL AND SURFACE TEMPERATURES AND OPTICAL PROPERTIES OF ZERDINE....**

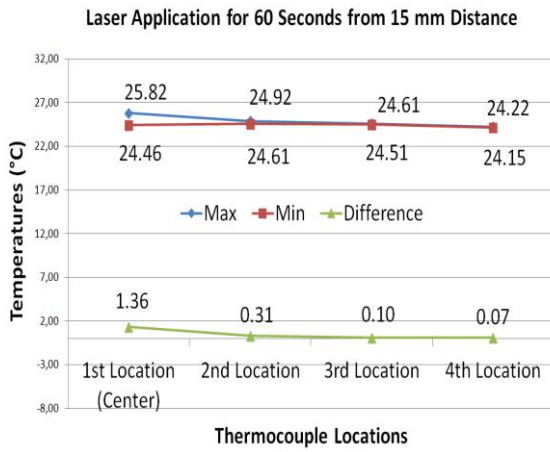


Fig. 13. Maximum and minimum temperatures, and temperature differences at different thermocouple locations caused by a distance of 15 mm.

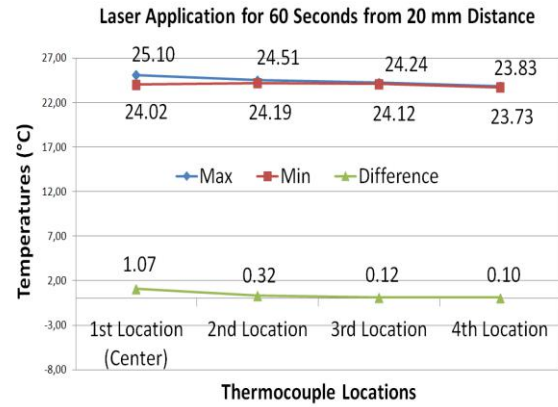


Fig. 14. Maximum and minimum temperatures, and temperature differences at different thermocouple locations caused by a distance of 20 mm.

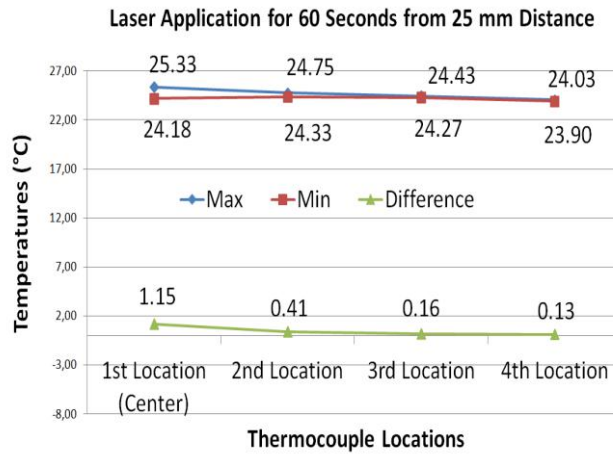


Fig. 15. Maximum and minimum temperatures, and temperature differences at different thermocouple locations caused by a distance of 25 mm.

By using above results, we can reorganize and evaluate the temperature differences in a good manner as per thermocouples used within the phantom. The temperature differences measured by the thermocouples according to the distance of the laser beam from the phantom surface can be seen from Figure 16 to Figure 19.

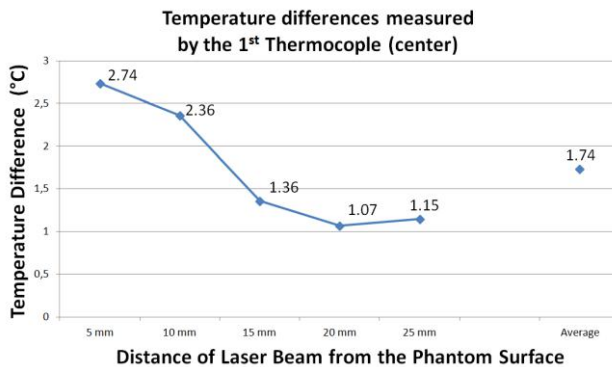


Fig. 16. The temperature differences measured by the 1<sup>st</sup> thermocouple (center thermocouple) within the phantom

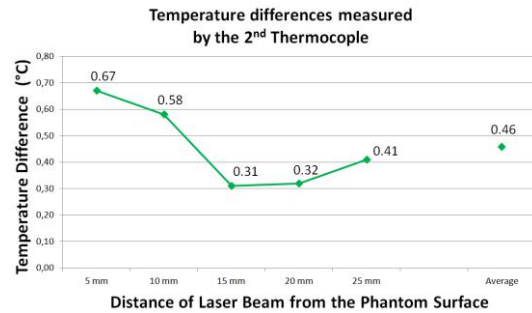


Fig. 17. The temperature differences measured by the 2<sup>nd</sup> thermocouple within the phantom

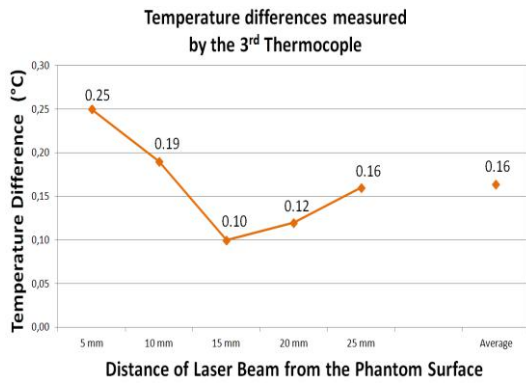


Fig. 18. The temperature differences measured by the 3<sup>rd</sup> thermocouple within the phantom.

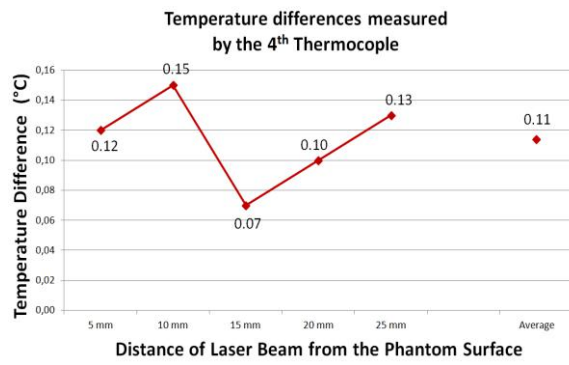


Fig. 19. The temperature differences measured by the 4<sup>th</sup> thermocouple within the phantom.

## SURFACE TEMPERATURE MEASUREMENTS

Because of the transparent color of the Zerdine phantom, significant temperature rises at surface temperatures could not be detected. Thus, the phantom material was colored at different concentrations as 2.5%, 5%, 10% and 20% with a color tone close to human skin (near to red skin) and the temperature differences formed at the phantom surface were measured within one minute interval at different distances with the laser “on” and “off” position. The measurement results can be seen from Figure 20 up to Figure 24.

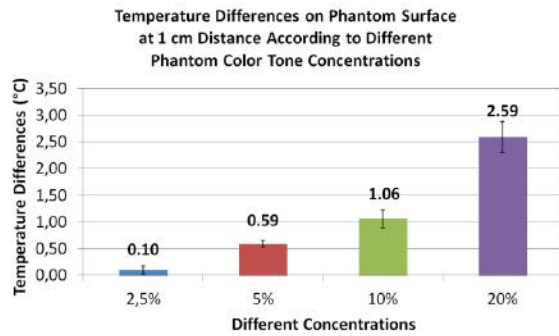


Fig. 20. The measured average temperature differences on phantom surface at 1 cm distance as per different color tone concentrations

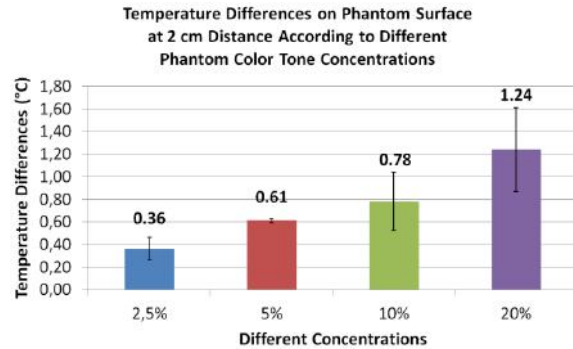


Fig. 21. The measured average temperature differences on phantom surface at 2 cm distance as per different color tone concentrations

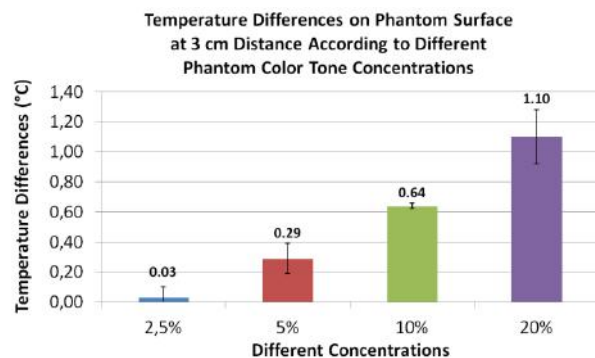


Fig. 22. The measured average temperature differences on phantom surface at 3 cm distance as per different color tone concentrations.

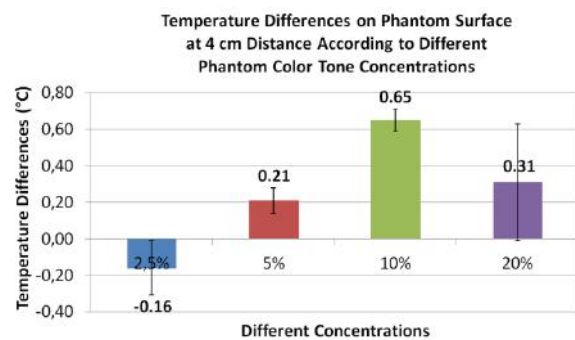


Fig. 23. The measured average temperature differences on phantom surface at 4 cm distance as per different color tone concentrations.

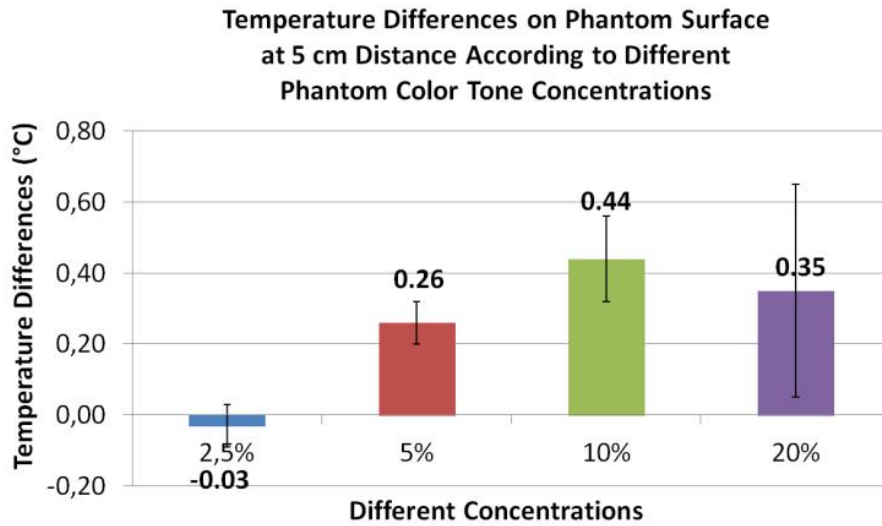


Fig. 24. The measured average temperature differences on phantom surface at 5 cm distance as per different color tone concentrations.

MEASUREMENTS OF OPTICAL PROPERTIES

The measurement of optical properties at 635 nm was performed using the single integrating sphere set-up. The measured values of optical properties of the Zerdine phantom at 635 nm can be seen in Figure 25 and Table I. As seen from the figure that transmittance value of the Zerdine phantom is high. This means that Zerdine phantom behaves like a glass. Because most of the light rays pass through of it.

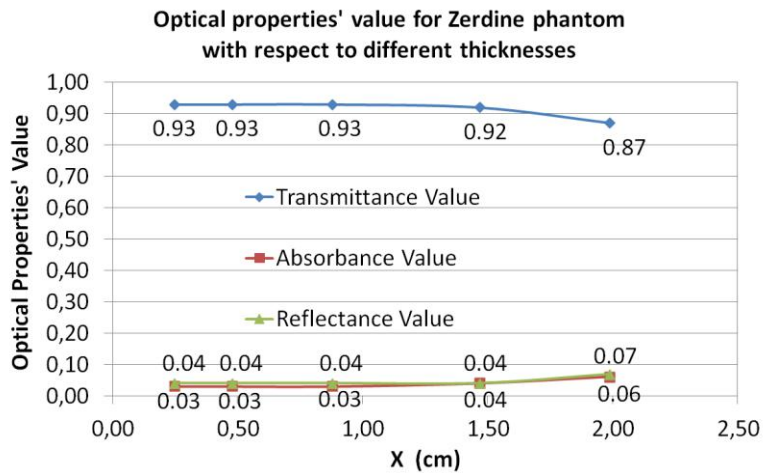


Fig. 25. The measured values of optical properties of the Zerdine phantom.

Table I.

The measured optical properties of the Zerdine phantom at 635 nm as average

Phantom	Transmittance, T	Absorbance, A	Reflectance, R	Attenuation Coefficient (cm <sup>-1</sup> )
Zerdine	0,91 ± 0,03	0,04 ± 0,01	0,05 ± 0,01	0,028 ± 0,01

The attenuation coefficient for Zerdine phantom at 635 nm was found as 0,028 cm<sup>-1</sup> as can be seen in Table I and Figure 26.

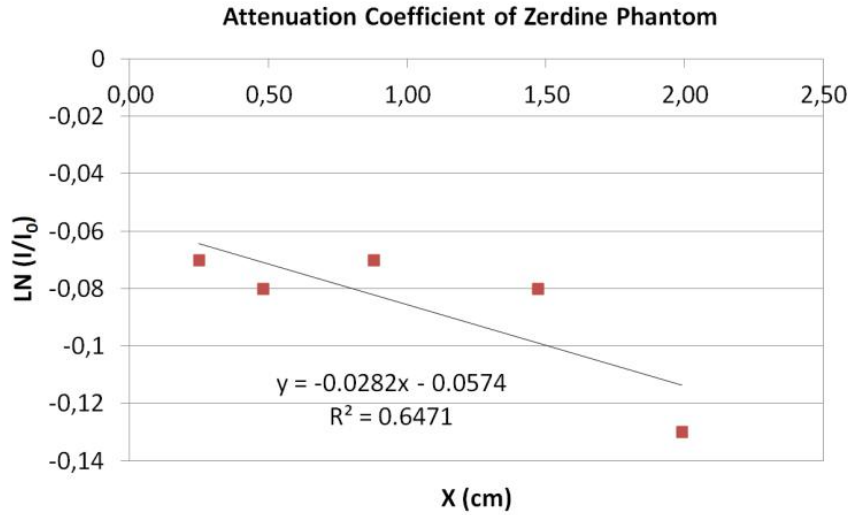


Fig. 26. The attenuation coefficient drawing graph for Zerdine phantom.

Using the formula (5), we also calculated the refractive index at 635 nm and we found the refractive index as  $1.58 \pm 0.08$ . This value also explains and proves the glass-like nature of the Zerdine phantom. Because the range of refractive indices of the glass has a value between 1.4 and 1.7 [26].

## CONCLUSION

In this study, it was firstly tried to be investigated the internal temperature values on Zerdine phantom under 635 nm low level laser irradiation. Later, surface temperatures of deliberately colored Zerdine phantom were measured. Finally, the optical properties of colorless Zerdine phantom were determined.

As a result, this research study can be summarized as follows.

- This study has shown that low-level laser irradiation can be used together with phantom studies. Therefore, phantom studies can be used for optical and temperature characterization of low level lasers.
- Low level laser irradiation produced insignificant temperature increases (max. about 3 °C) within the phantom and phantom surface.

- Low level laser irradiation was found as a safe application on human use for 1 minute interval at a distance of min 0.5 cm in our investigation. Other studies should also be carried out with long periods.

- The Zerdine phantom's optical properties such as absorbance, transmittance, reflectance, the refractive index, and optical attenuation coefficient at 635 nm were investigated for the first time in our knowledge.

- These studies may be evaluated as a tool in the development of wavelength sensitive optical phantom in the future.

- It is also very logical and advantageous to use the Zerdine phantom in terms of optical properties as an ideal background reference material in optical imaging studies because of its transparent color nature and low optical absorbance value.

As a result of this study, we can say that low-level laser therapy sources can be examined by using phantom studies. Furthermore, this study can also be extended towards different kinds of phantoms, the optical properties of the phantoms can be determined in this way and much more similar research studies can be done in the future.

- [1] M.A. Ansari ve E. Mohajerani. «Mechanisms of Laser-Tissue Interaction: I. Optical Properties of Tissue,» Journal of Lasers in Medical Sciences, cilt 2, no. 3, pp. 119-125, Summer 2011.
- [2] Q. Peng, A. Juzeniene, J. Chen, L.O. Svaasand, T. Warloe, K.E. Giercksky, J. Moan. 2008. Lasers in medicine. Reports on Progress in Physics, 71(5), 056701.
- [3] L.O. Svaasand. «Laser-tissue interaction,» Proc. SPIE 1524, Bioptics: Optics in Biomedicine and Environmental Sciences, pp. 1-13, 1992.
- [4] B. Dinç ve M.E. Or. «Farklı Tipte Lazerlerin Veteriner Hekimlikte Kullanımı,» TÜBAV Bilim, cilt 7, no. 3, pp. 1-10, 2014.
- [5] Z. Husain ve T. S. Alster. «The role of lasers and intense pulsed light technology in dermatology,» Clinical, Cosmetic and Investigational Dermatology, no. 9, pp. 29-40, 2016.
- [6] K.J. Ahn, B.J. Kim ve S.B. Cho. «Tissue-Mimicking Phantom Useful in Simulating Laser Light Tissue Interactions» Medical Lasers, cilt 4, no. 2, pp. 86-88, 2015.
- [7] Y. Alipanah, M. Asnaashari ve F. Anbari. «The effect of low level laser (GaAlAs) therapy on the post-surgical healing of full thickness wounds in rabbits,» Medical Laser Application, no. 26, pp. 133-138, 2011.

- [8] *H.B. Cotler, R.T. Chow, M.R. Hamblin, J. Carroll.* 2015. The use of low level laser therapy (LLLT) for musculoskeletal pain. *MOJ orthopedics & rheumatology*, 2(5).
- [9] *G.K. Reddy, L. Stehno-Bittel, C.S.Enwemeka.* 1998. Laser photostimulation of collagen production in healing rabbit Achilles tendons. *Lasers in Surgery and Medicine: The Official Journal of the American Society for Laser Medicine and Surgery*, 22(5), 281-287.
- [10] *A.L. McKenzie.* «Physics of thermal processes in laser-tissue interaction,» *Phys. Med. Biol.*, cilt 35, no. 9, pp. 1175-1209, 1990.
- [11] *B. Karaböce.* 2015, May. Focused ultrasound temperature effect in tissue-mimicking material and sheep liver. In 2015 IEEE International Symposium on Medical Measurements and Applications (MeMeA) Proceedings (pp. 131-134). IEEE.
- [12] *B. Karaböce, H.O. Durmuş.* 2015. Visual investigation of heating effect in liver and lung induced by a HIFU transducer. *Physics Procedia*, 70, 1225-1228.
- [13] *B. Karaböce, E. Çetin, H.O. Durmuş.* 2016, May. Investigation of temperature rise in tissue—Mimicking material induced by a HIFU transducer. In 2016 IEEE International Symposium on Medical Measurements and Applications (MeMeA) (pp. 1-6). IEEE.
- [14] *B. Karaböce, E.Çetin, H.O. Durmuş, M. Özdingiş, H. Öztürk, K. Mahmat, M. A. Güler.* 2018, June. Investigation of Different TMMs in High Intensity Focused Ultrasound Applications. In 2018 IEEE International Symposium on Medical Measurements and Applications (MeMeA) (pp. 1-5). IEEE.
- [15] *B.W. Pogue, M.S. Patterson.* 2006. Review of tissue simulating phantoms for optical spectroscopy, imaging and dosimetry. *Journal of biomedical optics*, 11(4), 041102.
- [16] *İ. Akkaya, M. Engin, Y. Öztürk.* Doku Fantom Üretimi ve Temel Optik Özelliklerinin Ölçümü/Fabrication of Tissue Phantom and Measurement of The Fundamental Optical Properties. *Celal Bayar Üniversitesi Fen Bilimleri Dergisi*, 13(1), 2017, 205-209.
- [17] *J. ZHANG, L.I.U. Yuanjie, J.ROBIC, A. NKENGNE, Y.A.N. Hong, X. ZHANG, SOO, X.Y.* 2019. Optical Phantom Development for Skin Measurement. In 19th International Congress of Metrology (CIM2019) (p. 19001). EDP Sciences.
- [18] *R. Srinivasan, D. Kumar, M. Singh.* 2002. Optical tissue-equivalent phantoms for medical imaging. *Trends Biomater. Artif. Organs*, 15(2), 42-47.
- [19] *R.A. Jaime, , Basto, R. L., Lamien, B., Orlande, H. R., Eibner, S., & O. Fudym,* (2013). Fabrication methods of phantoms simulating optical and thermal properties. *Procedia Engineering*, 59, 30-36.
- [20] *A.I. Chen, M.L. Balter, M.I. Chen, D. Gross, S.K. Alam, T.J. Maguire, M.L. Yarmush.* 2016. Multilayered tissue mimicking skin and vessel phantoms with tunable mechanical, optical, and acoustic properties. *Medical Physics*, 43 (6), 3117-3131.
- [21] *P. Lai, X. Xu, L.V. Wang.* 2014. Dependence of optical scattering from Intralipid in gelatin-gel based tissue-mimicking phantoms on mixing temperature and time. *Journal of biomedical optics*, 19(3), 035002.
- [22] *E. Dong, Z. Zhao, M. Wang, Y. Xie, S. Li, P. Shao, R.X. Xu.* 2015. Three-dimensional fuse deposition modeling of tissue-simulating phantom for biomedical optical imaging. *Journal of biomedical optics*, 20(12), 121311.
- [23] *M.Y. Nadeem, W. Ahmed.* 2000. Optical properties of ZnS thin films. *Turkish Journal of Physics*, 24(5), 651-659.
- [24] *D.T. Harvey.* 2003. *Analytical Chemistry for Technicians*, 3rd Edition, page 193, (John Kenkel).
- [25] *S. Chang, A.K. Bowden.* 2019. Review of methods and applications of attenuation coefficient measurements with optical coherence tomography. *Journal of biomedical optics*, 24(9), 090901.
- [26] *J. Fraser, R. Williams.* 2009. Page 192, *Handbook of Forensic Science*.

*Received: 05.09.2022*

## INVESTIGATION OF PARAMETERS OF SILICON PHOTOMULTIPLIERS

A. MAMMADLI<sup>1</sup>, B. IBRAHIMOV<sup>3</sup>, Y. BACHERIKOV<sup>2</sup>, Z. AHMADOV<sup>1</sup>

<sup>1</sup>*Institute of Radiation Problems, Baku, Azerbaijan*

<sup>2</sup>*V.Lashkaryov Institute of Semiconductor Physics, Kyiv, Ukraine*

<sup>3</sup>*Institute of Physics, Baku, Azerbaijan*

*e-mail: arzu\_memmedli\_92@mail.ru.*

The paper presents the results of studying the parameters of silicon photomultipliers of the MAPD-3NK, MAPD-3NM-I and MAPD-3NM-II types with deeply buried pixels. These photodetectors are manufactured in cooperation with the company ZECOTEK. Parameters such as current-voltage characteristics, gain, operating voltage and breakdown voltage were investigated. As a result of the experiments, it was determined that the gain of the MAPD -3NM-II photodiode is 4.5 times higher than that of the MAPD-3NK photodiode, and 2.3 times higher than the gain of the MAPD -3NM-I photodiode. The breakdown voltage of the MAPD -3NM-II photodiode was 52.4V, the breakdown voltage of the MAPD -3NK photodiode was 89 V, the breakdown voltage of the MAPD -3NM-I was 72V. At the same gain value (4.4 \*10<sup>4</sup>), the dark current photodiode MAPD -3NM-II was reduced 15 times compared with photodiode MAPD-3NK and 3 times compared with photodiode MAPD-3NM-I.

**Keywords:** Micropixel Avalanche Photodiode; MAPD; MAPD-3NK; MAPD-3NM-I; MAPD-3NM-II

**PACS:** 85.30.-z; 85.60.Dw

### INTRODUCTION

Silicon-based micropixel avalanche photodiodes (MAPDs) have outperformed photomultiplier tubes (PMTs), PIN diodes, APDs and other analogs in their field of application since 2006 [1-10]. Micropixel avalanche photodiodes have evolved from detecting large numbers of photons to detecting single photons at room temperature. These photodetectors have a wide range of linearity at voltages above the breakdown voltage (or in the Geiger mode) [8-15]. In this regard, the use of silicon photodetectors is of particular importance in studying the parameters of ionizing particles and determining their energy [16-20]. Micropixel avalanche photodiodes are used in high-energy physics, space research and medicine because of their high efficiency, which lies in their structure and operating parameters [2, 8-15]. The performance of MSFD devices is characterized by such parameters as breakdown voltage -  $U_b$ , dark current -  $I_g$ , gain -  $M$ , etc., and their study and improvement is the main task of researchers in this area [20].

One of the main parameters characterizing micropixel avalanche photodiodes is the breakdown voltage. The breakdown voltage in MAPD photodiodes varies depending on internal structural factors: the concentration of additive atoms, the structure (spherical or flat) of the photodiode pixels, and temperature as an external factor. When the same extreme voltage is applied to the MAPD photodiodes, the breakdown voltage and gain change with temperature. At low temperatures, the breakdown voltage decreases and the gain increases. In other words, carriers use a very small part of the energy they receive between two collisions to form optical fanons (the fraction increases with increasing temperature), and the main part to create a new pair of electron holes. Thus, the breakdown voltage decreases and, as a consequence, the gain increases [5]. In addition, the high breakdown voltage

( $U_{op} > 100$  V) of silicon photodetectors requires the assembly of multistage DC-voltage converters, which is not considered financially feasible. Low breakdown voltage in MAPD photodiodes leads to a weaker temperature dependence of photodiode parameters [5].

One of the characteristics of micropixel avalanche photodiodes is dark current. Dark current is one of the quantities that determine the signal-to-noise ratio in these photo recorders. The dark current of photodiodes is formed in photodiodes due to surface and volume currents. In MAPD photodiodes, the bulk current is formed by a temporary path due to defects and intrinsic conductivity [1]. When the applied voltage is greater than the breakdown voltage, a self-regulating process occurs and the bulk current is amplified. Thus, the dark current of the MAPD photodiode is determined as follows:

$$I = I_{surf} + I_{space} = I_{surf} + M \times I_{vol} \quad (1)$$

Here  $I_{surf}$  is the surface current,  $I_{vol}$  is the volume current, and  $M$  is the gain. In MAPD photodiodes, it is possible to reduce the dark current by improving the photodiode fabrication technology and reducing the thickness of the active volume region. The low dark current in MAPD photodiodes determines the minimum energy limit detected in radiation detectors based on these photodiodes.

One of the main parameters characterizing MAPD photodiodes is the gain. The gain characterizes the ionization process that occurs in the avalanche region in MAPD photodiodes [2, 8, 11]. The gain depends on the photodiode capacitance and overvoltage. In MAPD, in the case of a single photoelectron distribution, each pixel has the same gain and is expressed as:

$$M = 2 * C_{pik} (V_{ap} - V_b) / e \quad (2)$$

Here  $C_{pix}$ –pixel capacitance,  $V_{ap}$ –voltage applied to the photodiode,  $V_b$  – breakdown voltage and  $e$ –electron charge.

In MAPD photodiodes (when the gain is small and the dark current is large), it is impossible to apply a uniform distribution of photoelectrons to determine the gain (at room temperature). In this case, the method of measuring the photocurrent due to the change in frequency with respect to the amplitude is used to determine the gain. In this case, to determine the value of the intrinsic photocurrent, the difference between the total current and the dark current is found and determined as follows.

$$I_{ph} = I_{tot} - I_{dc} \quad (3)$$

Here,  $I_{tot}$  – total current,  $I_{dc}$ – dark current,  $I_{ph}$  – photocurrent. The following expression is used to find the average value of the photocurrent at a given frequency:

$$A(M) = \frac{I_{av.ph}}{e \cdot v_M} = \frac{I_{ph} \cdot M}{e \cdot v_M}, \quad M = \frac{A(M)}{A(M \sim 1)} \times \frac{v_M}{v_1} \quad (4)$$

Here,  $e$ –electron charge,  $I_{av.ph}$ –avalanche photocurrent,  $I_{ph}$  –photocurrent,  $M$  amplification coefficient,  $v_1, A(M), v_M, A(M \rightarrow I)$  the average values of the photocurrent and the frequency of the corresponding pulse. The high gain of MAPD photodiodes improves the parameters of radiation detectors based on them, and in most cases there is no need to use additional signal amplifiers.

In the presented work, the values characterizing MAPD photodiodes were studied: gain, operating voltage, detection voltage, and dark current. A comparative study of the parameters of photodiodes MAPD-3NK (2013), MAPD-3NM (2019) and a new development MAPD-3NM (2020) is presented. Correct determination of these parameters is very important for determining the performance of MAPD photodiode devices.

EXPERIMENT

The investigated photodiodes MAPD-3NK, MAPD -3NM-I and MAPD-3NM-II, were produced by Zecotek Photonics at factories in NANOFAB (MAPD-3NK) in South Korea (2013) and MIMOS (MAPD-3NM-I, MAPD-3NM-II) - in Malaysia (2019, 2020).

In the MAPD-3NK and 3NM-I photodiodes, the pixel diameter was  $7\mu m$ , and the pixel density with a  $10\mu m$  step was  $10,000 \text{ pixels/mm}^2$  [8]. In MAPD -3NM-II photodiodes, the pixel diameter was  $12\mu m$ , and the pixel density with a  $15\mu m$  step was  $4450 \text{ pixels/mm}^2$  [3, 5-7, 9-11].

A Keithley 6487 instrument was used to determine the current-voltage characteristics of the photodiodes. A light emitting diode with a wavelength of 450 nm with a low luminous flux was used to determine the gain of avalanche photodiodes. In fig. 2 shows the current-voltage characteristics of the MAPD-3NK, MAPD-3NM-I, and MAPD-3NM-II photodiodes.

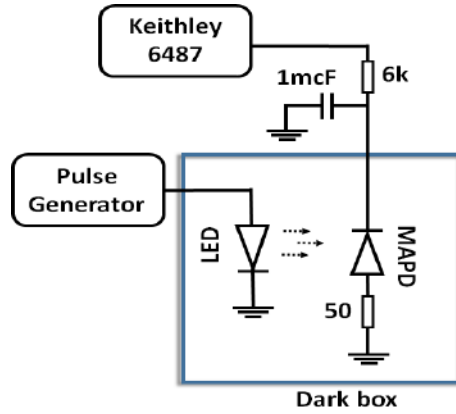


Fig. 1. Schematic of signal readout on MAPD photodiodes.

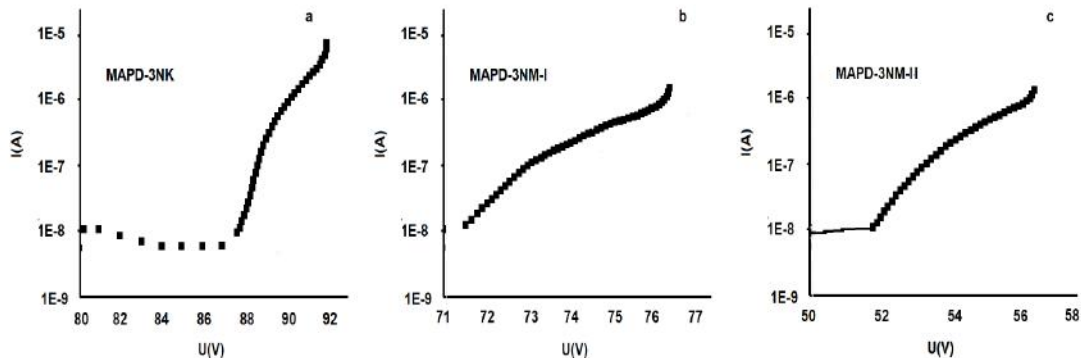


Fig. 2. Current-voltage characteristic of photodiodes MAPD-3NK, MAPD-3NM-I and MAPD-3NM-II (reverse bias).

In fig. 3 shows the dependence of the inverse differential ratio  $dI/(I \times dU)$  of the MAPD-3NK, MAPD-3M-I, and MAPD-3NM-II photodiodes on the applied voltage [6, 13].

It was found that the dark current gradually changes sharply depending on the applied voltage. In the MAPD-3NK photodiode, the voltage  $U_b=89V$  MAPD-3NM-I, and in the MAPD-3NM-II photodiodes  $U_b=72V$  and  $U_b=52.4V$ , the dark current increases sharply, and at subsequent voltage values, the process

is extinguished by a quenching resistor, and the rate of change dark current slows down to saturation. In this case, the gain of the photodiode is optimal. It was revealed that in the MAPD-3NK photodiode  $U_{optimal}=91V$  voltage the dark current is  $1609nA$ , in the MAPD-3NM-I photodiode the optimal voltage is  $U_{optimal}=75.4V$  the dark current is  $655nA$  and in the MAPD-3NM-II photodiode the operating voltage is  $U_{optimal}=55.6V$  and the dark current is  $815nA$ .

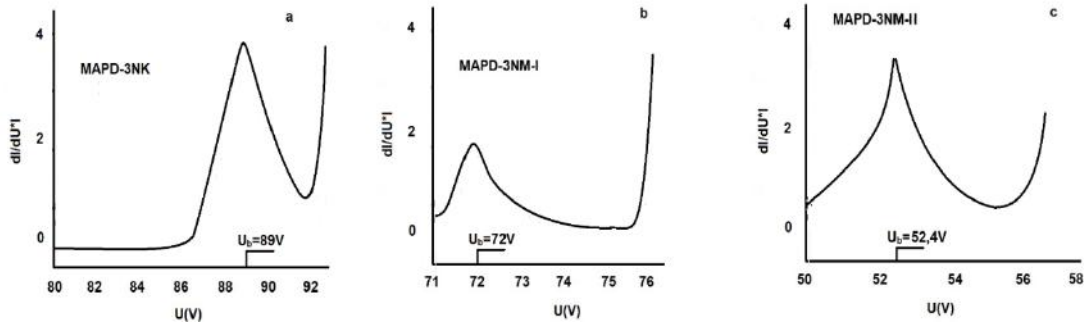


Fig. 3. Dependence of the differential ratio  $dI/(I \times dU)$  of the MAPD-3NK, MAPD-3NM-I and MAPD-3NM-II photodiodes on the applied voltage.

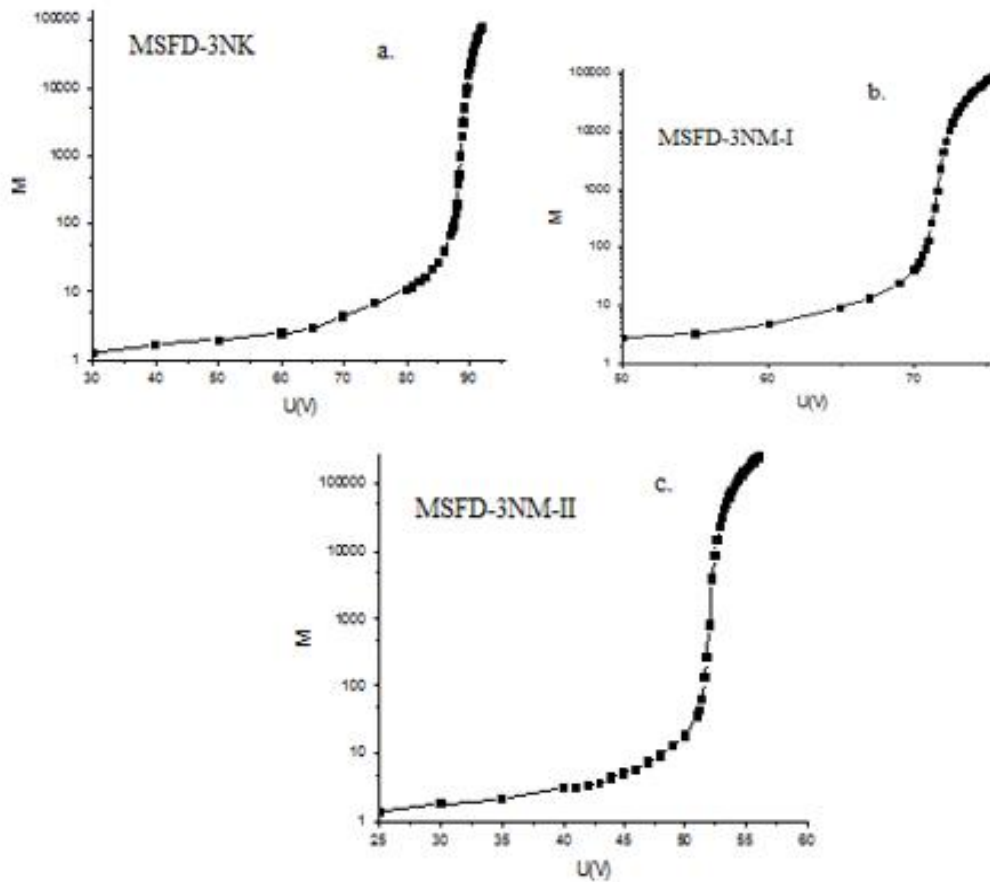


Fig. 4. Dependence of the gain on the voltage of MAPD-3NK, MAPD-3NM-I and MAPD-3NM-II.

In fig. 4 shows the voltage dependence of the gain of the MAPD-3NK, MAPD-3NM-I, and MAPD-3NM-II photodiodes.

Light with a wavelength of  $450nm$  was used from a generator to determine the gain of all three photodiodes. Negative rectangular pulses with an

amplitude of 2.5V and a width of 50ns were applied, varying in frequency from 1kHz to 1MHz. At low values of the gain, the frequency of a rectangular pulse applied to the LED to determine the photocurrent flowing through the photodiode varied in the range from 50kHz to 1MHz, and at high values, the pulse frequency varied between 1kHz-10kHz to ensure normal operation of the photodiodes. In practice, the total and dark current flowing through the avalanche photodiode was measured with a Keithley-6487 picoammeter to determine the gain. The LED pulse from the generator was not applied during the dark current detection.

The voltage applied to all three photodiodes starts at 20V and increases from the breakdown voltage to the maximum value. At 20V, the gain is  $M=1$ , this mode is called the PIN diode mode and is not subject to photocurrent amplification. As the voltage increases, the gain also begins to increase and is determined by the ratio of the average value of the photocurrent when the gain is greater than unity ( $M \gg 1$ ) to the average value of the photocurrent when the gain is equal to unity ( $M \sim 1$ ), the result is multiplied by the frequency ratio:  $M = \frac{A(M)}{A(M \sim 1)} \times \frac{\nu_M}{\nu_1}$ . Thus, the gain at an optimal

voltage of 91V for the MAPD-3NK photodiode was set at  $\sim 4.4 \cdot 10^4$  (25°C). In the MAPD-3NM-I photodiode, the gain at 75.4V was  $8.6 \cdot 10^4$ , and in the MAPD-3NM-II photodiode, the 55.6V gain was  $2 \cdot 10^5$  (25°C).

In fig. 5 shows the dependence of the gain on the optimal voltage on the MAPD-3NK, MAPD-3NM-I and MAPD-3NM-II photodiodes.

In the optimal case, the gain of the MAPD-3NM-II photodiode was 4.5 times higher than that of the MAPD-3NK photodiode, and 2.3 times higher than the gain of the MAPD-3NM-I photodiode.

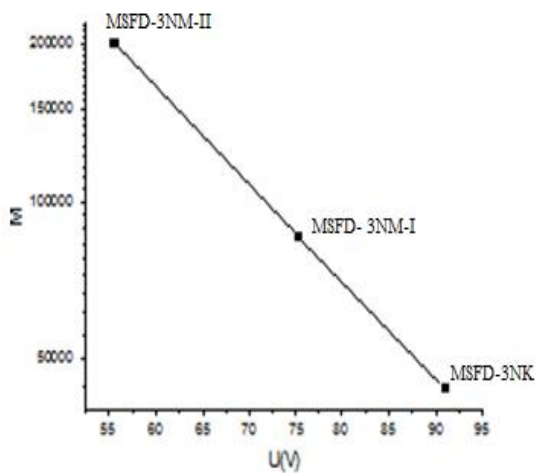


Fig. 5. Dependence of the gain on the optimal voltage on the MAPD-3NK, MAPD-3NM-I and MAPD-3NM-II photodiodes.

In fig. 6 shows the dependence of the dark current on the voltage at the same value of the gain for the MAPD-3NK, MAPD-3NM-I and MAPD-3NM-II photodiodes.

Thus, with the same value of the gain ( $M=4.4 \cdot 10^4$ ), the dark current of the MAPD-3NM-II

photodiode is reduced 15 times compared to the MAPD-3NK photodiode and 3 times compared to the MAPD-3NM-I photodiode.

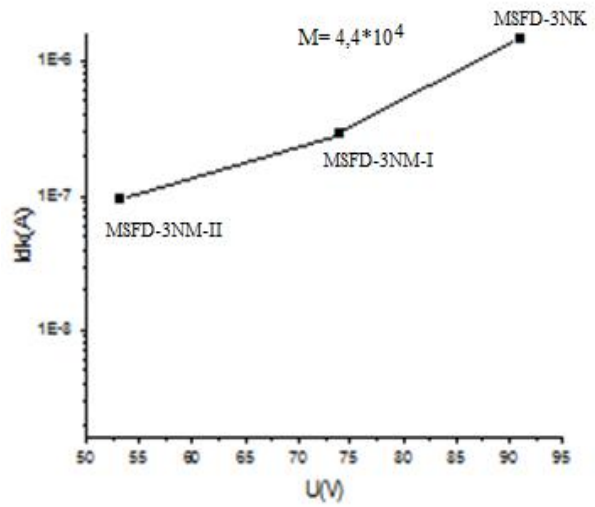


Fig. 6. Dependence of the dark current on the voltage at a constant value of the gain in the MAPD-3NK, MAPD-3NM-I and MAPD-3NM-II photodiodes.

## RESULTS

As a result of the experiments, the parameters characterizing the MAPD photodiodes were determined. The breakdown voltage of the MAPD-3NK photodiode at 25°C was 201, the optimal voltage  $U_{optimal}=91V$ , the gain  $M=4.4 \cdot 10^4$ , the gain of the MAPD-3NM-I photodiode  $=8.6 \cdot 10^4$ , the optimal voltage  $U_{optimal}=75.4V$ , breakdown voltage  $U_b=72V$ . In the MAPD-3NM-II photodiode  $U_b=52.4V$ ,  $U_{optimal}=55.6V$ , and the gain  $M=2 \cdot 10^5$ . The dark current of the MAPD-3NM-II photodiode  $I_{dk}=815nA$ , the dark current of the MAPD-3NK photodiode  $I_{dk}=1609nA$ , photodiode MAPD-3NM-I  $I_{dk}=655nA$ .

It was determined that, in the optimal case, the gain of the MSFD-3NM-II photodiode was 4.5 times higher than that of the MSFD-3NK photodiode, and 2.3 times higher than the gain of the MSFD-3NM-I photodiode. With the same value of the amplification factor ( $M=4.4 \cdot 10^4$ ), the dark current of the MSFD-3NM-II photodiode is reduced 15 times compared to the MSFD-3NK photodiode and 3 times compared to the MSFD-3NM-I photodiode.

The results showed that the newly developed MAPD-3NM-II photodiode outperforms the MAPD-3NK and MAPD-3NM-I photodiodes in most parameters, and the development of spectrometers based on the new MAPD-3NM-II photodiodes to be more appropriate and optimal.

## ACKNOWLEDGMENT

This work was supported by the Scientific Foundation of SOCAR.

- [1] *G.F. Knoll*. Radiation detection and measurements., John Wiley and Sons, Inc., New York 2000.
- [2] *D. Renker*. Photosensors., Nuclear Instruments and Methods in Physics Research., 2004, v.527, pp.15–20.
- [3] *Z. Sadygov, A. Olshevski, I. Chirikov, I. Zheleznykh, A. Novikov*. Three advanced designs of micro-pixel avalanche photodiodes: Their present status, maximum possibilities and limitations., Nucl. Instrum. Methods Phys. Res. 2006, A 567 pp.70–73.
- [4] *Z. Ya. Sadygov*. “Microchannel avalanche photodiode,” RF Patent No. 2316848, 2008.
- [5] *S. Nuruyev, G. Ahmadov, A. Sadigov, R. Akberov, F. Ahmadov, M. Holikand, Yu. Kopatch*. Performance of silicon photomultipliers at low temperature, J. Instrum. 2020, 15, C03003.
- [6] *N. Sadigova, K. Isayev, A. Sadigov, F. Ahmadov, E. Yilmaz, A. Mammadli & A. Gerayeva*. Improvement of buried pixel avalanche photodetectors. Colloquim Journal, physics and mathematics, 8.
- [7] *Z. Sadygov, A. Sadigov and S. Khorev*. Silicon Photomultipliers: Status and Prospects, Physics of Particles and Nuclei Letters., 2020, v.17, No. 2, pp.160–176.
- [8] *F. Ahmadov, G. Ahmadov, E. Guliyev, R. Madatov et al.*, New gamma detector modules based on micropixel avalanche photodiode., 2017, JINST, 12, C01003.
- [9] *F. Ahmadov, G. Ahmadov, E. Guliyev et al.*, Development of compact radiation detectors based on MAPD photodiodes with Lutetium Fine Silicate and stilbene scintillators., 2015, JINST, 10, C02041.
- [10] *M. Holik, F. Ahmadov, G. Ahmadov, R. Akbarov, D. Berikov, Y. Mora, S. Nuruyev, P. Pridal, A. Sadigov, Z. Sadygov, J. Zich*. Miniaturized read-out interface “Spectrig MAPD” dedicated for silicon Photomultipliers, Nucl. Instrum. Methods Phys., Res. 2020, A 978 pp.164–444.
- [11] *Z. Sadygov, A. Ariffin, F. Akhmedov, N. Anfimov, T. Bokova, A. Dovlatov, I. Zheleznykh, F. Zerrouk, R. Mekhtieva, A. Ol’shevskii, A. Sadygov, A. Titov, V. Chalyshev, M. Troitskaya*. Technology of manufacturing micropixel avalanche photodiodes and a compact matrix on their basis, Physics of Particles and Nuclei Letters., 2013, v.10, pp.780-782.
- [12] *Z. Sadygov et al.*, Development of scintillation detectors based on micro-pixels avalanche photodiodes, PoS (PhotoDet 2012)037.
- [13] *G. Ahmadov, F. Ahmadov, M. Holik et al.*. Gamma-ray spectroscopy with MAPD array in the readout of LaBr3:Ce scintillator., 2021 JINST 16 P07020.
- [14] *A. Sadigov, F. Ahmadov, G. Ahmadov, A. Ariffin, S. Khorev, Z. Sadygov, S. Suleymanov, F. Zerrouk, R. Madatov*. A new detector concept for silicon photomultipliers., Nucl. Instrum. Meth., 2016, A 824, pp.135-136.
- [15] *R.A. Akbarov, S.M. Nuruyev, G.S. Ahmadov et al.*. Scintillation readout with MAPD array for gamma spectrometer., 2020 JINST 15 C01001.
- [16] *Z. Sadygov, Kh. Abdullaev, N. Anfimov et al.*. A microchannel avalanche photodiode with a fast recovery time of parameters., 2013, Technical Physics Letters 39.
- [17] *F. Ahmadov, F. Abdullayev, G. Ahmadov, A. Sadigov, Z. Sadygov, R. Madatov, S. Suleymanov, R. Akberov, N. Heydarov, M. Nazarov*. New phoswich detector based on LFS and p-terphenyl scintillators coupled to micropixel avalanche photodiode, Funct. Mater. 2017, 24, pp.341–344.
- [18] *G.S. Ahmadov, Yu.N. Kopatch, S.A. Telezhnikov, F.I. Ahmadov, C. Granja, A.A. Garibov, S. Pospisil*. Detection of ternary and quaternary fission fragments from 252 Cf with a position-sensitive  $\Delta E-E$  telescope based on silicon detectors, Physics of Particles and Nuclei Letters, Physics of Particles and Nuclei Letters., 2015, 12, pp.542-549.
- [19] *E. Jafarova, Z. Sadygov, F. Ahmadov, A. Sadygov, A. Dovlatov, L. Alieva, E. Tapdygov, N. Safarov*. On features of barrier capacitance of micropixel avalanche photodiodes on different frequencies, Materials Science and Condensed Matter Physics Editia., 2014, 7, pp.266-266.
- [20] *F. Ahmadov, F. Abdullayev, R. Akberov, G. Ahmadov, S. Khorev, S. Nuriyev, Z. Sadygov, A. Sadigov, S. Suleymanov*. On iterative model of performance of micropixel avalanche photodiodes, Nucl. Instrum. Meth. 2018, A 912, pp.287-289.

Received: 12.09.2022

## SOME THEORETICAL ISSUES OF FORMATION AND DEVELOPMENT OF GAS VOIDS IN CROSS-LINKED POLYETHYLENE INSULATION

A.M. HASHIMOV, A.O. ORUJOV, M.A. JAMALOV

<sup>1</sup>*Azerbaijan National Academy of Science*

*H. Javid ave., Baku, Azerbaijan, AZ1143, e-mail: [arif@physics.ab.az](mailto:arif@physics.ab.az)*

<sup>2</sup>*Azerbaijan Technical University*

*H. Javid av., 25 Baku, Azerbaijan AZ 1073, e-mail: [mehticamal@aztu.edu.az](mailto:mehticamal@aztu.edu.az)*

It is of great practical importance to study the mechanism of formation of gas bubbles during thermal treatment in the production of medium and high voltage XLPE insulated cables. Experiments show that polymer insulation of cables is very sensitive to these types of defects. Taking this into account, the article developed a mathematical model of the development of gas bubbles in the polymer based on the theory of high elasticity and large mechanical deformation. Based on the mathematical model, the conditions for the development of gas voids were determined, and it was possible to find the critical degree of swelling. It was noted that the values obtained as a result of the theoretical calculations are very important in choosing the optimal technological mode in terms of obtaining homogeneous insulation.

**Keywords:** polymers, XLPE, voids, elasticity module, thermal treatment, mathematical model.

**PACS:** 61.80.Az, 82.35.Lr

### INTRODUCTION

Stable, continuous and reliable operation mode of power supply of power units of power stations, industrial enterprises, transportation, utilities and other areas of the agricultures are directly characterized by the reliability of power cables. The reliability and lifespan of cables are determined by the quality of their insulation. Different types of damage occur in cable insulation during both production and operation. During operation, certain electrophysical processes occur in these damages, which causes aging of insulation. As a result, the performance and reliability of the insulation decrease. For this reason, the prevention or minimization of various types of damage in cable insulation is one of the urgent issues for cable manufacturers and operators.

The main types of the aging phenomenon in cable insulation can be noted as following [1,2,3]:

- electrical aging;
- oxidation and heating aging in the insulation;
- aging due to the influence of moisture in the insulation;
- aging due to damages caused by other effects in the insulation.

The most common is electrical aging. This aging is caused by electrical discharges (partial discharge) occurring in the micro-gaps (gas gaps) in the insulation. Due to the effect of discharges, collapsing of molecular bonds in the insulation occur. The breakdown degree and its nature are characterized by the type of insulation material and the nature of the damage.

Currently, in cable technology, especially in the production of 6-500 kV voltage cables, cross-linked polyethylene (XLPE) is used as insulation. These cables have many advantages over oil-impregnated paper-insulated cables [4,5,6,7]. The most important is that depending on the laying conditions, the load carrying capacity must be 15-30% higher due to the higher operating temperature. At the same time, the

technology of manufacturing XLPE insulated cables is simple and economically efficient. The operation of these types of cables in about fifty years confirmed their effectiveness. XLPE insulated cables are more reliable and long-lasting in addition to high operational characteristics.

Two modern cable plants in Azerbaijan fully satisfy the country's energy system's demand for this type of cables. TPE insulated power cables produced by both plants are competitive with similar cables from leading western manufacturers.

In addition to all this, unlike impregnated paper insulation, monolithic polymer insulation of cables is more sensitive to various external inclusions (additives), voids and other defects (Figure 1). These defects create a large local electric field intensity in the insulation, lower the breakdown voltage, cause the formation of electric and water trees during operation, as a result of which the insulation aging occurs [8,9]. Just like the variety of foreign inclusions (injuries), the causes of their occurrence are also different. The most common non-homogeneous areas in XLPE insulation are gas voids and moisture. This type of regions can appear in the insulation both before heat treatment and during heat treatment.

Thus, one of the important criteria for evaluating XLPE insulated cables is the electrical strength of the insulation, that is, the electrical strength determines the reliability of the cable as a whole.

The electrical strength of the insulation under alternating and impulse voltages is determined by a number of factors - macro and microdefects of various nature in the insulation system, microvoids, products of thermal destruction, alien particles etc.

There is a high probability of gas voids in the insulation in the production of XLPE-insulated cables. The technological mode should be chosen so that the dimensions of these gaps do not exceed the critical limit that lowers the electrical strength of the insulation.

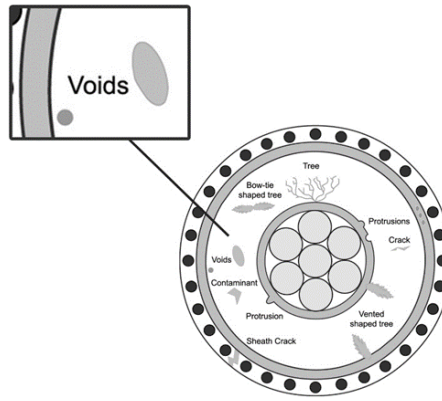


Fig. 1. Different types of defects in XLPE insulation.

The above-mentioned suggests that the reasons for the appearance of gas gaps and other inhomogeneous areas in the insulation in the production of polymer, including woven polyethylene insulated cables, and modern methods for their determination have been studied in detail.

At the same time, the development conditions and kinetics of gas voids formed due to dissolved gases during thermal treatment of insulation have not been sufficiently studied. The study of the growth conditions of gas bubbles and the influence mechanism of some technological parameters that play an important role in their development is very relevant from a practical and theoretical point of view. This article is devoted to the analysis of the development mechanism of gas bubbles that appear during thermal processing of XLPE insulation.

The achieved results can be useful in calculating the optimal technological mode for obtaining monolithic cable insulation.

## DEVELOPMENT CONDITIONS OF GAS VOIDS

The reasons for the formation of dissolved components during the technological regime in polymer insulation can be divided into three groups:

- the first group includes substances dissolved in the material before thermal treatment - moisture, air, solvents, etc. belongs to.
- the second group includes substances released in the material during heat treatment - by-products of the construction reaction, decomposition products of organic peroxides, products resulting from the destruction of the polymer.
- the third group includes gases dissolved in the polymer when technological heat treatment is carried out at high pressure.

When peroxide is used in the cross-linking process of polyethylene, the release of methane and acetophenone gases is characteristic. Technological thermal processing is carried out in a nitrogen (N<sub>2</sub>) environment at high pressure, in this case, additional nitrogen gas is dissolved in processed polyethylene.

At high temperatures, these gaseous products cause gas bubbles to form in polyethylene. In these

bubbles, under certain conditions, ionizations - partial discharges occur and finally the insulation breakdowns. It should be taken into account that since the structure is heterogeneous, there are ionization centers with radius  $r$  in the polymer. Therefore, let's look at the mechanism of the growth of the air gap of radius  $r$ , which is already present in the polymer.

The equilibrium pressure of vapors (gases) dissolved in the material is a function of temperature and concentration, i.e.  $P = f(V, T)$ . The dependence of equilibrium pressure on concentration is expressed by Henry's law [13].

$$P = \frac{U}{h} \quad (1)$$

where,  $U$  - the concentration of gases dissolved in the material,  $\text{kg/m}^3$ ;  $h$  - is the solubility coefficient,  $\text{kg/Pa}\cdot\text{m}^3$ .

It is known that the gases cannot be infinitely dissolved in the polymer, that is, at a certain value of the concentration (at a given pressure and temperature), the polymer-gas equilibrium is established (saturated solution).

The growth of a gas bubble in a polymer melt can occur if the equilibrium pressure is greater than the pressure of the region surrounding the air gap (ambient pressure). Therefore, the growth condition of gas bubbles will be as follows:

$$P = \sum P_i \geq P_0, \quad (2)$$

where,  $\sum P_i$  is the total equilibrium pressure of gases dissolved in the substance;  $P_0$  is the pressure in the polymer in the region where the gas bubble develops.

In the production of XLPE insulated cables in modern technological equipment, the peroxide cross-linking process is carried out at high temperatures (300 - 3600 C), and at this time polyethylene becomes highly elastic. In the case of high elasticity, the properties of polymers obey large elastic mechanical deformation laws [14,15]. In the simplest case, the following statement is true for a tensile specimen:

$$\sigma = \frac{G}{2} (\lambda - \lambda^{-2}), \quad (3)$$

where,  $\lambda = l/l_0$ ;  $l_0$  – the length of the sample until tension;  $l$  – the length of the sample after stretching (steady state);  $G$ - the modulus characterizing the elasticity property, Pa;  $\sigma$  – mechanical stress in tension, Pa (considering the cross-sectional area in the non-tensile state).

In the theory of large elastic mechanical deformation [15], the expression of the dependence of the dimensions of the spherical cavity (in this case, the gas cavity) located in a large block of material on the pressure inside it was obtained:

$$P = \frac{G}{2} (5 - 4\lambda^{-1} - \lambda^{-4}), \quad (4)$$

where,  $P$ - pressure;  $G$ - elasticity of the polymer (modulus of displacement);  $\lambda$  - is the degree of swelling of the sphere,  $\lambda=r/r_0$ ,  $r_0$  is the initial radius of the sphere,  $r$  is the radius in the deformed state. Equation (4) was experimentally confirmed in [15].

Modulus  $G$  is one of the quantities that play a key role in the development of the sphere.

The value of  $G$  depends on the degree of cross-linking of molecules and is determined by the following formula [16].

$$G = 2\rho \frac{RT}{M_{av}}, \quad (5)$$

where,  $\rho$ - density of PE, kg/m<sup>3</sup>;  $T$ -temperature, K;  $R$ - gas constant, C/mole·K;  $M_{av}$  is the average molecular weight of the polymer chain located between two adjacent building points. The value of  $M_{av}$  is inversely proportional to the number of transverse bonds in the XLPE.

If the initial radius of the gas cavity ( $r_0$ ) is very small, then it is necessary to add the pressure accumulator that takes into account the effect of surface tension to the right side of equation (4):

$$\Delta P = \frac{G}{2} \left[ 5 - 4 \left( 1 - \frac{\alpha_g}{r_0 G} \right) \lambda^{-1} - \lambda^{-4} \right] \quad (6)$$

where  $\alpha_g$  - is the surface tension of the polymer.

For a thin-walled spherical bubble, equation (6) becomes:

$$\Delta P = 2G \left( \frac{t_0}{r_0} \right) (\lambda^{-1} - \lambda^{-4}), \quad (7)$$

where  $t_0$  - is the thickness of the sphere wall.

Taking into account pressures inside the sphere (4) and surface tension (6), we can write the development condition of the gas void inside the highly elastic polymer:

$$P - P_0 = \frac{G}{2} (5 - 4\lambda^{-1} - \lambda^{-4}) + \frac{G}{2} \left[ 5 - 4 \left( 1 - \frac{\alpha_g}{r_0 G} \right) \lambda^{-1} - \lambda^{-4} \right] \quad (8)$$

After some transformations, we get:

$$\frac{P - P_0}{G} = \frac{5}{2} - 2 \left( 1 - \frac{\alpha_g}{2r_0 G} \right) \lambda^{-1} - \frac{\lambda^{-4}}{2} \quad (9)$$

or

$$P - P_0 = \frac{2\alpha_g}{r_0 \lambda} + G(5 - 4\lambda^{-1} - \lambda^{-4}) \quad (10)$$

When  $\lambda=1$ , the pressure in the gas space depends only on the surface tension. If

$P - P_0 < 2\alpha_g/r_0$ , then the gas gap will not grow.

If  $1 - \frac{\alpha_g}{2r_0 G} > 0$ , then the gas bubble with radius  $r_0$  will grow to the limit calculated by formula (6). Here  $\Delta P = P - P_0$ ,  $P_0$  is the pressure of the medium surrounding the polymer, and  $P$  is the pressure inside the gas bubble.

If  $\frac{2(P - P_0)}{G} < 5$ , then the size of the initial gas bubble grows to the limit determined by the formula(9).

If the condition  $\frac{2(P - P_0)}{G} \geq 5$  is met, the gas bubble should grow to infinity. In reality, gas bubble growth is limited by the allowable value of the relative tensile elongation of the cross-linked polyethylene, or the polymer collapses when the mechanical strength of the polymer is low (case of poor cross-linking).

If  $1 - \frac{\alpha_g}{2r_0 G} < 0$ , the growth of the gas bubble occurs only if the condition  $\frac{2(P - P_0)}{G} > 5$  is met, and with

a certain probability (as in hot liquids). In this case, the probability of bubble growth can be determined by a method analogous to the theory of bubble formation in heated liquids [16].

It is clear from the analysis that the growth rate of the bubble depends on the modulus of elasticity  $G$  of the polymer, the surface tension force  $\alpha_g$  and the starting radius  $r_0$ . The average surface tension of hydrocarbons and other organic substances is about  $3 \cdot 10^{-2}$  N/m. The value of the modulus of elasticity depends on the amount of PDK to which PE is added. It has been determined experimentally that when  $\approx 1.8$ -2% PDK is added to PE, the value of  $G$  is around  $\approx 10^5 - 10^6$  N/m<sup>2</sup> [12]. Thus, at the average value of the  $\alpha_g/G$  ratio,  $r_0 = 1.5 \cdot 10^{-7}$  m is obtained. Accordingly, as long as the pressure inside the sphere is greater than the pressure of the polymer surrounding it, all gas bubbles larger than  $10^{-7}$  m in size will grow in any case. In order to satisfy the condition  $\alpha_g/2Gr_0 < 1$ ,  $r_0$  must be  $< 1.5 \cdot 10^{-7}$  m. This condition is not met in technical materials.

Measurements carried out in cable factories on ready-made XLPE insulated cable samples showed that it is possible to have bubbles with a diameter of  $(10^{-4} - 10^{-5})$  m in the insulation. Therefore, the condition  $\alpha_g/2G \cdot r_0 \ll 1$  is always satisfied. In this case, we write the following approximate expression from equation (9).

$$\frac{P-P_0}{G} = \frac{5}{2} - 2\lambda^{-1} - \frac{\lambda^{-4}}{2} \quad (11)$$

As you can see, surface tension can be neglected in this case. In this case, the condition  $P - P_0 > 5G$  is unacceptable, because the growth of bubbles becomes more intense.

The process is carried out at high pressure so that bubbles do not grow during the construction process, in  $\lambda=1$ . For the case with  $\lambda=1$ , we get from (11).  $P - P_0 \leq 0$  or  $P \leq P_0$

Apparently, in order for the bubble not to grow, the external pressure must be greater than the total pressure of the gases dissolved in the polymer.

The growth of the initial gas bubble with radius  $r_0$  is conditioned by the following probability [17].

$$W = \exp\left(-\frac{Q}{kT}\right) \quad (12)$$

where, k-Boltzmann constant; Q- is needed energy for bubble growth; T is the temperature.

Taking into account that the degree of swelling of the bubble  $\lambda$  depends on the equilibrium pressure inside it, P, on the pressure in the growth region (external pressure)  $P_0$ , on the modulus of elasticity of the material G and on the surface tension  $\alpha_g$ , the critical value of the degree of swelling can be written for  $\lambda_{cr}$ :

$$\lambda_{cr} = \frac{2(1-\frac{\alpha_g}{2Gr_0})}{(\frac{5}{2}-\frac{P-P_0}{G})}, \quad (13)$$

At the beginning of the cross-linking process, at high temperature (300-360<sup>0</sup>) C, the polymer becomes molten, and the value of G becomes very small. In this case, the critical value of the degree of swelling of the sphere can be calculated analogously to the formation and development of bubbles in heated liquids [17], i.e.

$$\lambda_{cr} = \frac{2\alpha_g}{r_0(P-P_0)}, \quad (14)$$

accordingly, the critical radius  $r_{cr} = \lambda_{cr} \cdot r_0$

$$r_{cr} = \frac{2\alpha_g}{(P-P_0)}, \quad (15)$$

For gas bubble growth, the residual value of equilibrium pressure (P-P<sub>0</sub>) should be close to the value of  $2\alpha_g/r_0$ .

If we take  $\alpha_g = 3 \cdot 10^{-2}$  N/m for polymers in the highly elastic case, the equilibrium pressure should be  $P-P_0 = 10^5$  Pa for the growth of the initial bubble with radius  $r_0$ .

As can be seen from (15), the critical radius of the bubble depends on the properties of the material and external conditions.

After the thermal treatment process (cross-linking process), the cooling process should be carried out at high pressure to prevent the growth of gas voids. As the temperature decreases, the vacuum pressure P decreases.

During cooling, the value of the modulus of elasticity increases sharply (several orders) in the region of transition from the highly elastic state to the amorphous-crystalline state (105-115<sup>0</sup> C) of the cross-linked polyethylene. Accordingly, at temperatures below 100<sup>0</sup> C, the growth of microgas bubbles in the polymer is impossible due to the large value of the modulus of elasticity of polyethylene. Therefore, the cooling mode should be selected so that the temperature of the polymer should be below 100<sup>0</sup> C, even in places close to the conductor. However, during operation, the temperature in certain areas of the insulation may exceed 100<sup>0</sup> C for various reasons (for example, in short circuits). In this case, the growth of gas bubbles is possible. Therefore, in cases where the thickness of the insulation is large, especially in XLPE-insulated cables with a rated voltage of 110 kV and higher, gas products dissolved in the insulation should be removed from the insulation. For this purpose, the cable should be kept for certain time in an environment with a temperature of (80-90<sup>0</sup>) C. At this time, dissolved gases are removed from the insulation by way of diffusion.

The obtained results are very important in terms of calculating the optimal technological heating mode.

## RESULT

The mechanism of formation of gas bubbles in the insulation during thermal treatment in the production of XLPE insulated cables has been determined.

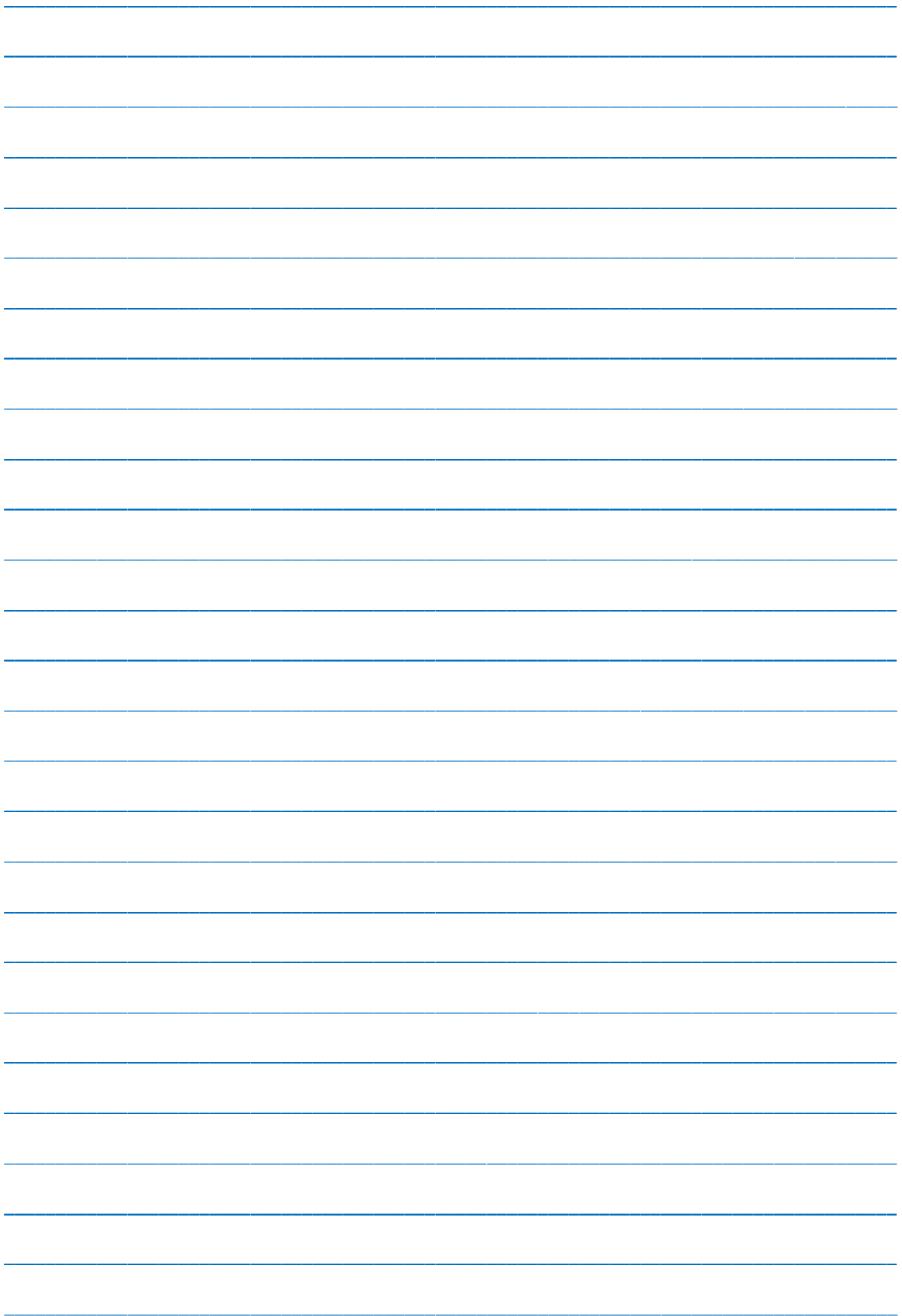
Based on the theory of high elasticity and large mechanical deformation, a mathematical model of the development of gas voids in polyethylene in the state of high elasticity was developed.

Considering various factors, the growth conditions of gas voids were determined.

A mathematical expression was obtained to determine the critical degree of swelling of gas cavities. According to this expression, it is possible to determine the development condition of gas spaces. The obtained results can be useful in choosing the optimal technological mode in terms of obtaining monolithic insulation in the production of XLPE insulated cables.

- [2] G.C. Montanari, G. Mazzanti. 2002. Ageing of polymeric insulating materials and insulation system design. *Polymer International*, 51(11), 1151–1158. doi:10.1002/pi.955
- [3] S.N. Koikov. Electrical aging of solid dielectrics. S.N. Koikov, A.N. Tsikin. M. - L.: Energy, 1968. -186 p.
- [4] IEC 62067. Power Cables with Extruded Insulation and Their Accessories for Rated Voltages from 150 kV Up to 500 kV
- [5] A. Kozhevnikov. Modern cable insulation. Magazine "News of Electrical Engineering" No. 2 (38) 2006
- [6] A.S. Mitkevich, N.G. Paverman, A.N. Elagina. Cable compositions based on polyethylene and polyvinyl chloride. Development trends in Russia. Magazine "Cables and Wires" No. 1 (302) 2007
- [7] A.O. Orujov, R.H. Rzayev, S.N. Niftiyev. Cross-linked polyethylene insulated power cables with high performance characteristics. Baku, ELM, 2013, 341 p.
- [8] Y. Luo, J. Luo, B. Li. Performance of Cross-linked Polyethylene Insulated Cable based on Detection of High Voltage Electric Field. *Int. Jnl. of Multiphysics* Volume 13 · Number 2 · 2019
- [9] Tatyana V. Susakova, Arina M. Evseeva and Irina A. Chesnokova. Analysis and prevention of accident-caused faults in power cable lines .MATEC Web of Conferences 110, 01077 (2017)
- [10] N.M. Koryakin, P.V. Fursov. "Calculation of the possibility of formation of air inclusions in the plastic insulation of cables during cooling", "Cable Technology", 1977, issue 5, p. 8-11.
- [11] A.O. Orujov. "Research of physical processes during technological heat treatment of cables and wires with plastic insulation", Abstract of Ph.D., M., MPEI, 1976, 20 s
- [12] A.O. Orujov, Yu.V. Zherdev, S.D. Kholodny. "Study of pore formation during the vulcanization of polyethylene with dicumyl peroxide", "Cable Technology", vol. 1(119), 1975, pp. 27-30.
- [13] E.F. Peschke et. al. A new generation of joints for XLPE-insulated extra-high voltage cables: CIGRE 21-204. 1996.
- [14] A.Yu. Grosberg, A.R. Khokhlov. Statistical physics of macromolecules. Study guide. — M.: Science. 1989. - 344 p.
- [15] A. Green, J. Adkins. Large elastic deformations and nonlinear continuum mechanics. Moscow: Mir, 1965, 455 p.
- [16] E.F. Peschke et. al. A new generation of joints for XLPE-insulated extra-high voltage cables: CIGRE 21-204. 1996.
- [17] L.D. Landau, E.M. Lifshits. Statistical physics, M., "Science", 1964, 310 p..

*Received:13.09.2022*



---

---

**CONTENTS**

---

---

1.	The peculiarities of electrical conductivity in $\text{AgSbSe}_2$ and $(\text{AgSbSe}_2)_{0,85}(\text{PbTe})_{0,15}$ <b>A.A. Saddinova, R.I. Selim-zadeh, A.E. Babayeva</b>	3
2.	Infrared spectra, differential scanning calorimetry and mechanical properties of polyethylene doped with $\text{CaGa}_2\text{S}_4:\text{Eu}^{+2}$ <b>T.D. Ibragimov, O.B. Tagiev, I.S. Ramazanova, T.Sh. Ibrahimova, A.F. Nuraliyev, E.G. Asadov, B.H. Ibragimov</b>	6
3.	Simulation spatial structure of amyloid beta-peptide (28-35) determined by molecular mechanics method <b>G.Z. Najafova</b>	11
4.	Demonstrating the importance of emissivity measurement in determining the doses of light sources on tissue mimicking materials such as Laser, IPL and LED <b>Hüseyin Okan Durmuş, Mirhasan Yu Seyidov</b>	16
5.	On the theory of dispersion interferometer with two nonlinear crystals <b>Sh.Sh. Amirov</b>	27
6.	Plasma etching of GaAs surface in a planar gas discharge system <b>B.G. Salamov, T.G. Mammadov</b>	30
7.	Measurement of internal and surface temperatures and optical properties of zerdine phantom under 635 nm low level laser irradiation <b>Hüseyin Okan Durmuş, Mirhasan Yu. Seyidov</b>	39
8.	Investigation of parameters of silicon photomultipliers <b>A. Mammadli, B. Ibrahimov, Y. Bacherikov, Z. Ahmadov</b>	48
9.	Some theoretical issues of formation and development of gas voids in cross-linked polyethylene insulation <b>A.M. Hashimov, A.O. Orujov, M.A. Jamalov</b>	53



[www.physics.gov.az](http://www.physics.gov.az)